DOT/FAA/TC-19/50, P3

Federal Aviation Administration
William J. Hughes Technical Center
Aviation Research Division
Atlantic City International Airport
New Jersey 08405

Development of a Tabulated Material Model for Composite Material Failure, MAT213

Part 3: Implementation of Probabilistic Modeling Capability in the Tabulated Composite Failure Model MAT213

January 2020

Final Report

U.S. Department of Transportation
Federal Aviation Administration

NOTICE

Technical Report Documentation Page

1. Report No.	2. Government Accession No.	3. Recipient's Catalog No.
DOT/FAA/TC-19/50, P3		

4. Title and Subtitle	5. Report Date
Development of a Tabulated Material Model for Composite Material Failure, MAT213 Part 3: Implementation of Probabilistic Modeling Capability in the Tabulated Composite Failure Model MAT213	January 2020 6. Performing Organization Code
7. Author(s) Tobias Achstetter, Chung-kyu Park, and Cing-Dao Kan	8. Performing Organization Report No.
9. Performing Organization Name and Address Center for Collision Safety and Analysis George Mason University 4400 University Drive, MSN 4C6 Fairfax, VA 22030	10. Work Unit No. (TRAIS) 11. Contract or Grant No. FAA Grant 12-G-001 NASA Contract NN15CA32
12. Sponsoring Agency Name and Address U.S. Department of Transportation Federal Aviation Administration FAA New England Regional Office 1200 District Ave Burlington, MA 01803	13. Type of Report and Period Covered Final Report 14. Sponsoring Agency Code AIR-6A0

15. Supplementary Notes

The Federal Aviation Administration Aviation William J. Hughes Technical Center Research Division COR was Daniel Cordasco, and the NASA Glenn Research Center Contracting Officer Representative was Robert Goldberg.

16. Abstract

One of the challenges in building a predictive numerical model for composites is the ability to model accurately the behavior of the structure, especially under impact loading. This report provides details of a newly developed orthotropic material model that has three distinct sub-models for describing deformation, damage, and failure of general composites, and has been implemented in the commercial finite element program, LS-DYNA, as *MAT_213 (*MAT_COMPOSITE_TABULATED_PLASTICITY _DAMAGE). The model is driven by tabulated data that can be generated using laboratory tests or via virtual testing. The yield function is a modified form of the Tsai-Wu failure model. A non-associated plastic flow is used. Rate and temperature dependence are supported along with tension-compression asymmetric behavior. The damage sub-model allows for both uncoupled and coupled parameters to be defined. Strain equivalence between the true and the effective stress space permits decoupling of the plasticity and damage calculations. The failure modeling is currently being enhanced and the initial version discussed in this report includes some of the most commonly used failure criteria – principal strain, Tsai-Wu, and a generalized tabulated laminate failure criterion. Part 1 describes the experimental procedures and results from characterizing a widely used aerospace composite – T800-F3900. Part 2 discusses the theory, implementation, verification and validation of the MAT213 material model using the T800-F3900 composite as a test case. Verification tests are carried out using single and multiple element models. Validation tests are carried out using data from impact tests carried out at NASA-GRC involving T800-F3900 composite panels. Part 3 discusses the probabilistic modeling implementation in LS-DYNA to support MAT213 (via *DEFINE_STOCHASTIC_VARIATION_MAT213) and compares the results from deterministic and probabilistic modeling of impact events.

17. Key Words	18. Distribution Statement
Orthotropic plasticity, material characterization testing, damage, failure, cohesive zone modeling, explicit finite element analysis, probabilistic modeling, impact simulations. Composite failure, LSDYNA, MAT213, Tabulated material model	This document is available to the U.S. public through the National Technical Information Service (NTIS), Springfield, Virginia 22161. This document is also available from the Federal Aviation Administration William J. Hughes Technical Center at actlibrary.tc.faa.gov.

19. Security Classif. (of this report)	20. Security Classif. (of this page)	21. No. of Pages	22. Price
Unclassified	Unclassified		

TABLE OF CONTENTS

LIST OF FIGURES

LIST OF TABLES

EXECUTIVE SUMMARY

One of the challenges in building a predictive numerical model for composites is the ability to model accurately the behavior of the structure, especially under impact loading. This report provides details of a newly developed orthotropic material model that has three distinct sub-models for describing deformation, damage, and failure of general composites, and has been implemented in the commercial finite element program, LS-DYNA, as *MAT_213 (*MAT_COMPOSITE_TABULATED_PLASTICITY _DAMAGE). The model is driven by tabulated data that can be generated using laboratory tests or via virtual testing. The yield function is a modified form of the Tsai-Wu failure model. A non-associated plastic flow is used. Rate and temperature dependence are supported along with tension-compression asymmetric behavior. The damage sub-model allows for both uncoupled and coupled parameters to be defined. Strain equivalence between the true and the effective stress space permits decoupling of the plasticity and damage calculations. The failure modeling is currently being enhanced and the initial version discussed in this report includes some of the most commonly used failure criteria – principal strain, Tsai-Wu, and a generalized tabulated laminate failure criterion. Part 1 describes the experimental procedures and results from characterizing a widely used aerospace composite – T800-F3900. Part 2 discusses the theory, implementation, verification and validation of the MAT213 material model using the T800-F3900 composite as a test case. Verification tests are carried out using single and multiple element models. Validation tests are carried out using data from impact tests carried out at NASA-GRC involving T800-F3900 composite panels. Part 3 discusses the probabilistic modeling implementation in LS-DYNA to support MAT213 (via *DEFINE_STOCHASTIC_VARIATION_MAT213) and compares the results from deterministic and probabilistic modeling of impact events.

1. DEVELOPMENT OF A COMPOSITE FINITE ELEMENT MODEL

1.1 BALLISTIC IMPACT TEST AND SIMULATION

1.1.1 Ballistic Impact Test

NASA conducted two series of ballistic impact tests of T800/F3900 composite panels: (1) low-velocity impact tests of unidirectional composite panels, and (2) high-velocity impact tests of cross-ply composite panels. The ballistic impact tests were carried out to validate the developed material model *MAT_213.

The low-velocity impact tests are carried out to observe the elastic response of the composite plate under a dynamic impact. For the low-velocity impact tests, a 16-ply T800/F3900 composite panel with the dimensions 12" x 12" x 0.122" was impacted by a blunt projectile with a weight of 50.8 grams and a radius of 1.996". The fiber direction of the panel in the test was chosen to run vertically. The cylindrical clamping of the panel has an inner radius of 5" and an outer radius of 6". The projectile and plate setup are shown in figure 1.1. The low-velocity impact test results are summarized in table 1.1. Due to gravitation, the points of impact of the projectile in the LVG905 and the LVG906 tests lay 1.6" and 0.7" below the center of the panel, respectively.

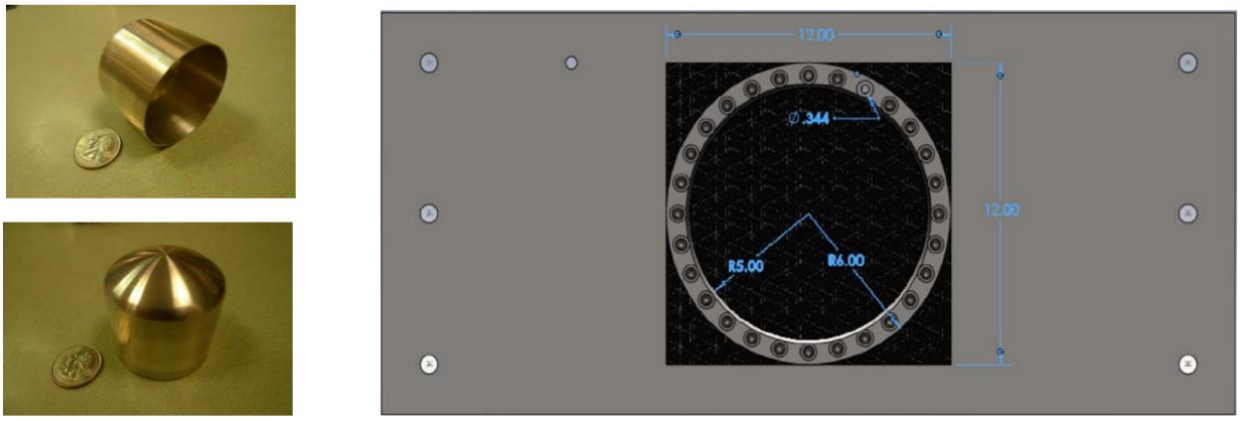

(a) (b)

Figure 1.1. Setup of the low-velocity impact test: (a) projectile, and (b) plate setup

Table 1.1. Low-velocity impact test results

Test ID	Impact velocity (ft/sec)	Exit velocity (ft/sec)	Rebound velocity (ft/sec)
LVG905	23.3	Contained no damage	69.39
LVG906	27.4	Contained no damage	not measured
-	36.5	-	

Test ID	Impact velocity (ft/sec)	Exit velocity (ft/sec)	Rebound velocity (ft/sec)
LVG 903	46	Contained one crack	
LVG 897	101.2	Contained one crack	
LVG 898	~145	Contained three cracks	
-	200	-	
LVG 888	507.4	Penetrated	

The high-velocity impact tests are conducted to identify the ballistic limit velocity of the T800/F3900 composite panel. The general test setup was similar to the previously described low-velocity impact tests, except for the composite panel. The panel was made of T800S/3900-2B[P2352W-19] BMS8-276 Rev-H-Unitape fiber/resin unidirectional composite in a layup of $[0, 90, +45, -45]_{2S}$. The dimension of the panel is 12" x 12" x 0.122", which is the same as the one in the low-velocity impact test. The high-velocity impact test results are summarized in table 1.2.

Table 1.2. High-velocity impact test results

Test ID	Impact velocity (ft/sec)	Exit velocity (ft/sec)	Rebound velocity (ft/sec)
LVG1065	115.96	-	69.39
LVG1071	155.00	-	not measured
LVG1067	155.38	-	83.83
LVG1073	172.34	-	89.39
LVG1072	172.70	-	not measured
LVG1069	177.91	-	78.68
LVG1070	181.21	-	94.39
LVG1068	182.13	-	97.22
LVG1066	185.10	-	104.35
LVG1064	237.39	-	116.01
LVG1075	385.03	-	46.44
LVG1074	417.01	25.38	-
LVG1076	453.27	114.28	-
LVG1063	534.80	262.90	-

1.1.2 Ballistic Impact Simulation

Based on the physical test described above, a baseline simulation model was set up similarly with single point constraints in the region of the clamping. The projectile was moved away from the center in fiber direction (global x-direction) to account for the impact of 1.6" (LVG905) and 0.7" (LVG906) below the center of the panel. Figure 1.2 shows the simulation setup for LVG906 with single point constraints and the projectile impacting off center. The material of the composite panel was defined by *MAT_213,

which was developed by Arizona State University (ASU) based on the series of material tests.

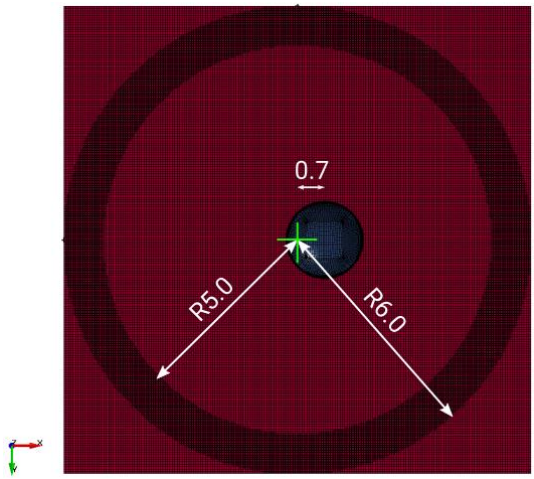

Figure 1.2. Baseline simulation setup of low-velocity impact test

Figure 1.3 shows a fringe plot of the z-displacement of LVG 906 in the test and the simulation at the time of maximum z-displacement. The general shape of the contour lines in the fringe plots shows a good correlation between test and simulation. As previously mentioned, the center of impact in test and simulation was about 0.7" below the center of the plate. The point of maximum z-displacement, however, showed a different location in test and simulation. In the test, the maximum z-displacement occurred above the center of the panel whereas, in the simulation, the point of maximum z-displacement lay between the center of the panel and the center of the impact.

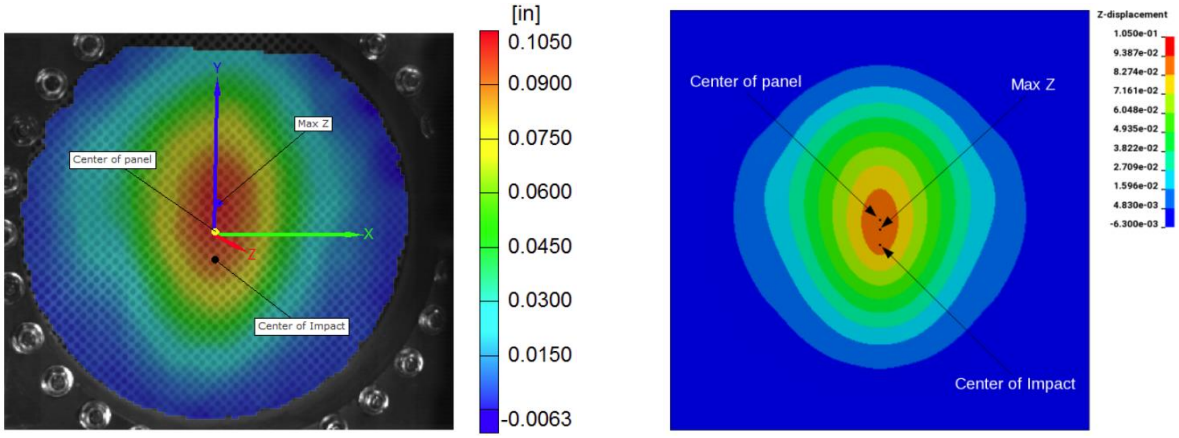

(a) (b)

Figure 1.3. Fringe plots of the z-displacement: (a) test, and (b) simulation

In figure 1.4, the z-displacement over time in the simulation at the impact point, the center of the plate, and the point of maximum z-displacement can be seen. Additionally, the point of maximum z-displacement at the center of the plate in the physical test is shown. The plate was meshed with four fully integrated elements through the thickness and an element aspect ratio of 1:1 (length:height), resulting in a total element number of 620,944.

In the simulation, all three measuring points show very little variation in their maxima as well as the time of occurrence. All three curves show a lower maximum than measured in the test at the center of the plate and at the point of maximum z-displacement. The period of the three simulation curves is shorter than the test displacement curves, indicating a stiffer response of *MAT_213.

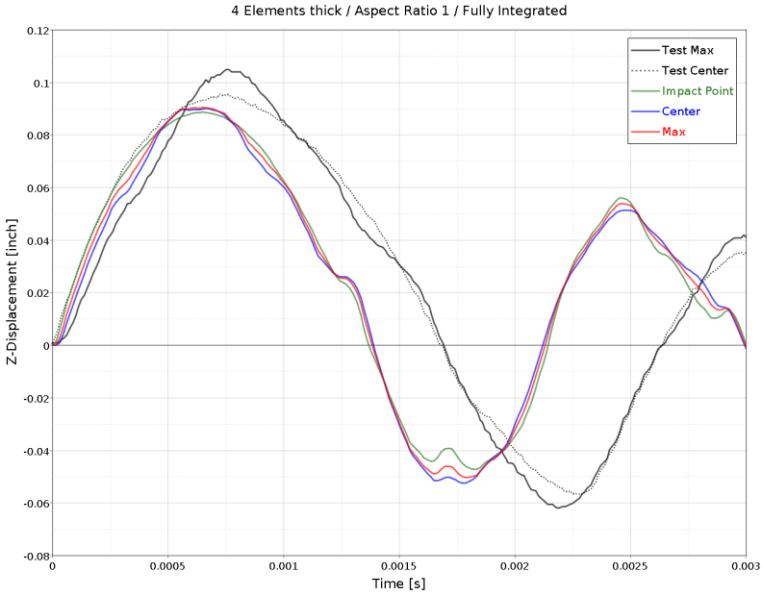

Figure 1.4. Z-displacement curves at various points

1.2 CONVERGENCE STUDY

The convergence of various simulation parameters was studied using the baseline simulation model developed above. For a parametric study, several variables were changed and their influence on the displacement results in low-velocity impact simulations was analyzed. To get the first simulation results faster, the number of elements can be minimized by reducing the number of elements through the thickness and/or by increasing the aspect ratios of the used elements. However, the aim is to satisfactorily balance the accuracy and the computing resources by using enough elements to not influence the results drastically. In the study, two, four, and eight elements through the thickness, with aspect ratios of 1:1, 2:1, 5:1, and 10:1 (length:height) were used. Apart from this mesh sensitivity study, the influence of different hourglass control types and element formulations (fully vs. reduced) were

analyzed. For this purpose, three hourglass types (six, nine, and ten) with reduced integration points were used.

Table 1.3 shows all 47 simulations, the used variables, total number of elements of the plate, the resultant x-coordinate (distance from the center of a plate) where the maximum z-displacement occurred, the maximum z-displacement and the percent error in comparison to the test, the time of occurrence of the maximum z-displacement and the percent error, the percentage of hourglass energy with respect to the total energy at the last time step and additionally the CPU time of the specific simulation. Simulations with an aspect ratio of 1:1 and 8 elements through the thickness were not conducted due to the high CPU times on the available cluster.

Table 1.3. Summary of convergence study

Case ID	# of Elements through Thickness	Aspect Ratio	Total # of elements of plate	Hourglass control	Integration	X-Coord. of Max. Z disp. (in)	Max. Z-Disp. (in)	Max. Z-Disp. (%)	Max. Z-Disp. Time (s)	Max. Z-Disp. Time (%)	Hourglass Energy/ Total Energy (%)	CPU Time (min)
LVG 906	-	-	-	-	-	0.7	1.05E-01	-	7.50E-04	-	-	-
7	2	1:1:1	78,408	1	reduced	0.182	1.00E-01	4.53	6.36E-04	15.16	11.56%	6
13				6		0.242	9.98E-02	4.93	6.36E-04	15.16	0.54%	7
21				9		0.242	9.98E-02	4.93	6.36E-04	15.16	0.80%	7
25				10		0.182	9.98E-02	4.94	6.36E-04	15.17	>99%	1
1				no	full	0	9.38E-02	10.68	6.21E-04	17.20	0.00%	39
10		2:2:1	20,000	1	reduced	0.24	1.00E-01	4.50	6.51E-04	13.15	19.70%	2
16				6		0.24	9.98E-02	4.92	6.36E-04	15.17	0.41%	2
22				9		0.12	9.99E-02	4.89	6.36E-04	15.17	0.45%	2
26				10		0.24	9.98E-02	4.91	6.36E-04	15.17	>99%	5
4				no	full	0	9.36E-02	10.89	6.21E-04	17.19	0.00%	11
19		5:5:1	3,200	6	reduced	0.3	1.00E-01	4.72	6.82E-04	9.12	0.44%	1
23				9		0.3	1.00E-01	4.80	6.82E-04	9.10	0.63%	1
27				10		0.3	1.00E-01	4.79	6.67E-04	11.13	>99%	2
49				no	full	0.3	8.92E-02	15.08	6.21E-04	17.19	0.00%	3
20		10:10:1	800	6	reduced	0	1.04E-01	0.55	7.12E-04	5.07	1.93%	1
24				9		0	1.05E-01	0.29	6.97E-04	7.09	1.30%	1
28				10		0	1.04E-01	0.56	6.82E-04	9.11	>99%	1
52				no	full	0.6	8.40E-02	20.00	6.21E-04	17.19	0.00%	1
8	4	1:1:1	620,944	1	reduced	0.213	9.24E-02	11.98	5.91E-04	21.23	3.52%	75
14				6		0.183	9.23E-02	12.12	5.91E-04	21.22	0.00%	89
31				9		0.183	9.23E-02	12.12	5.91E-04	21.22	0.04%	84
35				10		0.213	9.23E-02	12.11	5.91E-04	21.22	>99%	214
2				no	full	0.274	9.05E-02	13.79	6.51E-04	13.14	0.00%	588
11		2:2:1	156,816	1	reduced	0.242	9.26E-02	11.79	5.91E-04	21.22	7.03%	19
17				6		0.182	9.24E-02	11.97	5.91E-04	21.23	0.04%	24
32				9		0.182	9.25E-02	11.93	5.91E-04	21.22	0.05%	23
36				10		0.182	9.25E-02	11.95	5.91E-04	21.22	>99%	56
5				no	full	0.242	9.07E-02	13.67	6.51E-04	13.14	0.00%	148
29		5:5:1	25,600	6	reduced	0.15	9.31E-02	11.30	5.91E-04	21.22	0.09%	5
33				9		0.15	9.32E-02	11.28	5.91E-04	21.23	0.15%	5
37				10		0.15	9.31E-02	11.30	5.91E-04	21.22	>99%	11
50				no	full	0.15	9.00E-02	14.28	6.51E-04	13.14	0.00%	26
30		10:10:1	6,400	6	reduced	0.3	9.33E-02	11.19	6.36E-04	15.16	0.26%	2
34				9		0.3	9.33E-02	11.12	6.82E-04	9.10	0.39%	2

Case ID	# of Elements through Thickness	Aspect Ratio	Total # of elements of plate	Hourglass control	Integration	X-Coord. of Max. Z disp. (in)	Max. Z-Disp. (in)	(%)	Max. Z-Disp. Time (s)	(%)	Hourglass Energy/ Total Energy (%)	CPU Time (min)
38				10		0.3	9.33E-02	11.19	6.82E-04	9.11	>99%	5
53				no	full	0.3	8.64E-02	17.74	6.06E-04	19.20	0.00%	8
12				1		0.274	9.07E-02	13.58	5.91E-04	21.22	2.02%	260
18	8	2:2:1	1,241,888	6	reduced	0.182	9.24E-02	12.00	6.05E-04	19.33	0.00%	3556
42				9		0.182	9.24E-02	12.00	6.05E-04	19.33	0.00%	3585
6				no	full	0.180	9.20E-02	12.38	6.03E-04	19.60	0.00%	N/A
39				6		0.152	9.08E-02	13.54	5.61E-04	25.26	0.02%	54
43		5:5:1	199,712	9	reduced	0.152	9.08E-02	13.57	5.61E-04	25.26	0.05%	51
47	8			10		0.152	9.08E-02	13.55	5.61E-04	25.26	>99%	139
40				6		0.15	9.14E-02	12.98	5.76E-04	23.24	0.04%	16
44		10:10:1	51,200	9	reduced	0.15	9.13E-02	13.02	5.76E-04	23.24	0.09%	16
48				10		0.15	9.14E-02	12.99	5.76E-04	23.24	>99%	39
54				no	full	0.15	8.96E-02	14.66	6.67E-04	11.12	0.00%	100

Number of Elements through Thickness

For an analysis of the effects of different numbers of elements through the thickness, two, four, and eight elements were used with different aspect ratios. Figure 1.5 shows the results of the full integration scheme, and figure 1.6 shows the results of the hourglass type 6.

In the case of fully integrated elements, the displacement peak and time of occurrence does not change significantly with the number of layers through the thickness for the lower aspect ratios. Only for aspect ratio 10:1, two elements through the thickness provide very poor results. In the case of hourglass control type 6, for all aspect ratios, the simulation with two elements through the thickness shows a higher displacement peak and a longer period. The change of the curve from four to eight layers is relatively small, indicating the reach of mesh convergence. The simulations of aspect ratios 1:1 and 2:1 were not conducted due to the high CPU time on the available cluster.

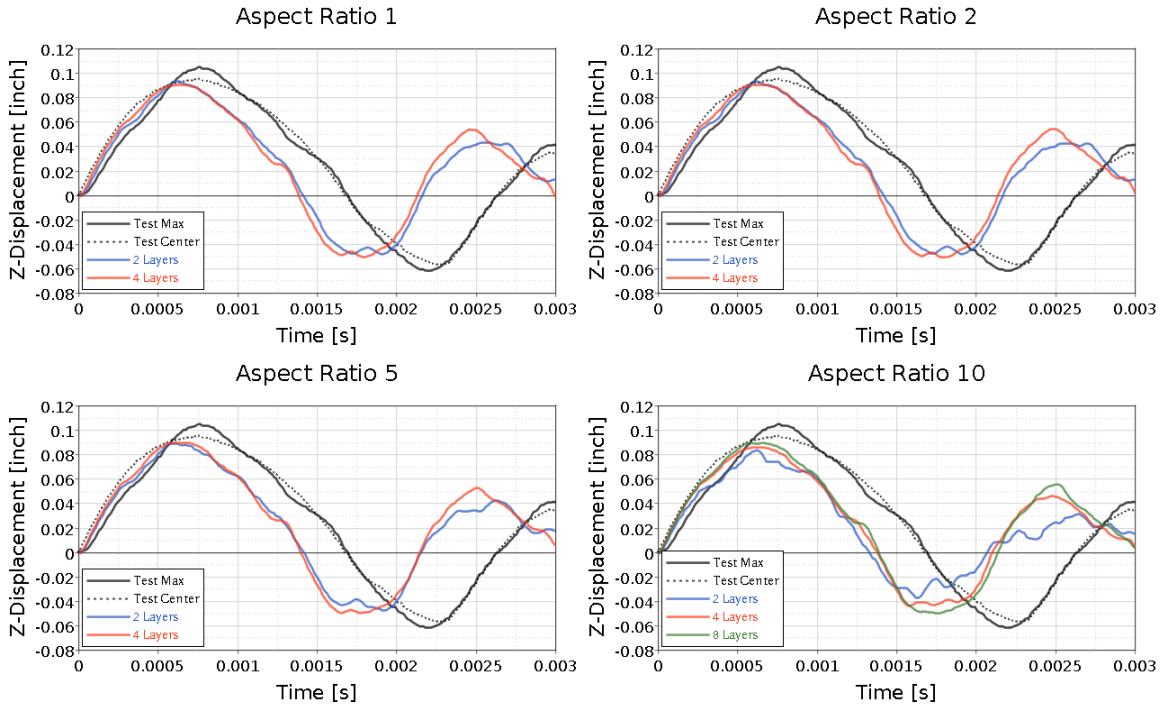

Figure 1.5. Z-displacement plots of the cases with full integration scheme

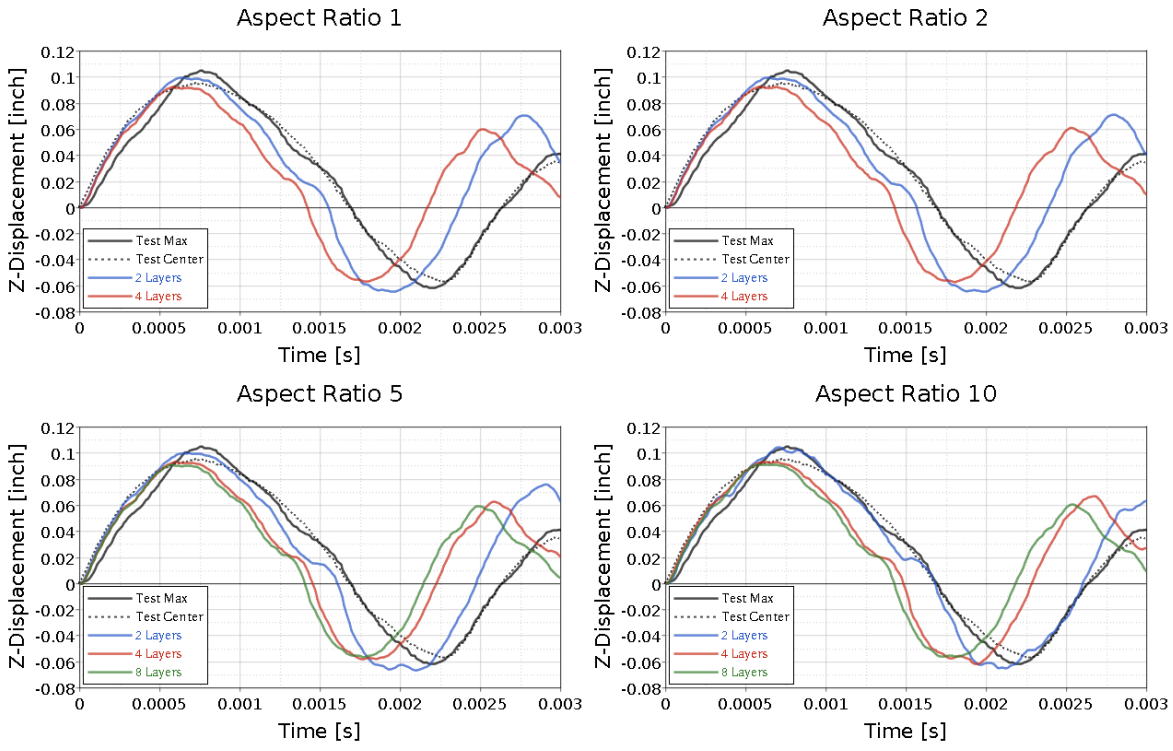

Figure 1.6. Z-displacement plots of the cases with the hourglass control type 6

Aspect Ratio

The influence of different aspect ratios on the displacement curve was analyzed with aspect ratios 1:1, 2:1, 5:1, and 10:1. Figure 1.7 (two elements through the thickness) and figure 1.8 (four elements through the thickness) show the results. The effect on the maximum displacement and time of its occurrence was relatively little for two elements through the thickness and even lower for four elements through the thickness. Only the aspect ratio of 10:1, with two layers, produced poor results. For the three different types of hourglass control, a similar behavior was observed.

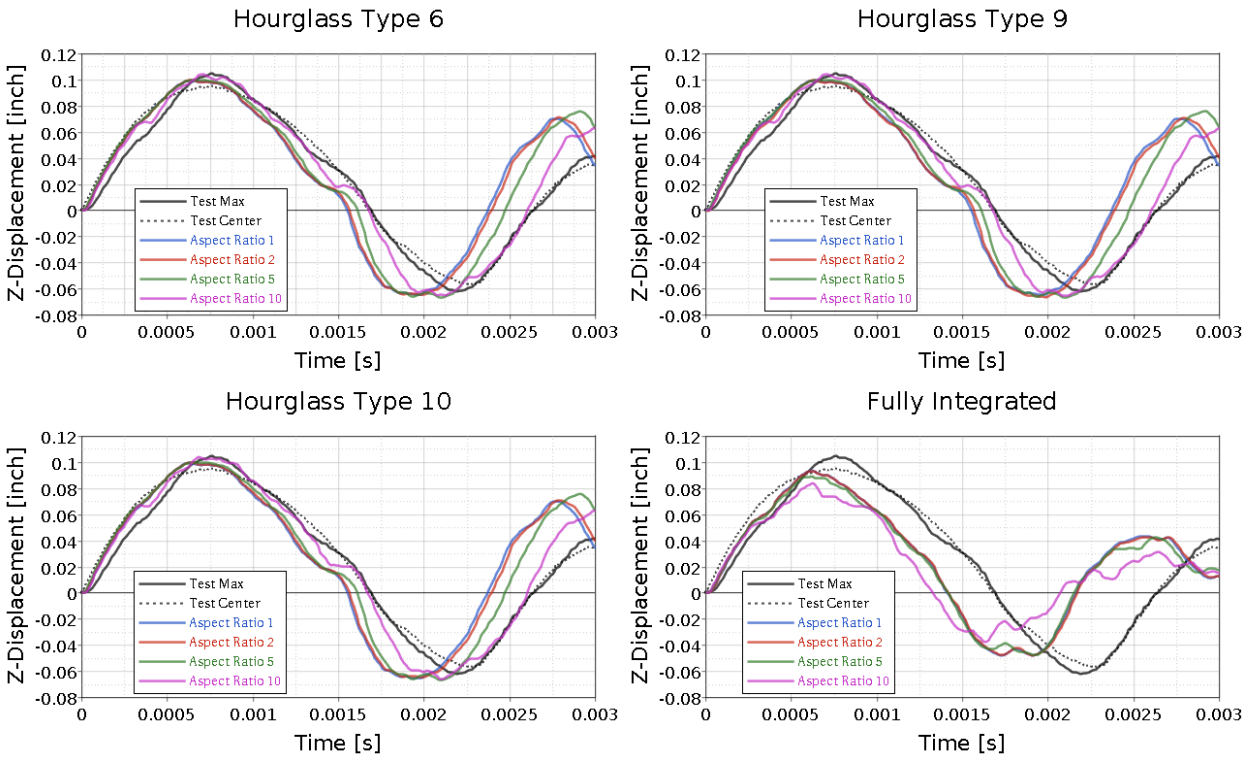

Figure 1.7. Z-displacement plots of the cases with two elements through thickness

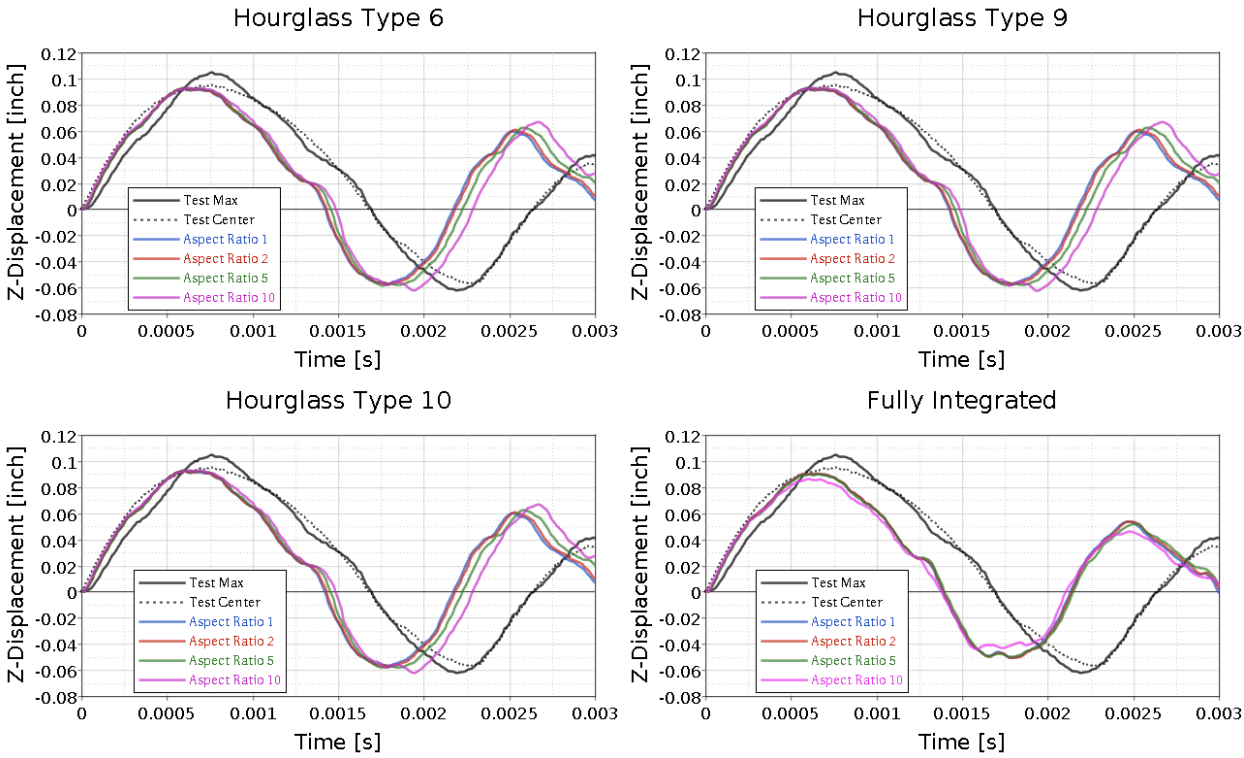

Figure 1.8. Z-displacement plots of the cases with four elements through thickness

Hourglass Control

Whether the use of different types of hourglass control has an effect on the displacement results was analyzed by using type six (Belytschko-Bindeman), nine (Puso enhanced assumed strain stiffness form), and ten (Cosserat Point Element) hourglass control. In figure 1.9, the results for a different number of elements through the thickness are shown. In all cases the curves lie on top of each other, meaning the different types of hourglass control don't influence the displacement results.

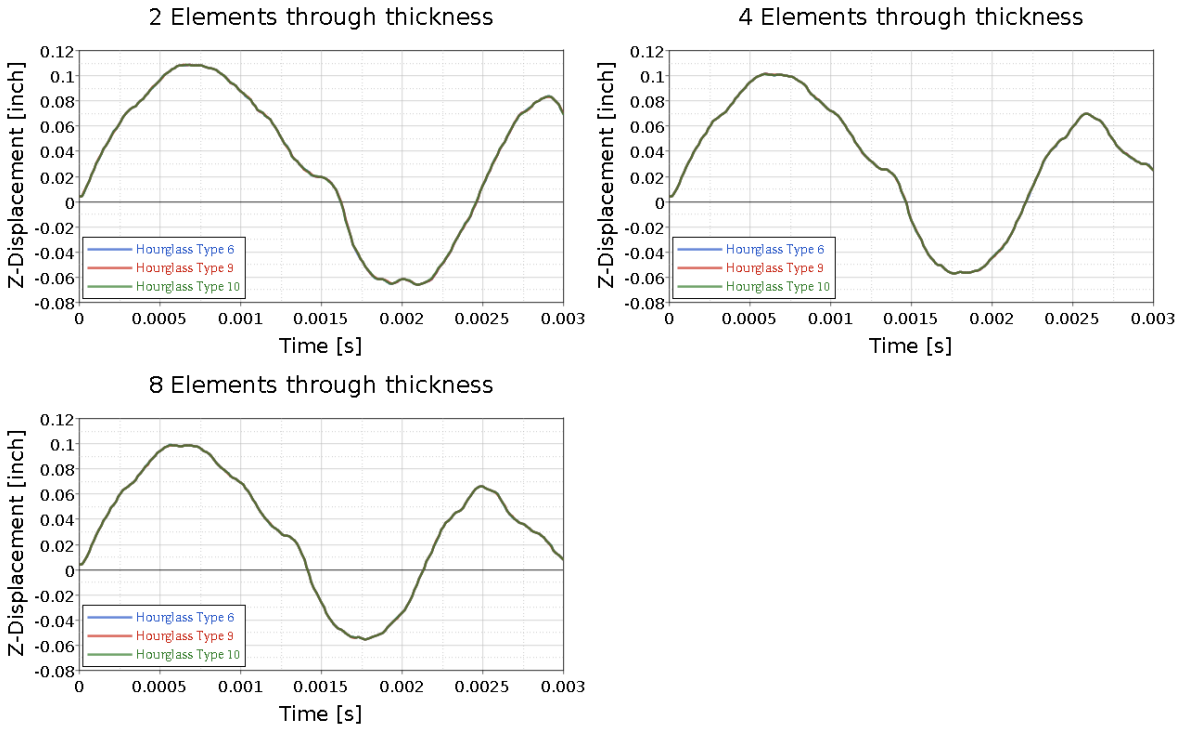

Figure 1.9. Z-displacement plots of the cases with Aspect ratio 5:5:1

Even though all types of hourglass control produced the same displacement curves, an abnormality with the hourglass energy of type ten hourglass control was observed. As figure 1.10 shows, the hourglass energy grows to abnormally high values, being the dominating energy with over 99% of the total energy. The deformation of the plate, however, seemed to happen normally. A reason for this behavior was not found.

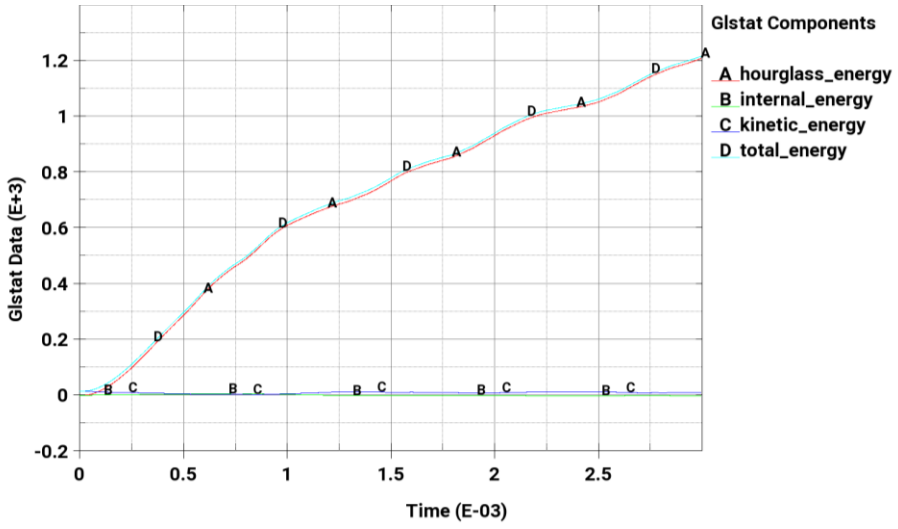

Figure 1.10. Energy plots in the case with the hourglass control type 10

CPU Times

Different types of hourglass control or integration schemes usually lead to different computation times of the simulations. To analyze how expensive these different methods are, the number of elements was plotted over the CPU time needed to perform the analysis. Figure 1.11 shows the results. As one would expect, the fully integrated element formulation needed the most resources and the standard hourglass control the least. Hourglass control type 10 was the second most expensive, and type 6 and 9 took about the same amount of CPU time to complete.

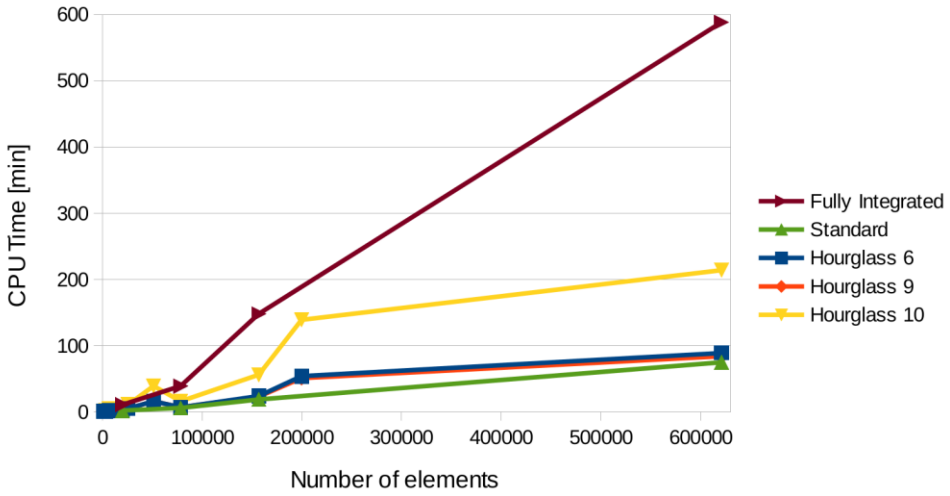

Figure 1.11. CPU times

Summary

In the parametric study, the Low-Velocity Impact Test (LVG906) on a 16-ply T800/F3900 composite panel was simulated using *MAT_213. Different types of hourglass control, aspect ratios, and numbers of elements through the thickness were used to analyze their influence on the displacement results of the composite panel.

The results suggest that different types of hourglass control can be used with *MAT_213 without compromising the results. After comparing the results of different numbers of elements through the thickness, it can be said that by using more than four elements through the thickness the displacement results in this low-velocity impact simulation cannot be improved significantly. The simulation showed relatively low sensitivity to different element aspect ratios. To reduce CPU time, the user can choose a higher aspect ratio without compromising the results significantly. Additionally, if low computation times are to be achieved, the standard type hourglass control should be chosen.

1.3 BOUNDARY CONDITION

Several simulation models were set up to study the effects of different boundary conditions on the simulation results of the ballistic impact test LVG906, in which a projectile hits a 16-ply unidirectional composite plate with a velocity of 27.4 ft/sec.

Figure 1.12(a) shows the geometry of the physical test setup in which the composite plate was clamped between a steel plate (yellow) and a steel ring (purple) by bolts. A detailed FE model of this setup, including the bolts, was built up as shown in figure 1.12(b). The bolts are connected on the top and bottom using nodal rigid bodies. The total number of solid elements in this model was about 6 million, of which the composite plate, modeled with four elements through the thickness, accounted for 300,000 elements.

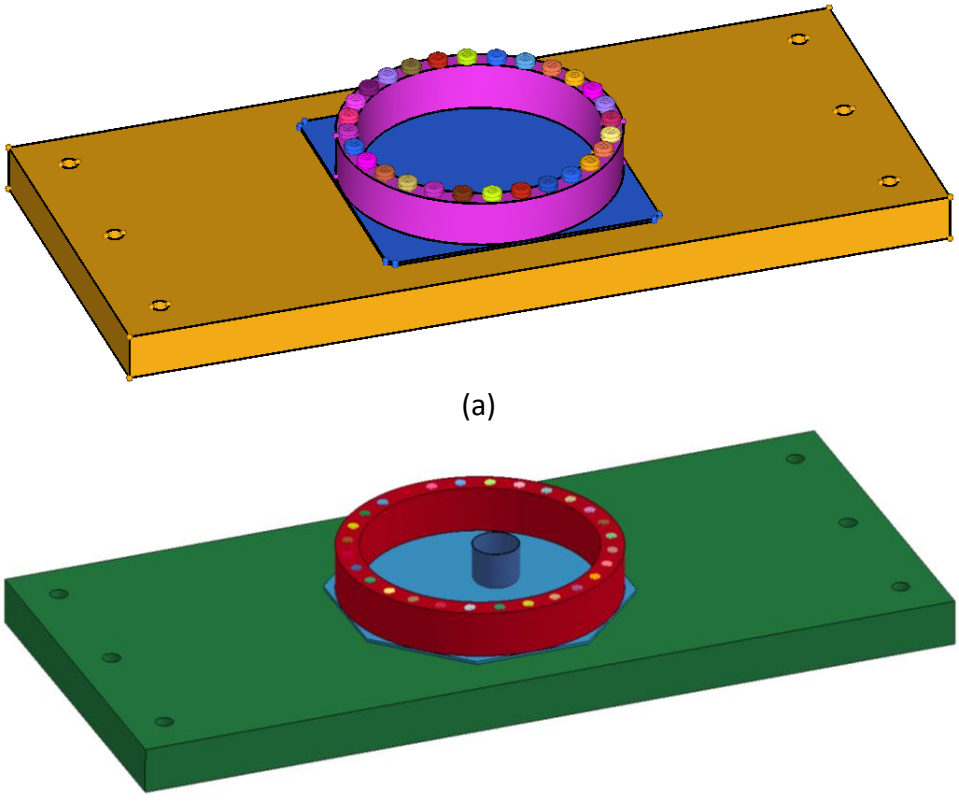

(a)

(b)

Figure 1.12. Boundary setup of ballistic impact tests: (a) test, and (b) simulation

The test and simulation results of this setup can be seen in figure 1.13, with the test results shown in black and the detailed simulation model in red. In the same graph, the dashed blue line shows the results of the baseline simulation, in which a round composite plate was fully constrained on the edges of the clamped region. This boundary condition was chosen in previous studies of the ballistic impact test. In the

baseline simulation, the period of the deformation is significantly shorter than in the test, suggesting a too stiff response. Closer to the test are the results of the detailed model showing a longer period than in the baseline simulation.

However, it is not very practical to use the detailed model in extensive studies due to the high number of elements and consequently very long CPU times (about 60 hours in this case). Simplifications to these detailed boundary conditions had to be made, which was achieved by constraining a round plate in the clamping region in impact direction, modeling the interaction between the clamping plates and the composite plate. A visualization of the nodal constrained in this setup can be seen in figure 1.14(a). The results these boundary conditions produce are shown as the green curve in figure 1.13, which are very similar to the results of the detailed model. This suggests that modeling the clamping region as not being constrained perpendicular to the impact direction is closer to the physical boundary conditions.

However, when this boundary condition is applied to higher-velocities, the simulation results worsen by making the response too soft. Therefore, the nodes in the region where the bolts would be located are additionally constrained in plane as shown in figure 1.14(b). With this set of boundary conditions, the resultant z-displacement curve is shown in figure 1.13 in purple. The response is slightly stiffer than when using only constraints in impact direction, but an improvement of the baseline model towards the test results in both high- and low-velocity impacts was achieved. The simple boundary setup shown in figure 1.14 was selected in the following impact simulations.

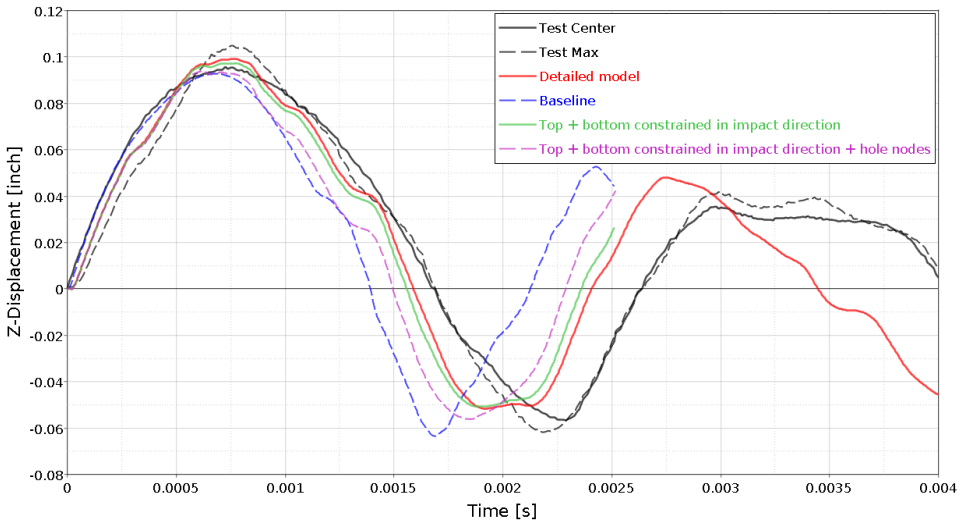

Figure 1.13. Z-displacement curves with various boundary setups

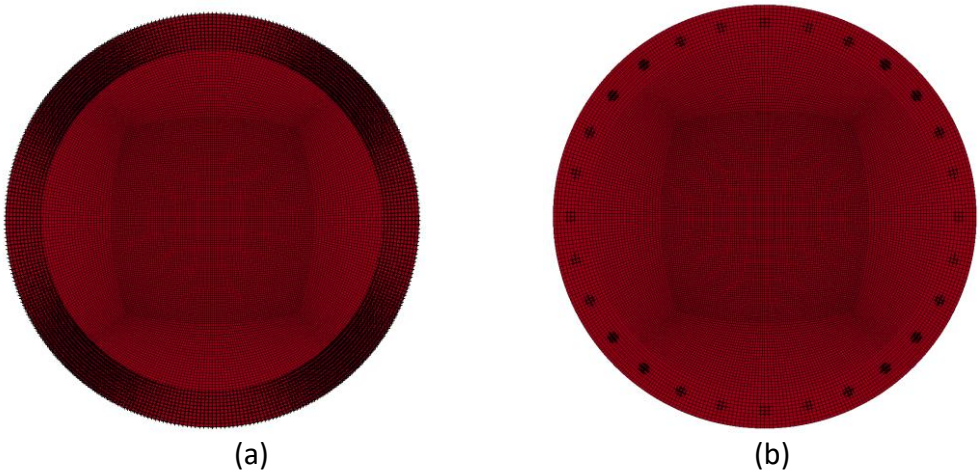

Figure 1.14. Simple boundary setup: (a) clamping constraints, and (b) bolting constraints

1.4 DELAMINATION MODEL

With the increasing capabilities of *MAT_213, simulations of low-velocity impacts on composite plates can help to predict a critical velocity range for which penetration of the plate is expected to occur. To simulate the ballistic impacts more accurately, it is important to include a delamination model. At the time of this study, no test data with regards to delamination of the composite material T800-F3900 was available, and therefore a material with publicly available test and simulation data was chosen for this delamination study.

Brief Overview of Cohesive Laws Currently Available in LS-DYNA

The most common way to model composite delamination in LS-DYNA is a cohesive zone approach modeled by elements or tiebreak contact. LS-DYNA currently offers several different cohesive material laws. The interface element's behavior is governed by a traction-separation curve which relates the element stress (traction) to mode I (opening) and mode II (shear) nodal displacements.

The main distinguishing factor between the cohesive material laws is the shape of the traction-separation curve. *MAT_184 (or *MAT_COHESIVE_ELASTIC) is a simple linear elastic model. A bilinear cohesive law, as shown in figure 1.15, is the basis for *MAT_138 (or *MAT_COHESIVE_MIXED_MODE). It includes a quadratic mixed-mode delamination criterion and a damage formulation. Both MAT185 (or *MAT_COHESIVE_TH) and *MAT_240 (or *MAT_COHESIVE_MIXED_MODE_ELASTOPLASTIC_RATE) use a trilinear traction-separation law (figure 1.16), with an ideal plastic region. An arbitrary traction separation curve can be defined with *MAT_186 (or *MAT_COHESIVE _GENERAL).

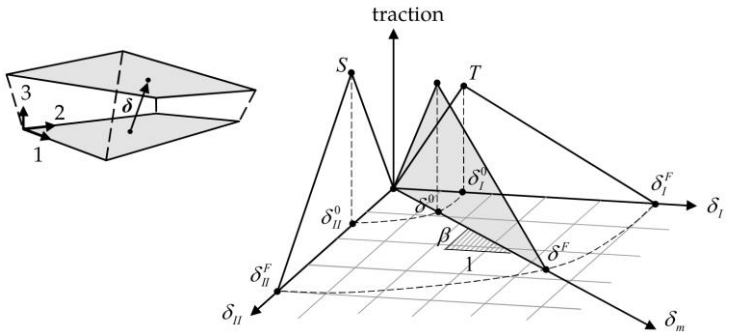

Figure 1.15. *MAT_138, bilinear mixed-mode traction-separation law [1]

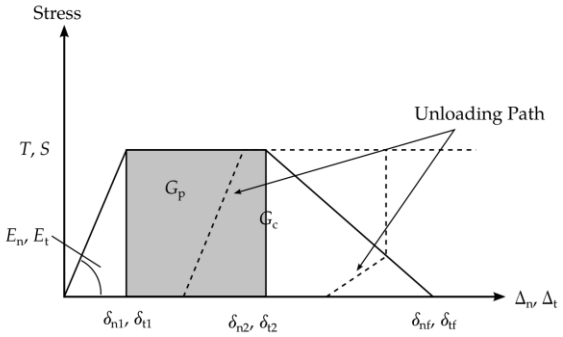

Figure 1.16. *MAT_240, trilinear traction-separation law [1]

When using *MAT_240, the user has the option to incorporate strain rate effects for the strain energy release rate (G_{IC} for Mode I, G_{IIC} for Mode II) and for yield stress (*T* for Mode I, *S* for Mode II). By defining the three parameters G_{I0}, $G_{I\infty}$, and ε_{G1}, the strain rate dependent strain energy release rate can be curve fitted following the equations:

$$G_{IC}(\dot{\epsilon}) = G_{I0} + (G_{I\infty} - G_{I0})\exp\left(\frac{\dot{\epsilon}_{G1}}{\dot{\epsilon}}\right) \quad (1.1)$$

$$G_{IIC}(\dot{\epsilon}) = G_{II0} + (G_{II\infty} - G_{II0})\exp\left(\frac{\dot{\epsilon}_{G2}}{\dot{\epsilon}}\right) \quad (1.2)$$

Figure 1.17 shows an example of how experimental results of strain rate dependent strain energy release rate can be curve fitted using Eq. (1.1).

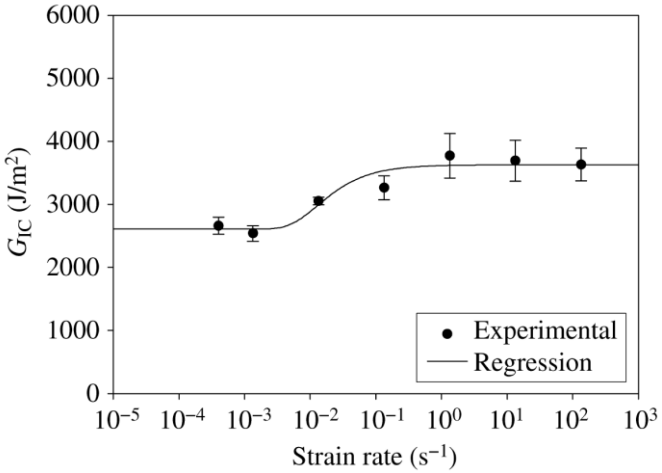

Figure 1.17. Strain rate dependent strain energy release rate in mode I [2]

To define strain rate dependent yield stresses for Mode I and II, a linear logarithmic or quadratic logarithmic regression can be chosen to curve fit the experimental results:

$$T(\dot{\epsilon}) = T_0 + T_1 \langle ln \frac{\dot{\epsilon}}{\dot{\epsilon}_T} \rangle \quad \text{or} \quad T(\dot{\epsilon}) = T_0 + T_1 \langle ln \frac{\dot{\epsilon}}{\dot{\epsilon}_T} \rangle^2 \tag{1.3}$$

$$S(\dot{\epsilon}) = S_0 + S_1 \langle ln \frac{\dot{\epsilon}}{\dot{\epsilon}_S} \rangle \quad \text{or} \quad S(\dot{\epsilon}) = S_0 + S_1 \langle ln \frac{\dot{\epsilon}}{\dot{\epsilon}_S} \rangle^2 \tag{1.4}$$

Figure 1.18 illustrates an example how Eq. (1.3) and (1.4) are used to curve fit experimental results for strain rate dependent yield stresses in mode I.

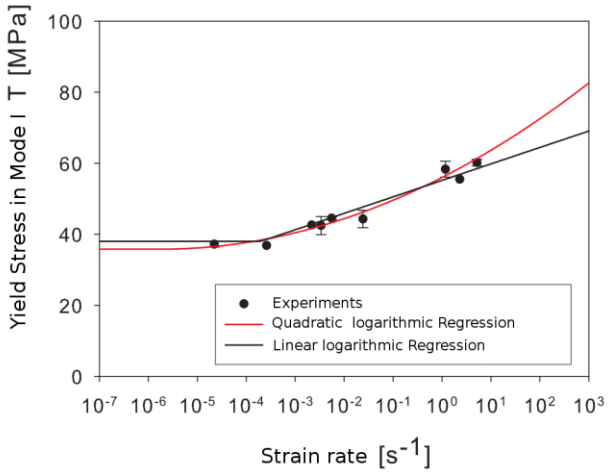

Figure 1.18. Strain rate dependent yield stress in mode I [2]

Initial Material Input for Delamination Study

In 1990, Juntti et al. evaluated methods for the mixed-mode bending test and therefore conducted delamination tests on a toughened resin HTA/6376C carbon/epoxy prepreg produced by Ciba Geigy [3]. The Double Cantilever Beam (DCB) test for the opening Mode I and the End-Notched Flexure (ENF) test for Mode II were used. Based on the results obtained in this study, Harper et al. conducted the analysis of different cohesive zone lengths in numerical simulations of composite delamination using *MAT_138 [4]. The material input that was used in this work is shown in table 1.4. In addition to the input for *MAT_138, a second cohesive material model (*MAT_240) was used with the input parameters shown in table 1.5. By only defining the shown parameters, *MAT_240 is expected to behave like *MAT_138 because no ideal plastic region and no strain rate dependency are defined. With additional test results available, these options could be used in the future.

Table 1.4. *MAT_138 of HTA/6376C composite [4]

Variable	Description	LS-DYNA Variable	Value	Unit
K_I	Elastic Stiffness (normal direction)	EN	1.0e5	N/mm^3
K_{II}	Elastic Stiffness (in plane)	ET	1.0e5	N/mm^3
G_{IC}	Critical strain energy release rate (Mode I)	GIC	0.26	N/mm
G_{IIC}	Critical strain energy release rate (Mode II)	GIIC	1.002	N/mm
$\sigma_{I,max}$	Interfacial strength (Mode I)	T	30.0	MPa
$\sigma_{II,max}$	Interfacial strength (Mode II)	S	60.0	MPa

Table 1.5. *MAT_240 of HTA/6376C composite

Variable	Description	LS- DYNA Variable	Value	Unit
EN * THICK	The Young's modulus of the material	EMOD	1000.0	N/mm^2
ET * THICK	The shear modulus of the material	GMOD	1000.0	N/mm^2
	GT.0.0: Cohesive thickness LE.0.0: Initial thickness is calculated from nodal coordinates	THICK	0.1	mm
G_{IC}	Energy release rate GIC in Mode I	G1C_0	0.26	N/mm
$\sigma_{I,max}$	Yield stress in Mode I	T0	30.0	MPa
G_{IIC}	Energy release rate GIIC in Mode II	G2C_0	1.002	N/mm
$\sigma_{II,max}$	Yield stress in Mode II	S0	60.0	MPa

In addition to the cohesive material models, a tiebreak contact was defined. Option 9 in the keyword card of *CONTACT_AUTOMATIC_ONE_WAY_SURFACE_TO_ SURFACE_TIEBREAK describes a discrete crack model with a power law and

Benzeggagh-Kenane damage model which is based on the cohesive material model *MAT_138 [1]. Table 1.6 lists the input required for this option.

Table 1.6. *CONTACT_AUTOMATIC_ONE_WAY_SURFACE TO_SURFACE_TIEBREAK of HTA/6376C composite

Variable	Description	LS- DYNA Variable	Value	Unit
	Exponent in damage model	PARAM	1	-
	Ratio of tangential stiffness to normal stiffness	CT2CN	1	-
E_N	Normal stiffness	CN	1e5	N/mm^3
G_{IC}	Normal strain energy release rate (Mode I)	ERATEN	0.26	N/mm
G_{IIC}	Shear strain energy release rate (Mode II)	ERATES	1.002	N/mm
$\sigma_{I,max}$	Normal failure stress	NFLS	30	MPa
$\sigma_{II,max}$	Shear failure stress	SFLS	60	MPa

The dimensions of the DCB specimen are given as 150 x 20 x 3.1 mm and the initial crack length (a_0) as 35 mm. In the test, the specimen is loaded displacement-controlled and the force acting on the piano hinges is measured. In the simulation, the ends of the specimen are pulled apart by a prescribed motion. Figure 1.19 shows the simulation and test setups. The composite plies are modeled linear-elastically (*MAT_022) while the interface between the plies is modeled using cohesive elements or a tiebreak contact.

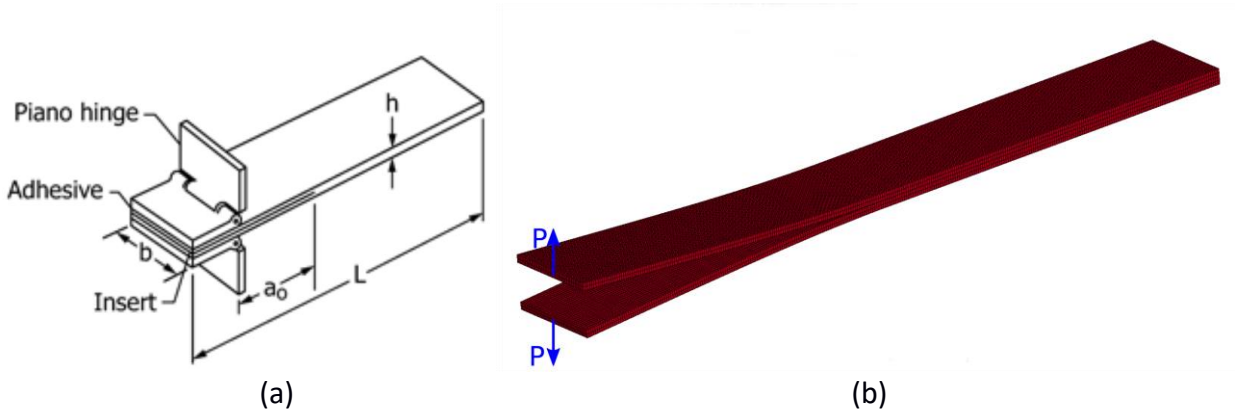

Figure 1.19. Setup of Double Cantilever Beam (DCB) test: (a) test, and (b) simulation.

Figure 1.20 shows the results for the DCB test and simulation with *MAT_138, *MAT_240, and Tiebreak contact. The cohesive element length was 0.25 mm which resulted in a count of 384,000 elements for the plate and 36,800 elements for the cohesive zone. It can be seen that the results for the two cohesive models and the tiebreak contact closely match as anticipated. The slope and maximum, however, do not exactly match the test. This could most likely be improved by refining the mesh or by

optimizing the material parameters. The reason for the slight difference in slope can most likely be found in the composite material definition or the general boundary conditions and geometry, which was not exactly defined in the test description.

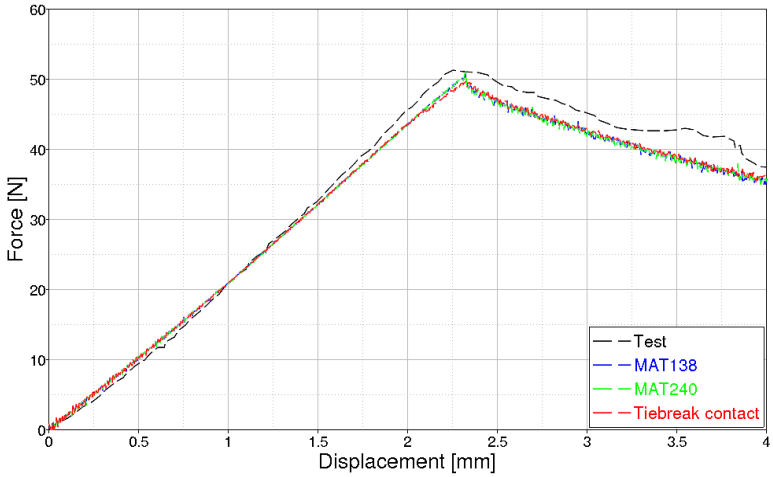

Figure 1.20. DCB result comparison between *MAT_138, *MAT_240, and Tiebreak contact

If a coarser mesh is used (cohesive and *MAT_022 element size = 0.5 mm), as seen in figure 1.21, the slope of the force is much lower. This can be traced back to the coarser mesh of the composite plates and not the cohesive element size. In the beginning of the simulation, no cohesive element fails and therefore they do not influence the results.

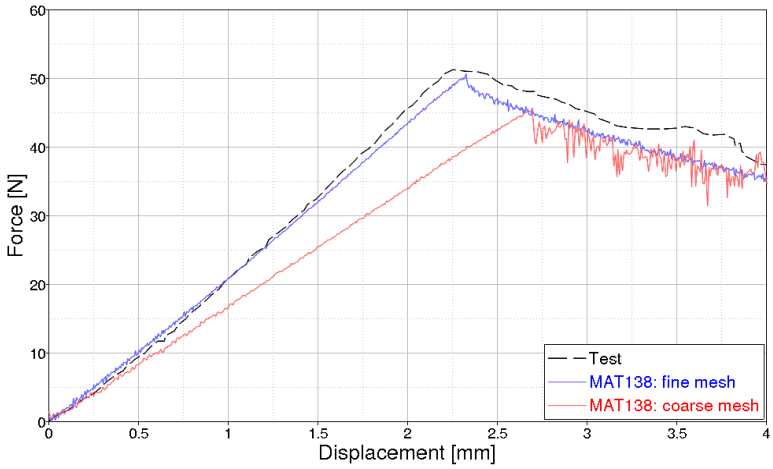

Figure 1.21. Mesh dependency

However, after the maximum force is reached and the crack propagates, the resultant force oscillates more than with the finer mesh size. Figure 1.22 shows how a different cohesive element thickness influences the results. The slope again is slightly lower as

with zero cohesive element thickness and there can be drops in force found while the crack propagates.

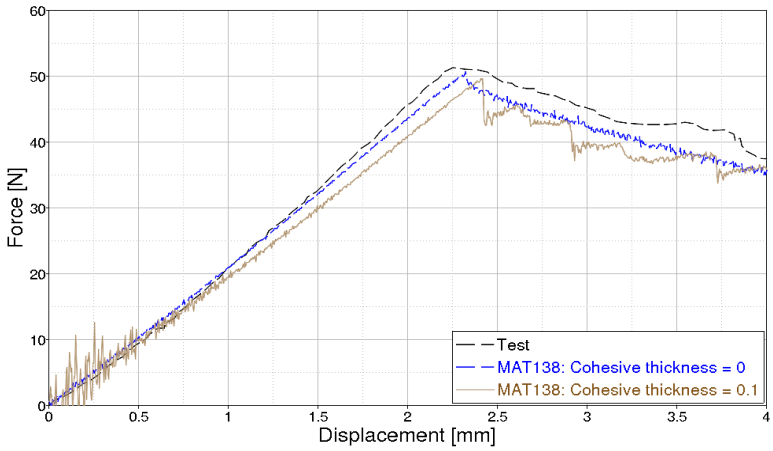

Figure 1.22. Influence of cohesive element thickness

For the ENF test and simulation, the same specimen is used as for the DCB test. The specimen is loaded displacement-controlled as shown in figure 1.23(a) while the force is measured. Due to the bending of the specimen, the interface (cohesive zone) is loaded in Mode II (shear). Figure 1.23(b) shows the simulation setup.

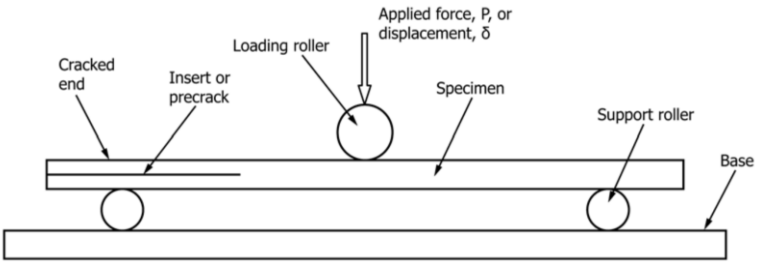

(a)

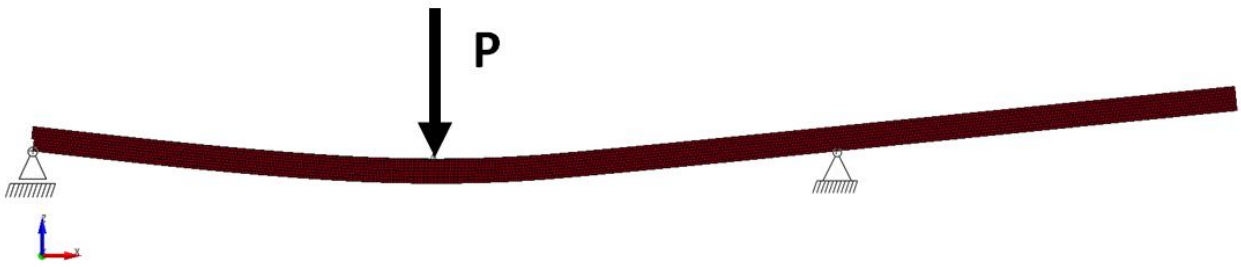

(b)

Figure 1.23. Setup of End-Notched Flexure (ENF) test; (a) test and (b) simulation.

The results of the ENF test can be seen in figure 1.24. Both the tiebreak contact and *MAT_138 method show very similar results and the slopes match the test very well. The time when the crack propagates, however, is earlier in the simulation than the test. Better results can most likely be obtained with optimized material parameters.

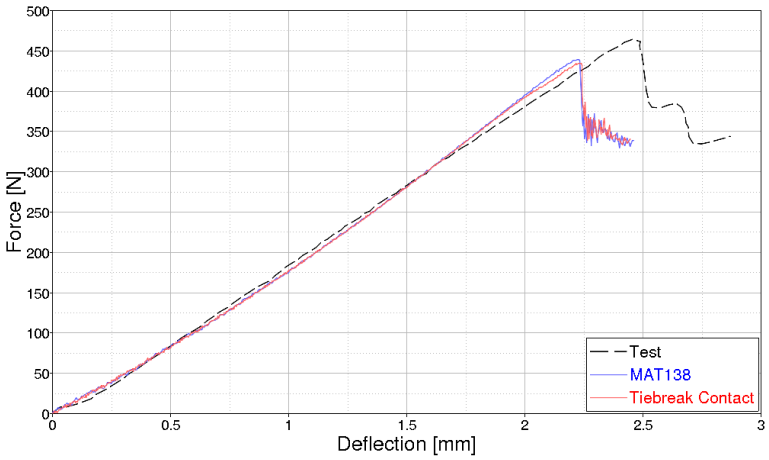

Figure 1.24. ENF Simulation result

Delamination Model for T800/F3900

In the previous delamination session, well-described results of DCB and ENF tests of a toughened resin HTA/6376C carbon/epoxy prepreg, conducted by Juntti et al. [3], were used to identify material parameters for the LS-DYNA cohesive material models *MAT_138 (*MAT_COHESIVE_ MIXED_MODE) and *MAT_240 (*MAT_COHESIVE_ MIXED_MODE_ ELASTOPLASTIC_RATE).

To adapt the obtained material parameters to the composite material T800/F3900, which is the objective of this research, available fracture toughness values from the literature were obtained and compared. Table 1.7 lists the values for Mode I fracture toughness (GIC) and Mode II fracture toughness (GIIC), as identified by various sources.

Table 1.7. Fracture toughness of T800/F3900 composite in literature (*simulative)

Source	Material	GIC (MPa·mm)	GIIC (MPa·mm)
Matsuda et al. [5]	T800H/3900-2	-	1.19 – 2.14
Liu et al. [6]	T800H/3900-2	0.26*	3.15*
Davidson et al. [7]	T800S/3900-2B	-	2.18
Chou et al. [8]	T800/3900-2	-	1.63 – 1.97
Kageyama et al. [9]	T800H/3900-2	0.75	2.05 – 2.09
Nuggehalli [10]	T800S/3900	0.26 – 0.96	1.22 – 4.9
Rhymer et al. [11]	T800/3900-2	-	2.1

Based on the fracture toughness values and the force versus displacement results obtained by Kageyama et al., in the DCB and ENF tests [9], an LS-DYNA cohesive material was defined using *MAT_138. Table 1.8 lists the material input used as a baseline in the following simulations.

Table 1.8. *MAT_138 of T800/F3900 composite

Variable	Description	LS-Dyna Variable	Value	Unit
K_I	Elastic Stiffness (normal direction)	EN	6.16e8	lbf/in^3
K_{II}	Elastic Stiffness (in plane)	ET	6.16e8	lbf/in^3
G_{IC}	Critical strain energy release rate (Mode I)	GIC	4.28	lbf/in
G_{IIC}	Critical strain energy release rate (Mode II)	GIIC	14.5	lbf/in
$\sigma_{I,max}$	Interfacial strength (Mode I)	T	10,000	psi
$\sigma_{II,max}$	Interfacial strength (Mode II)	S	15,000	psi

The dimensions of the DCB specimen are given as 5.512 x 0.98 x 0.118 inches and the initial crack length as 1.693 inches. In the test, the specimen is loaded displacement-controlled and the force acting on the piano hinges is measured. In the simulation, the ends of the specimen are pulled apart by a prescribed motion. The composite plies are modeled linearly elastically (*MAT_022) while the interface between the plies is modeled using cohesive elements. Figure 1.25 shows the force vs. displacement results obtained by Kageyama et al. [9] in the test in comparison with the simulation results using the material input shown in table 1.8.

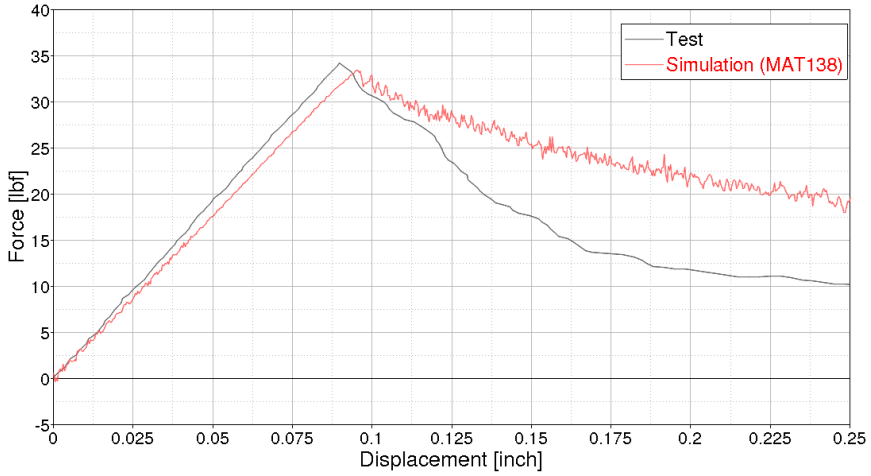

Figure 1.25. DCB Test and Simulation

The maximum force obtained in the simulation matches the test very well. The lower slope after the peak force is reached can be explained by the change of the fracture toughness with crack length as measured by Kageyama et al. [9]. After the crack is

initiated, the measured Mode I fracture toughness drops significantly, which cannot be incorporated into the simulation model.

For the ENF test and simulation, the same specimen is used as for the DCB test. The specimen is loaded displacement controlled while the force and the tip displacement is measured. Due to the bending of the specimen, the interface (cohesive zone) is loaded in Mode II (shear). Figure 1.26 shows the force vs. displacement results obtained by Kageyama et al. [9] in the test in comparison with the simulation results. Again the peak force at which the delamination crack starts to propagate matches very well in test and simulation.

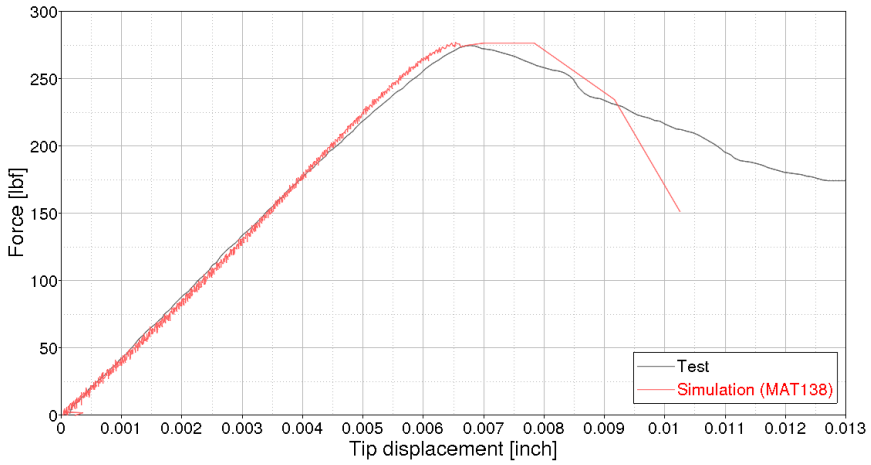

Figure 1.26. ENF Test and Simulation

The influence of different cohesive material parameters on the force versus displacement results was studied. The Elastic Stiffness in the normal direction (EN) has very little influence on the force versus displacement results (figure 1.27).

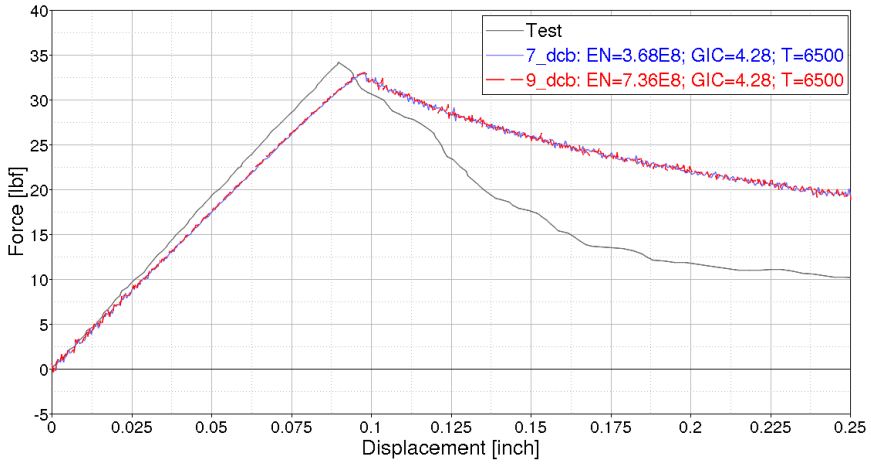

Figure 1.27. Effect of EN on DCB results

A decrease of the Interfacial strength (Mode I) slightly decreases the slope of the force versus displacement curve until the maximum force is reached (figure 1.28).

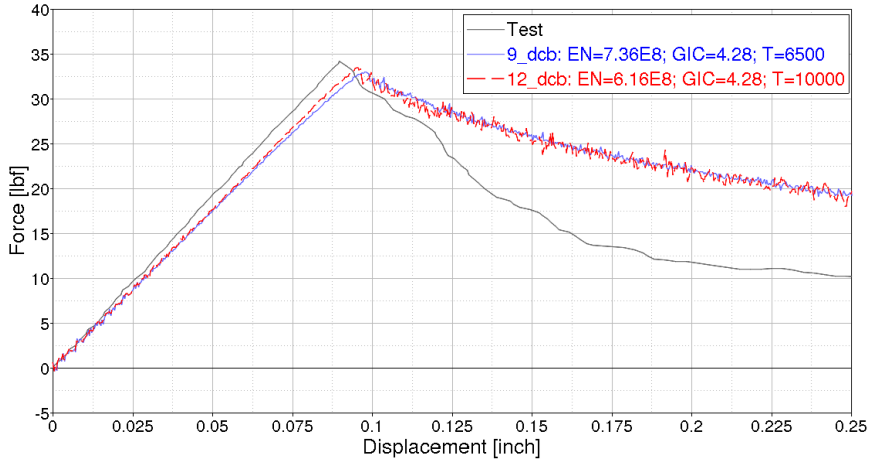

Figure 1.28. Effect of T on DCB results

The main parameter that influences the maximum force itself is the strain energy release rate (Mode I). As figure 1.29 shows, for a lower strain energy release rate, the crack starts to propagate at a lower force.

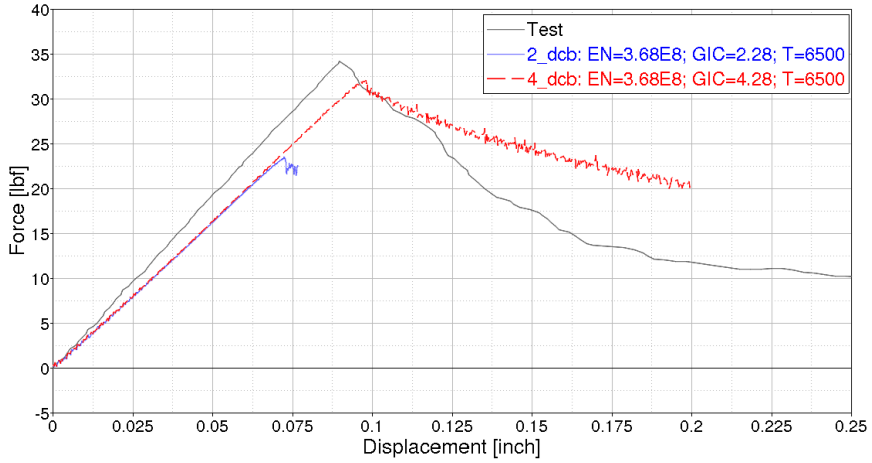

Figure 1.29. Effect of GIC on DCB results

Similar results can be obtained for the Mode II ENF test. The elastic stiffness in a plane has very little influence on the force versus displacement results of the ENF test (figure 1.30).

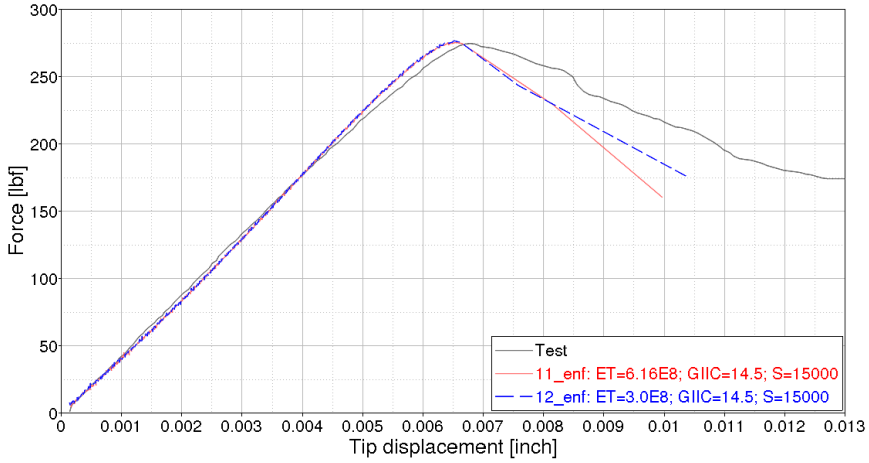

Figure 1.30. Effect of ET on ENF results

A decrease of the Interfacial strength (Mode II) decreases the slope of the force versus displacement curve (figure 1.31).

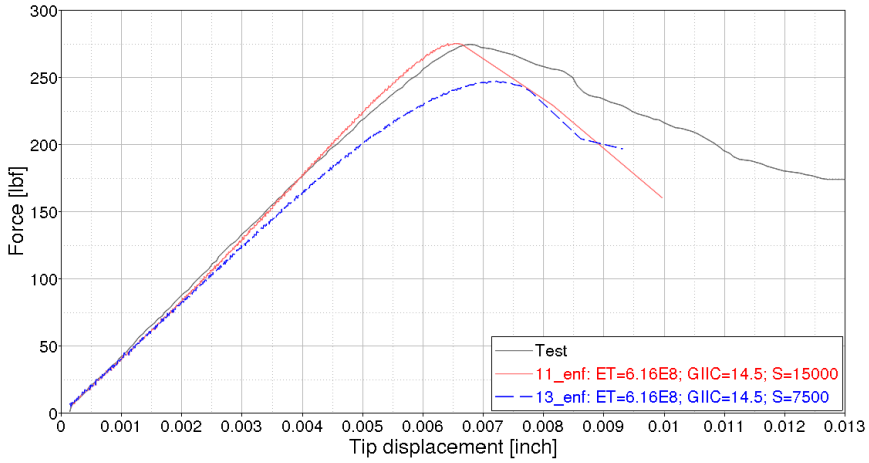

Figure 1.31. Effect of S on ENF results

A reduction of the strain energy release rate (Mode II) again reduces the maximum force that is reached before the crack propagates (figure 1.32).

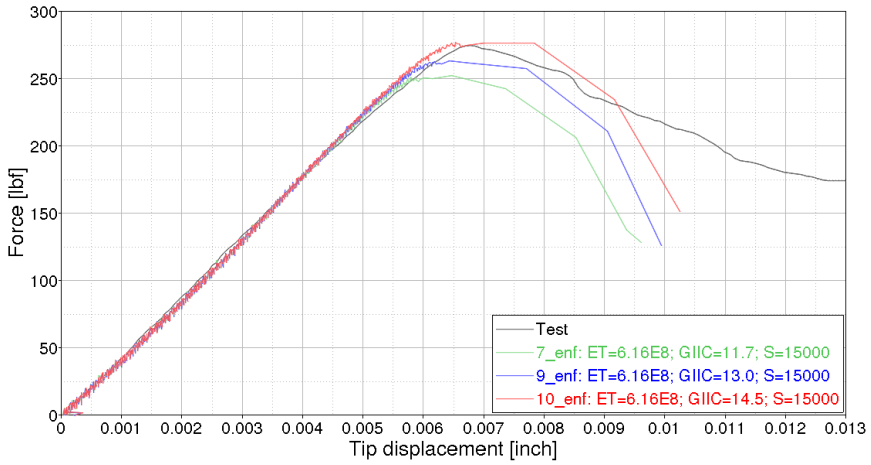

Figure 1.32. Effect of GIIC on ENF results

Validation

The delamination model developed above was validated by simulating the impact tests. Figure 1.33 shows the impact simulation setup. The simple boundary setup described in figure 1.14 was applied to the plate. The aluminum impactor was modeled with 8-noded hexahedral elements and using a piecewise linear plasticity model (*MAT_024). No damping parameters were used in the FE models. The plate was modeled using *MAT_213 with 4 elements through the thickness and an aspect ratio of 5.

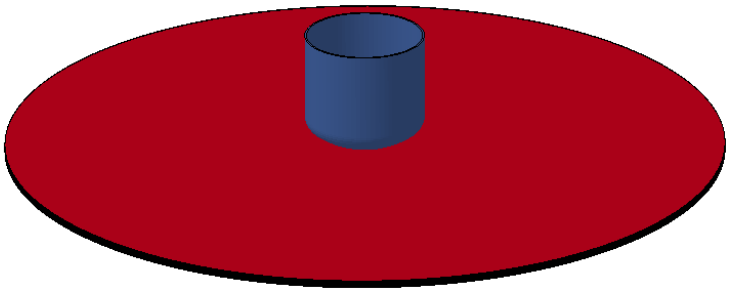

Figure 1.33. Impact simulation setup

First, the low-velocity impact test (LVG906), in which no delamination occurred, was considered. In figure 1.34, the Z-displacement over time for simulations of two models using cohesive elements and a tiebreak contact to model delamination is compared with the simulation result without the delamination model. For the relatively low-velocity of 27.4 ft/sec, one would assume that no delamination takes place and therefore the displacement versus time curve should be close to the same, which is the case.

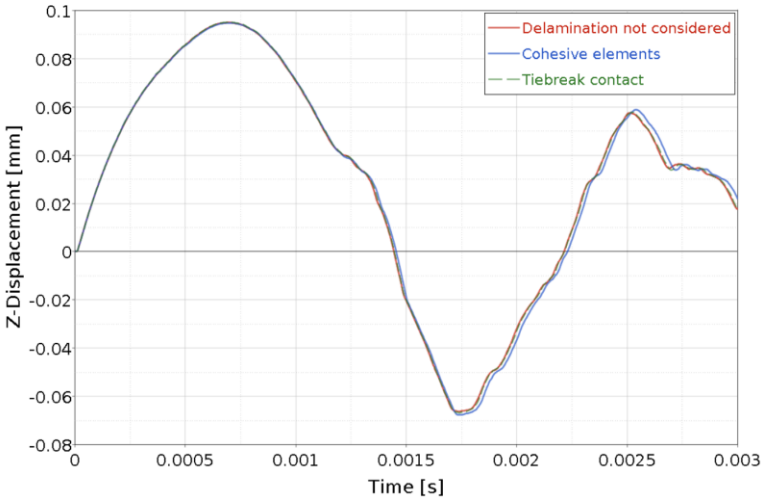

Figure 1.34. Impact simulation without delamination, cohesive elements and tiebreak contact

Next, the higher-velocity impact tests listed in table 1.9 were considered. In additional simulations, the velocity was increased to match some of the tested velocities. The ballistic impact test LVG903 at a velocity of 46 ft/sec lead to one visible crack in the post-test plate. In the simulation, however, no delamination occurred at the same speed. For a higher-velocity of about 145 ft/sec, the plate was damaged with three visible cracks in the physical test. The simulation at this speed showed delamination in the top layer (figure 1.35). The highest speed that was simulated was a velocity of 200 ft/sec for which no test was conducted. The simulation showed delamination in all three cohesive element layers (figure 1.36).

Table 1.9. Impact tests and simulations at different speeds

Test ID	Projectile Velocity (ft/sec)	Damage in Test	Delamination in Simulation
LVG 906	27.4	Contained no damage	No
-	36.5	-	No
LVG 903	46	Contained one crack	No
LVG 897	101.2	Contained one crack	-
LVG 898	~145	Contained three cracks	Yes (top layer)
-	200	-	Yes (all layers)
LVG 888	507.4	Penetrated	-

(a) (b) (c)

Figure 1.35. Delamination at 145 ft/sec projectile velocity; (a) top layer, (b) middle layer, and (c) bottom layer

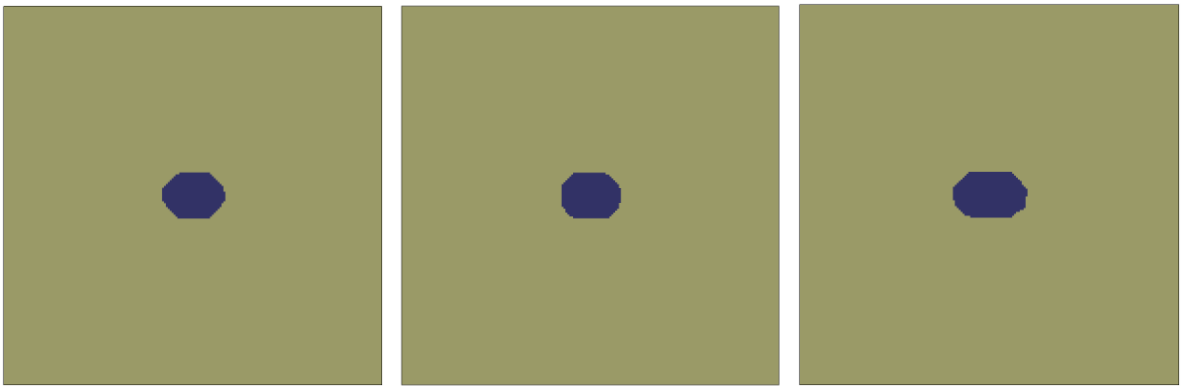

(a) (b) (c)

Figure 1.36. Delamination at 200 ft/sec projectile velocity; (a) top layer, (b) middle layer, and (c) bottom layer

In addition to the unidirectional panel simulations, the cohesive material was tested on cross-ply panels. The plate was modeled with 16 elements through the thickness with an aspect ratio of ~8 in the center of the plate. The mesh contained 370,000 8-noded hexahedral plate elements with one integration point and hourglass control type 1. Additionally, the interface between the plies was modeled with 350,000 cohesive elements to account for delamination.

Because the impact velocities were very similar, both test results of LVG1067 and LVG1071 were compared to the same simulation as shown in figure 1.37. The black line shows the z-displacement results of LVG1067 and the dashed black line of LVG1071. The displacement of the center point in the simulation is shown in blue and at the coordinates of the center in the test in red. The results of the simulation show a good agreement of the general shape of the test curve.

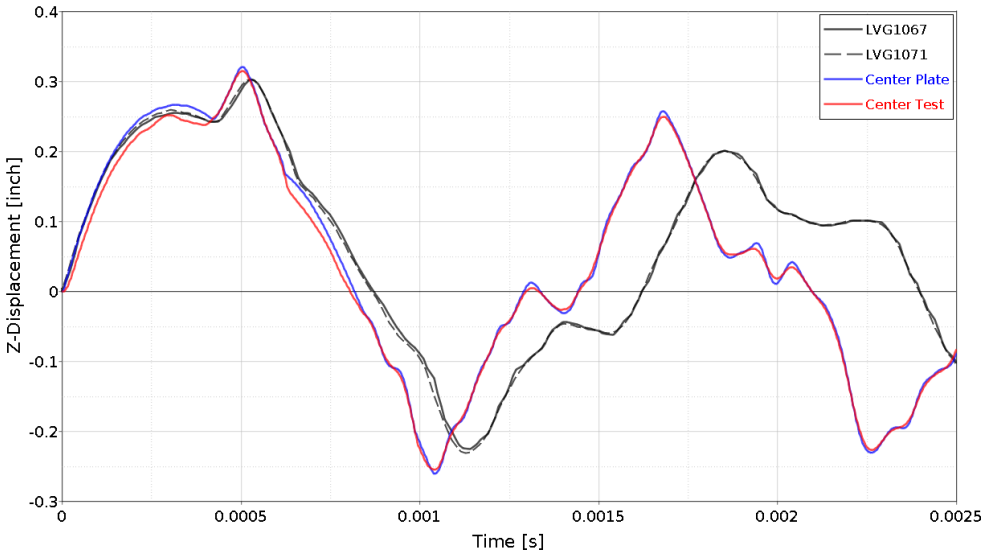

Figure 1.37. Displacement vs. time of test and simulation

In addition to the center, results at four more points of the plate were compared. Figure 1.38 shows the location of these points with point one, two and three lying perpendicular to the fiber direction in different distances from the center, and point four about two thirds to the edge of the plate in the fiber direction.

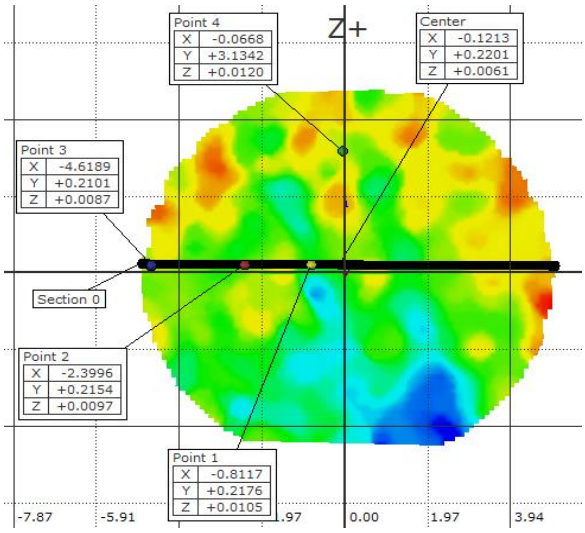

Figure 1.38. Measurement locations on plate

Figure 1.39 shows the displacement plots for these measurement points in the tests (black) and simulation (red), and a good agreement of the simulation results with the test.

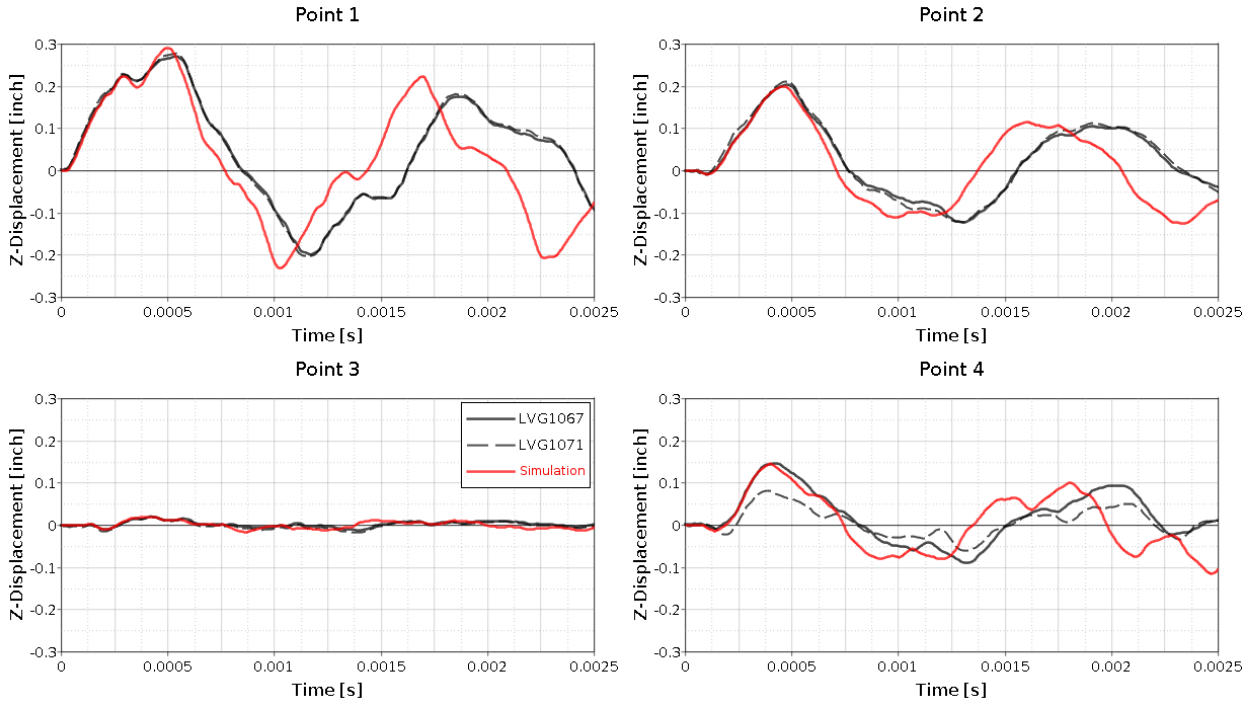

Figure 1.39. Displacement vs. time at several locations on plate

Since the interface between the composite plies was modeled with cohesive elements, apart from the displacement measurements, the delaminated areas in test and simulation can be compared. Using a method of Non-Destructive Evaluation (NDE), the test specimen was scanned to make delamination in the plate visible. These scans were then compared to the simulation by showing only the cohesive layers, coloring the cohesive elements that fail in the simulation, and changing the transparency of the model.

The NDE of the test specimen in LVG1067 is shown on the left in figure 1.40. A small area of delamination in a circular shape is visibly similar to the simulation results which are shown on the right. The differences in the shades of blue in the simulation are due to the different layers in which the delamination occurred. As there is no layer-by-layer examination of the delamination in the test specimen available, only the overall delaminated area is shown in the simulation.

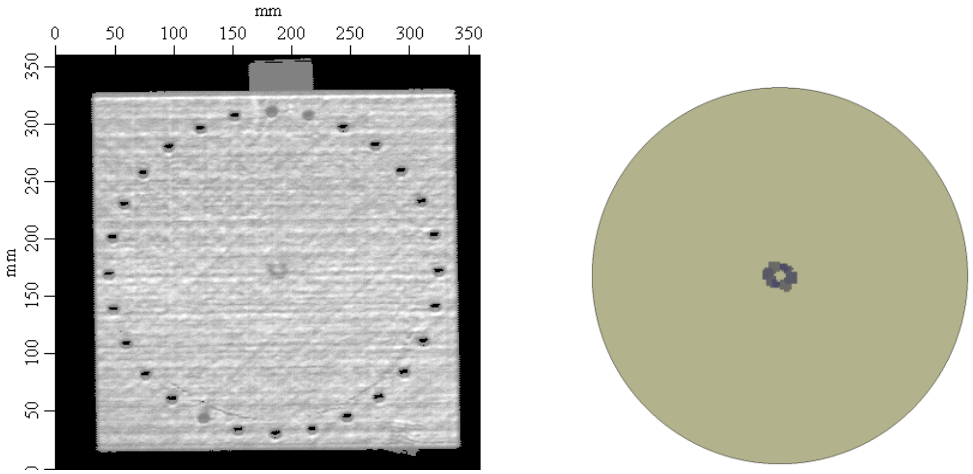

Figure 1.40. LVG1067: (a) NDE of test, and (b) delamination in simulation

Similar delamination results as for LVG1067 are obtained in LVG1071, which was conducted at almost the same velocity. Figure 1.41 shows the delaminated area in the test on the left and on the right the simulation results. In both test and simulation, a small circular area of delamination is visible.

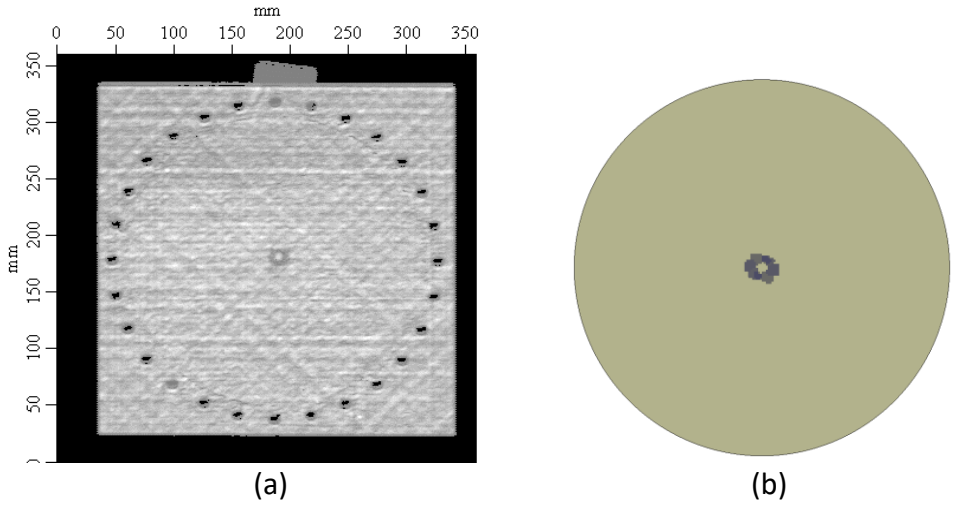

Figure 1.41. LVG1071: (a) NDE of test, and (b) delamination in simulation

In addition to LVG1067 and LVG1071, a lower velocity impact (LVG1065) was simulated as well. The black line in figure 1.42 shows the z-displacement results of LVG1065. The displacement of the center point in the simulation is shown in blue and at the coordinates of the center in the test in red. The results of the simulation show a good agreement of the general shape of the test curve.

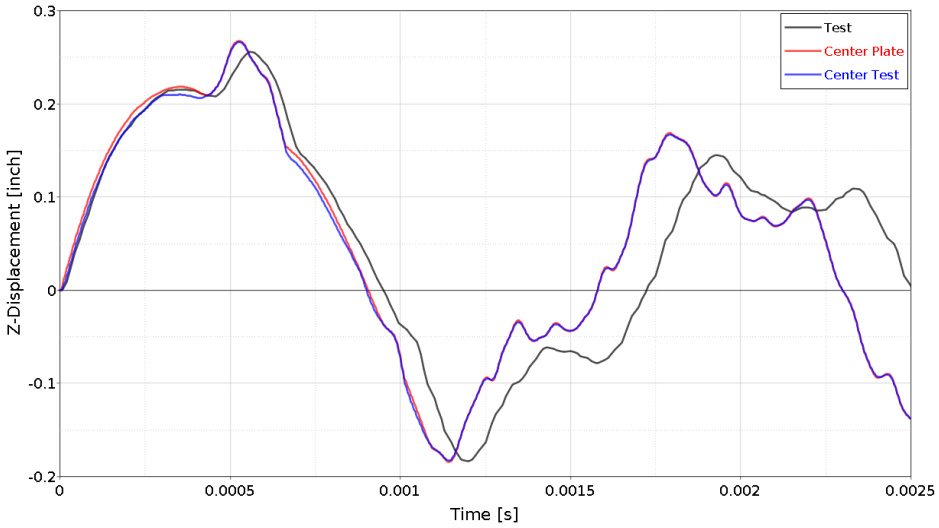

Figure 1.42. Displacement vs. time of test and simulation (LVG1065)

Figure 1.43 shows the displacement plots for the additional measurement points in the test (black) and simulation (red), and a good agreement of the simulation results with the test.

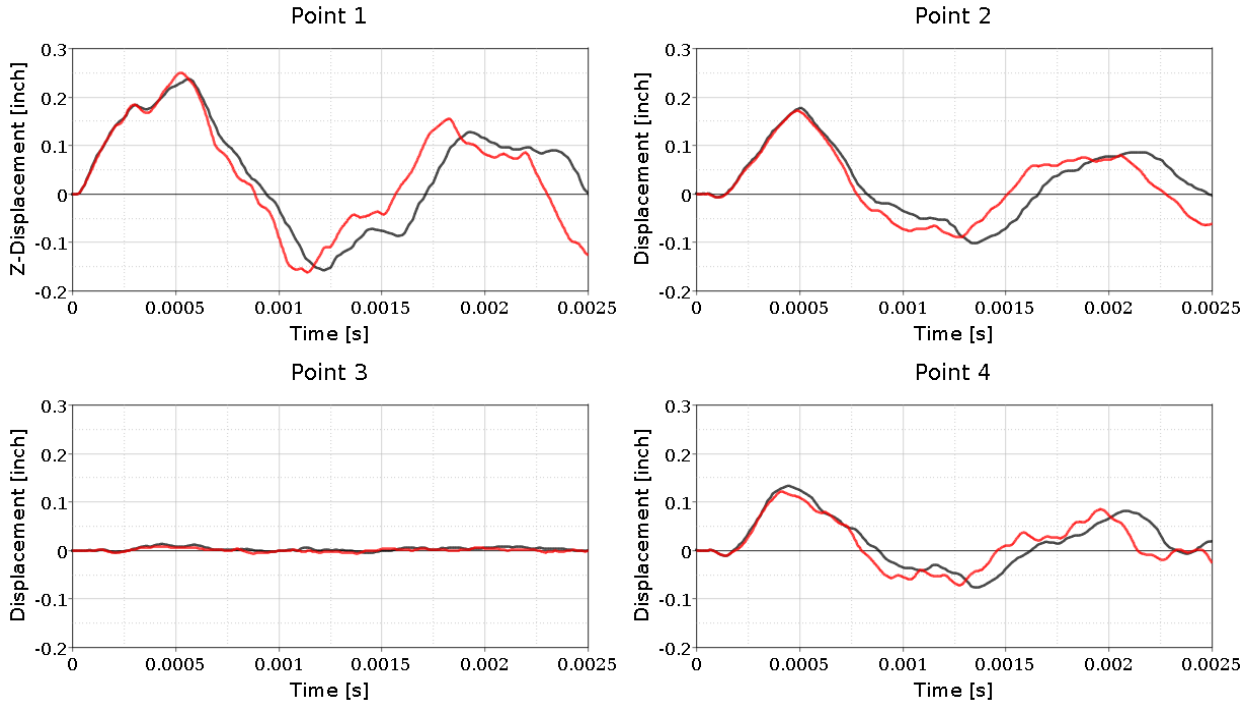

Figure 1.43. Displacement vs. time at several locations on plate (LVG1065)

Since the interface between the plies was modeled with cohesive elements, the simulated delaminated area was compared to the test. The NDE of the test specimen in LVG1065 is shown on the left in figure 1.44. In both test and simulation, no delamination occurred.

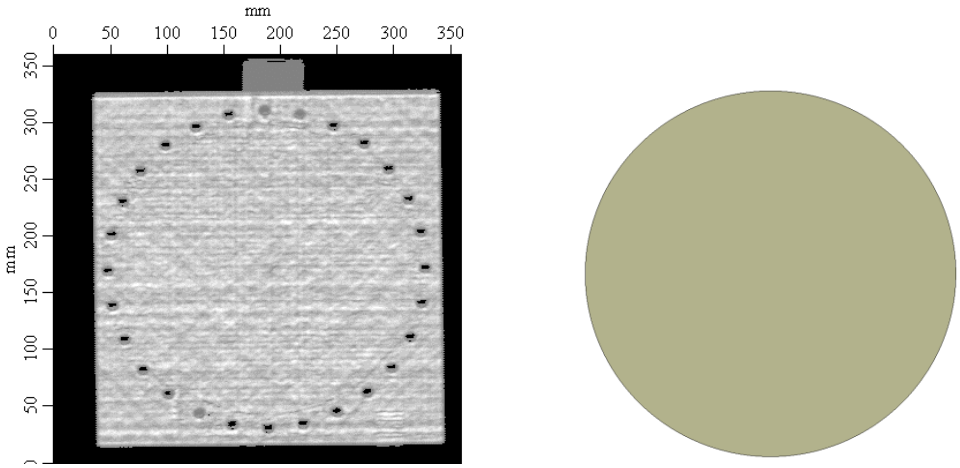

Figure 1.44. LVG1065: (a) NDE of test, and (b) delamination in simulation

1.5 IMPACT SIMULATION MODEL USING *MAT_054

Because the validation of the *MAT_213 material model was still ongoing at the time of this study, the widely used LS-DYNA material model *MAT_054 was used for developing the computational framework of stochastic analysis in Chapter 2. Therefore, the material model *MAT_054, in conjunction with a failure criterion available in *MAT_ADD_EROSION, was verified in single-element simulations and validated using ballistic impact tests and simulations. The goal was to create the required baseline material input to study the effects of statistical variation of material parameters on the response in ballistic impact simulations. This study can furthermore be helpful as a baseline comparison case to newly developed composite material models, as it describes a currently commonly used material model for ballistic impact simulations, the steps necessary to obtain useful results, and the limitations of the model.

**MAT_054 Material Model and Single-Element Verification*

Single-element simulations were used to verify that the baseline material card is working as expected, and to highlight some of the current capabilities of *MAT_054. Figure 1.45 shows the input to the *MAT_054 material card, while table 1.10 lists how these values were obtained and, if applicable, the source. The material tests to get the elastic properties of the T800/F3900 composite were performed by Arizona State University and The Ohio State University.

Apart from the elastic properties that were obtained using material tests (shaded blue), several material parameters had to be taken from the literature (shaded red). Obtaining good values for these parameters can be time and resource intensive and requires extensive calibration efforts to reverse engineer the correct values for the used material. Since many of these parameters were obtained for a different fiber/matrix combination, they might not be the best values possible and could be improved. Due to time constraints, an extensive calibration of these parameters was not performed in this study.

```
*MAT_ENHANCED_COMPOSITE_DAMAGE
$#     mid        ro        ea        eb      (ec)      prba    (prca)      prcb
         1 1.4521E-4   23.46E6   1.066E6                0.016800            0.4390
$#     gab       gbc       gca      (kf)     aopt      2way        ti
  0.5795E6   0.326E6                          2.000                 1
$#      xp        yp        zp        a1        a2        a3    mangle
                                         1         0         0
$#      v1        v2        v3        d1        d2        d3    dfailm    dfails
                                         1         1         0
$#   tfail      alph      soft      fbrt     ycfac    dfailt    dfailc       efs
                0.1                 0.5       1.2     300.0    -300.0
$#      xc        xt        yc        yt        sc      crit      beta
    105513    366070     25513      6502     18670        54       0.5
$#     pel      epsf      epsr      tsmd     soft2
$#  slimt1    slimc1    slimt2    slimc2     slims    ncyred     softg
    0.2834       1.0    0.6402       1.0       1.0
```

Figure 1.45. Material model using *MAT_054

Table 1.10. Material input parameters and source of value [1]

*MAT_054	Description	Source of value
ro	Mass density	Material test
ea	Young's modulus - longitudinal direction	Material test
eb	Young's modulus - transverse direction	Material test
prba	Poisson's ratio ba	Material test
prcb	Poisson's ratio cb	Material test
gab	Shear modulus ab	Material test
gbc	Shear modulus bc	Material test
ti	Flag to turn on transversal isotropic behavior	Assumption
alph	Shear stress parameter for nonlinear term	Assumption – as recommended by Wade et al. [12]
fbrt	Softening for fiber tensile strength	Assumption – as recommended by Wade et al. [12]
ycfac	Reduction factor for compressive fiber strength after matrix compressive failure	Assumption – as recommended by Wade et al. [12]
dfailt	Maximum strain for fiber tension	De facto deactivated
dfailc	Maximum strain for fiber compression	De facto deactivated
xc	Longitudinal compressive strength	Material test

*MAT_054	Description	Source of value
xt	Longitudinal tensile strength	Material test
yc	Transverse compressive strength	Material test
yt	Transverse tensile strength	Material test
sc	Shear strength, ab plane	Material test
crit	Failure criterion	Computational
beta	Weighting factor for shear term in tensile fiber mode	Assumption – as recommended by Wade et al. [12]
slimt1	Factor to determine the minimum stress limit after stress maximum (fiber tension)	Assumption – generally requires extensive calibration [13]
slimc1	Factor to determine the minimum stress limit after stress maximum (fiber compression)	Assumption – generally requires extensive calibration [13]
slimt2	Factor to determine the minimum stress limit after stress maximum	Assumption – generally requires extensive calibration [13]
slimc2	Factor to determine the minimum stress limit after stress maximum (matrix compression)	Assumption – generally requires extensive calibration [13]
slims	Factor to determine the minimum stress limit after stress maximum (shear)	Assumption – generally requires extensive calibration [13]

To verify that the material is responding as expected, single-element simulations were performed. The material was loaded in 1-, 2-, and 3-directions in tension and compression as well as in 12-, 23-, and 31-shear. Figure 1.46 shows the results of the 9 single-element simulations.

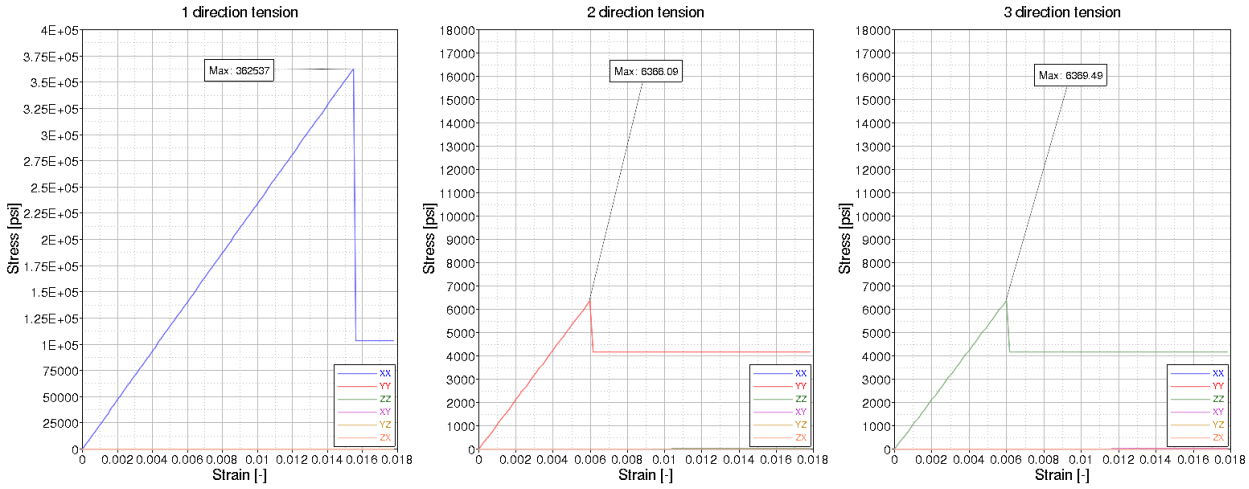

(a)

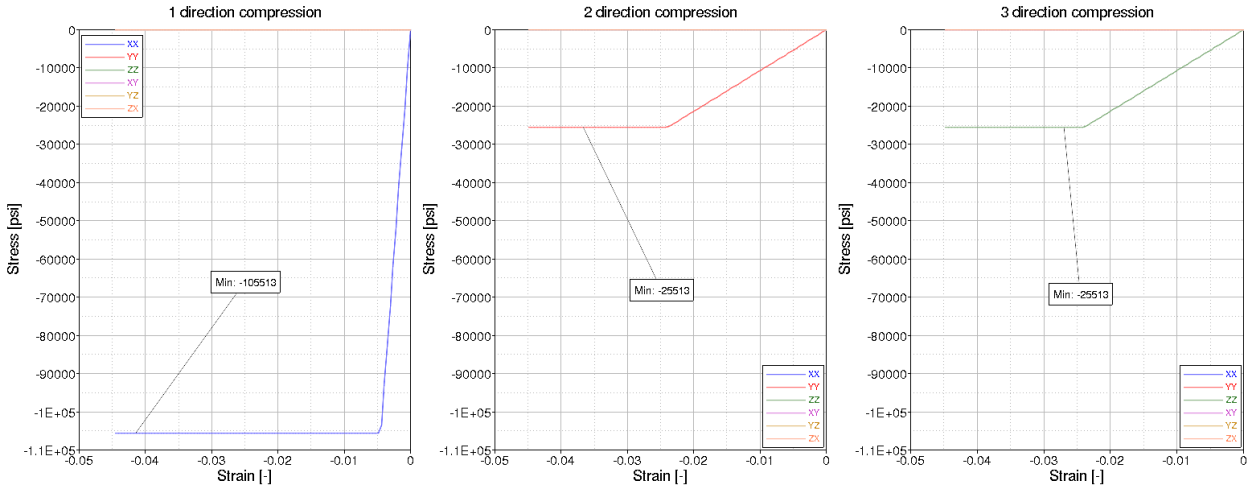

(b)

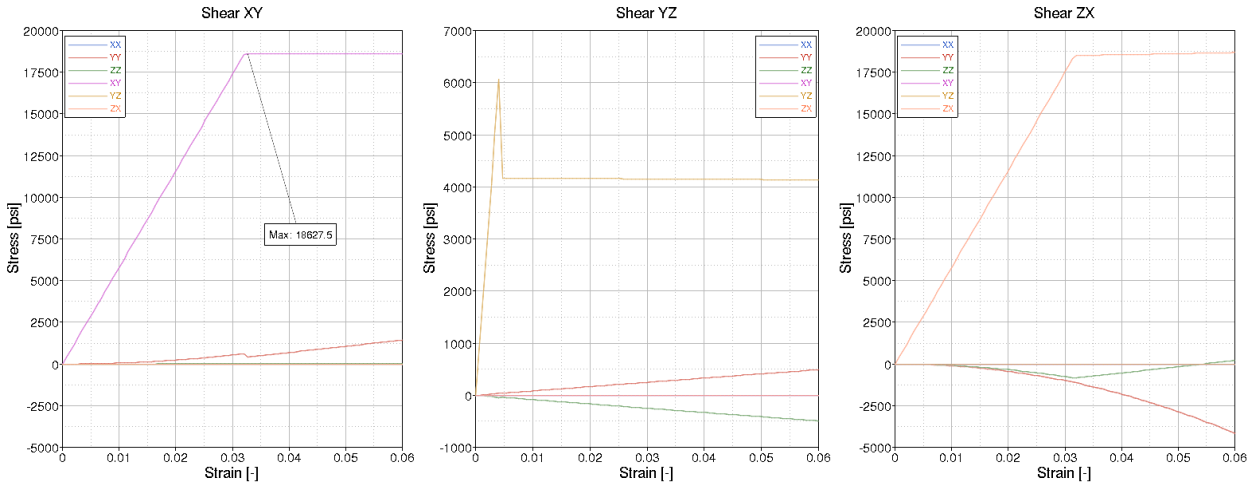

(c)

Figure 1.46. Stress vs. strain results of single-element simulations: (a) tension, (b) compression, and (c) shear

In 1-direction tension, the material responds linear elastically until the longitudinal tensile strength (XT) is reached. The stress then drops to XT*SLIMT1 and stays perfectly plastic. As the transverse isotropic behavior flag is turned on (TI=1), the response in the 2- and 3-direction is expected to be the same, which is the case. This option was made available starting with LS-DYNA revision 10.0 in June 2017.
In both the 2- and 3-direction tension, the stress increases linear elastically until the transverse tensile strength (YT) is reached and then drops to a perfectly plastic level of YT*SLIMT2.

In compression, the SLIM values were chosen to be 1 (assumption) and therefore, after the compressive strengths (XC and YC) are reached, the stress does not drop but stays perfectly plastic at the level of XC and YC respectively. The response in shear 12- and 31-directions are the same due to transverse isotropy with stresses reaching SC and then staying perfectly plastic at that level due to SLIMS being chosen as 1.

In shear 23, the material seems to respond similarly to tension in the transverse direction with stresses reaching a level of YT and then dropping to YT*SLIMT2.

*Validation of *MAT_054 Material Model using Impact Simulations*

In the ballistic impact tests, a projectile hits a 16-ply composite plate with a layup of $[0, 90, +45, -45]_{2S}$. In the simulation, the plate was constrained in impact direction in the area of the clamping and in plane where the bolts are located in the test as shown in figure 1.14. The plate was modeled with 16 elements through the thickness using 370,000 solid elements and additionally 350,000 cohesive elements to account for delamination between the layers.

For validation of the elastic response of the material, a relatively low-velocity impact (LVG1067/1071 – 155.0 ft/sec) was chosen. To calibrate the failure criterion, three high-velocity impacts were chosen:

- LVG1075 – 385.0 ft/sec, in which the projectile caused significant damage to the plate but was contained.
- LVG1074 – 417.0 ft/sec, where the projectile penetrated the plate and exited with a low-velocity (~25 ft/s).
- LVG1076 – 454.0 ft/sec, which was the second highest velocity tested by NASA, where the projectile penetrated the plate and exited with a high-velocity.

Figure 1.47 shows a plot of impact velocity (abscissa) vs. exit velocity (ordinate) in the penetration cases, or rebound velocity (ordinate) in the cases where the projectile was contained.

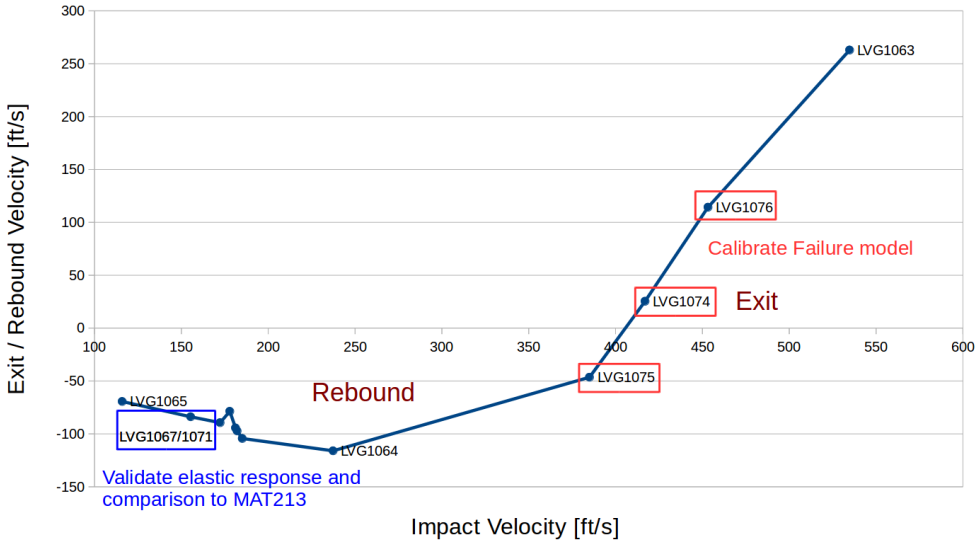

Figure 1.47. Projectile velocities pre- and post-impact

The elastic response of the material model was validated using the low-velocity impact tests LVG1067 and LVG1071, with projectile velocities of 155.0 and 155.38 ft/sec, respectively. The impact caused no visible damage to the plate in both tests. Figure 1.48 shows the displacement in impact direction in the center of the back side of the plate in the test (blue), simulated using *MAT_022 (purple), an early version of *MAT_213 and the material card *MAT_054 described earlier in this document. The response of *MAT_054 was considered “close enough” to the test results and therefore could be used in the higher-velocity impacts to calibrate a failure model.

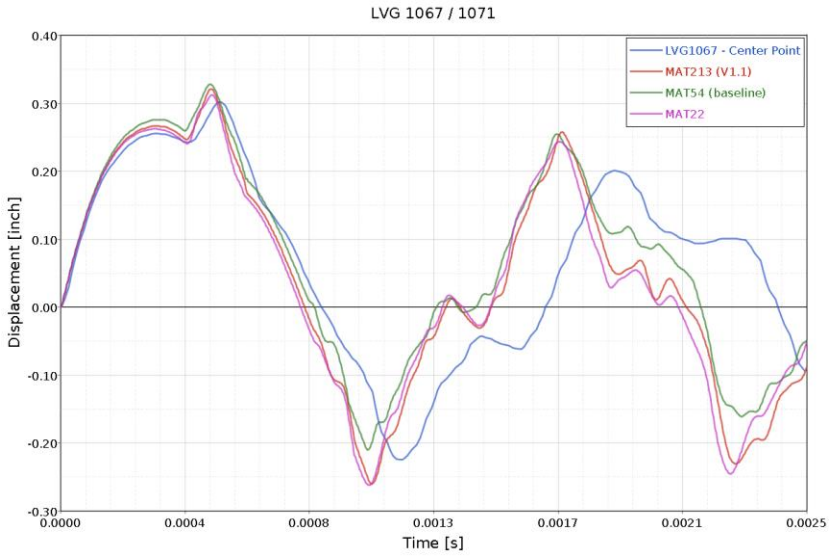

Figure 1.48. Plate Z-displacement vs. time

For this study, failure was considered using the LS-DYNA *MAT_ADD_EROSION card, which provides an option to include different failure criteria with existing material models. The options chosen were minimum and maximum principal strain at failure and tensorial shear strain at failure. To calibrate this failure model, three higher-velocity impacts were simulated.

As a first step, the lowest of the three velocities was simulated with failure disabled. Plotting the minimum and maximum principal strain at failure and the shear strain in this simulation provided a starting point to identify failure parameters that allow for an accurate modeling of the failure patterns. By trial and error, approximately 10 different combinations of the three failure parameters were simulated at the three different impact velocities. The total amount of simulations to come up with the final set of values was therefore around 30 simulations.

The projectile velocities pre- and post-impact are plotted in figure 1.49, with the horizontal datum lines representing the exit velocity that was measured in the test. A good fit of the simulation is therefore obtained if the post-impact velocity of the projectile is close to the datum line of the specific test. As figure 1.49 shows, the material is capable of modeling the projectile rebound in LVG1075 and the penetration and exit velocities in LVG1074 and LVG1076.

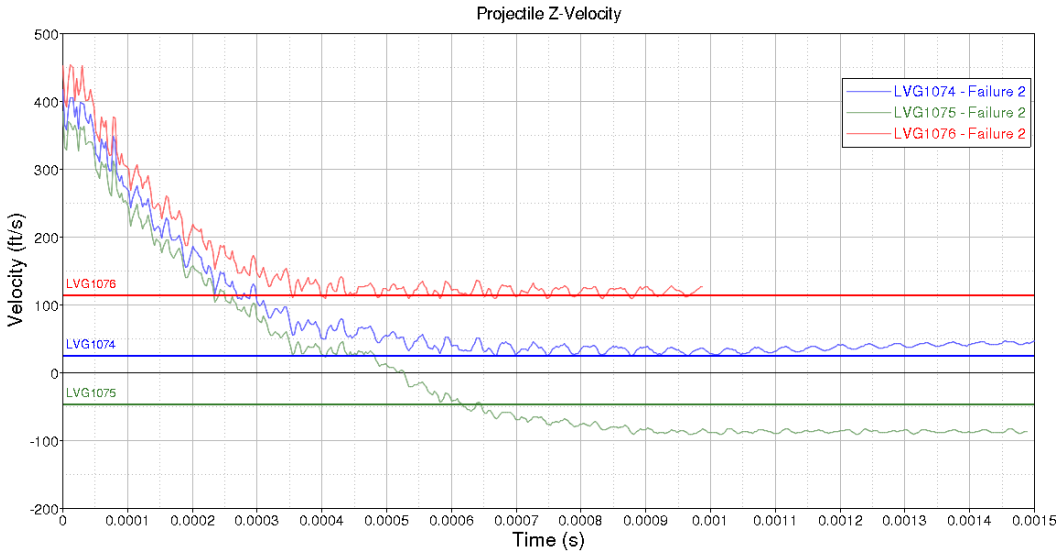

Figure 1.49. High-velocity impact simulations - projectile velocity pre- and post-impact

The failure pattern in the test and the simulation are shown in figure 1.50. In both test and simulation, the plate fails in a cross-like pattern with significant delamination between the layers. The failure patterns in the higher speed impacts looked similar in the tests and simulations.

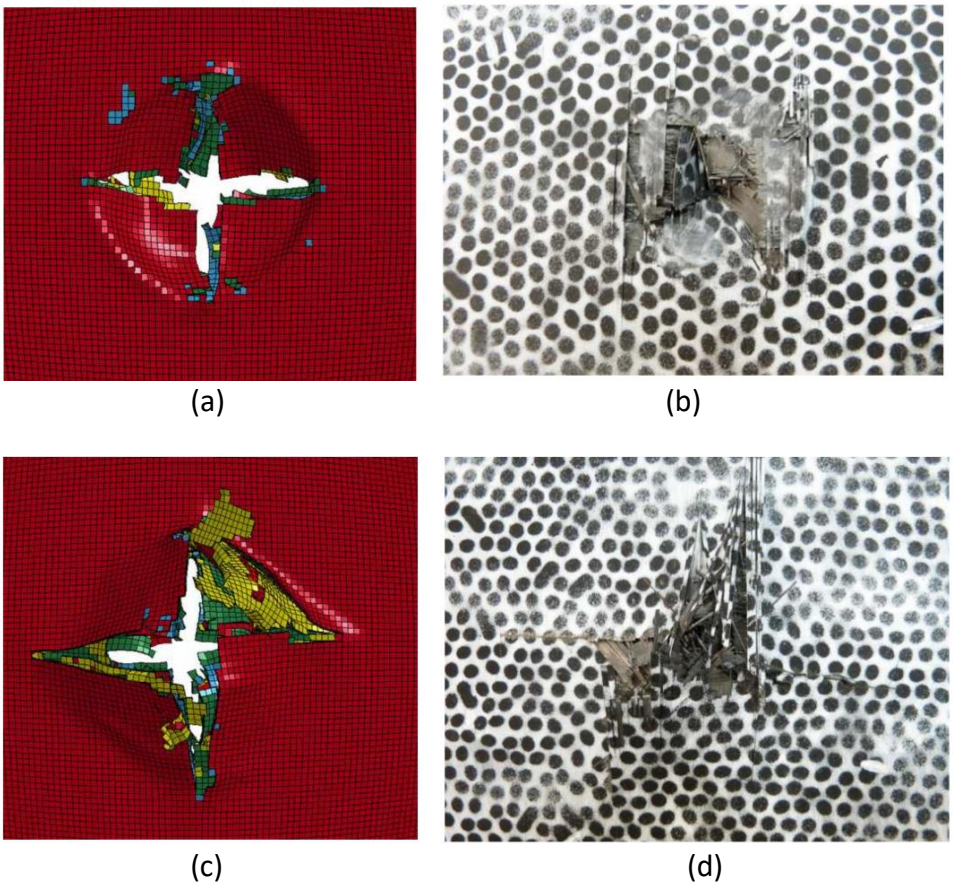

Figure 1.50. LVG1075 – post impact: (a) top view in simulation, (b) top view in test, (c) bottom view in simulation, and (d) bottom view in test.

As mentioned earlier, delamination was accounted for by the use of cohesive elements that were calibrated extensively in an earlier study based on Double Cantilever Beam, End Notched Flexure tests, and ballistic impact simulations. However, this was the first time the calibrated cohesive material was used in high-velocity impacts. As the images in figures 1.51 to 1.53 show, the predicted delaminated areas in the simulations (left) are close to the delaminated areas that can be seen in scans of the tested specimen (right).

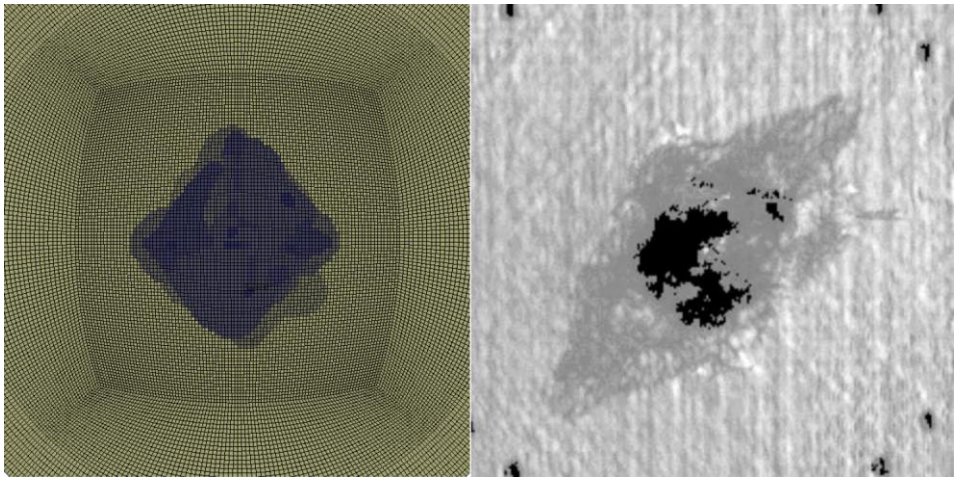

(a) (b)

Figure 1.51. LVG1075 – delamination: (a) simulation, and (b) test

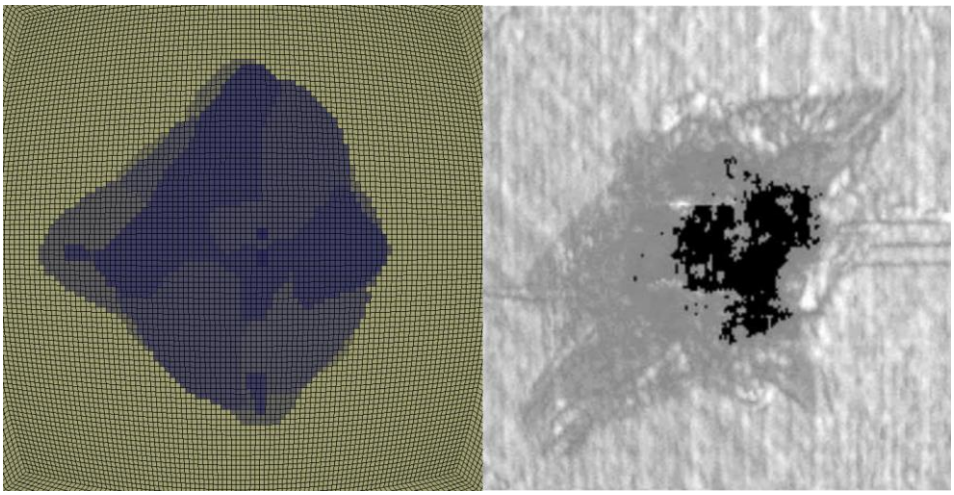

(a) (b)

Figure 1.52. LVG1074 – delamination: (a) simulation, and (b) test

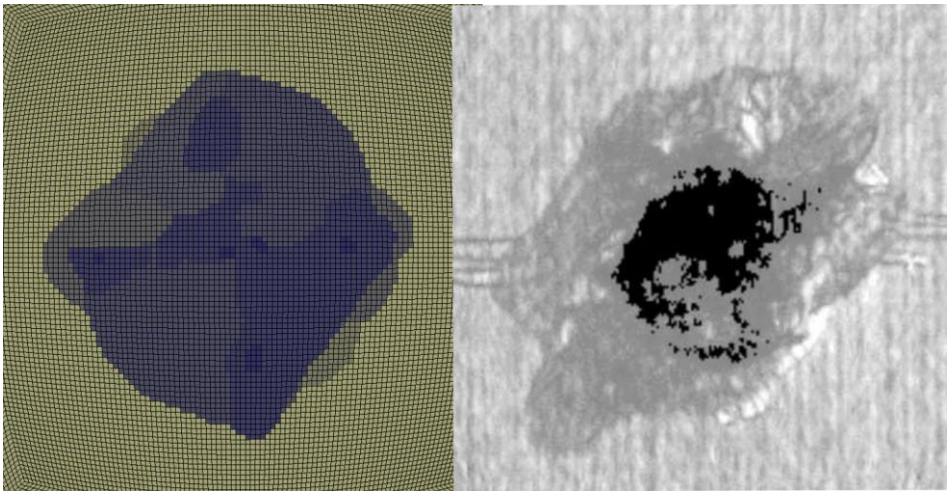

(a) (b)

Figure 1.53. LVG1076 - delamination: (a) simulation, and (b) test

The importance of accounting for delamination in ballistic impact simulations of composite plates is demonstrated by comparing a simulation without cohesive elements to the baseline simulation. Figure 1.54 shows the projectile velocity in the LVG1074 case. Just like in the test, the projectile penetrated the panel in the simulation in which delamination was accounted for by cohesive elements (blue). In the simulation without cohesive elements (red), the projectile is contained and rebounds the plate (negative post-impact velocity). This highlights the need to account for delamination in impact simulations of composites.

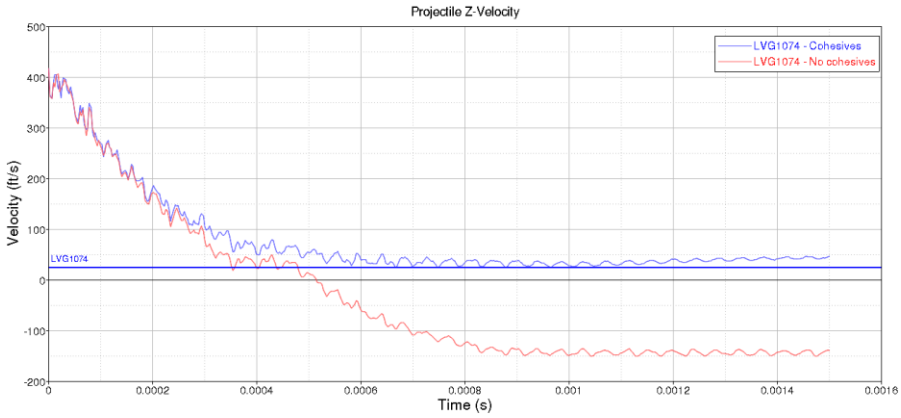

Figure 1.54. Projectile velocity in LVG1074 simulation with and without cohesive elements

Assumptions and Limitations

Due to the limited scope of this study, some assumptions were made to simplify the analysis. As mentioned earlier, several material parameters were taken from the literature, where these values were optimized for different fiber/matrix pairings. In addition, the material and failure models were calibrated on a specific use case with a certain mesh size and orientation. Variations in loading, for example, due to a different projectile shape or a different mesh size and/or orientation, might need additional or new calibration efforts.

This strong mesh dependency can be shown by rotating the plate by 45° or by using a finer mesh size. Figure 1.55 shows the projectile velocity results for the baseline mesh (solid lines) and for the rotated mesh (dashed lines). As the material direction was defined in the global coordinate system, this does not influence the results, and the difference between the original (0°) and the rotated (45°) mesh can only be explained by the mesh sensitivity. The simulation of LVG1074 (blue) in figure 1.55 with the original mesh, previously correctly predicting penetration of the projectile with a low exit velocity, now predicts a rebound of the projectile when the rotated mesh is used. The pattern of failure also shows differences between the baseline and the rotated mesh (figures 1.56) with the pattern roughly following the element lines in both cases.

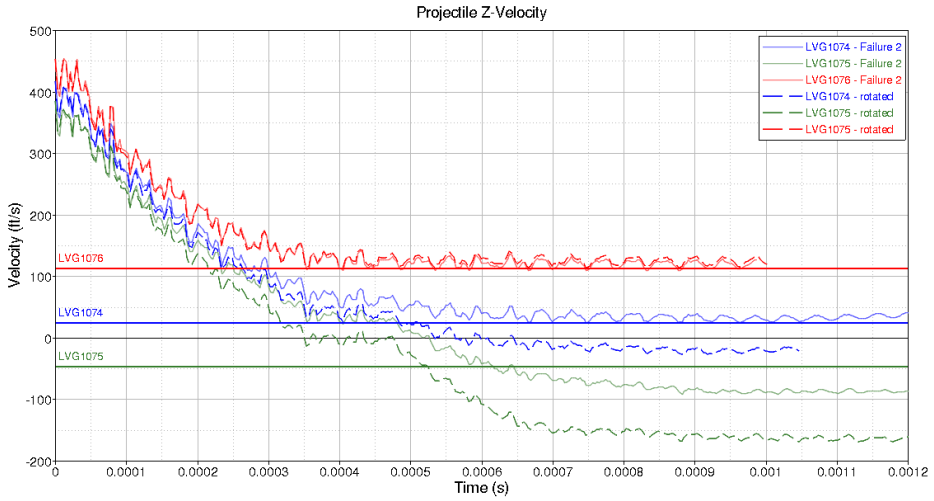

Figure 1.55. Projectile velocities with baseline mesh and with 45° rotated mesh

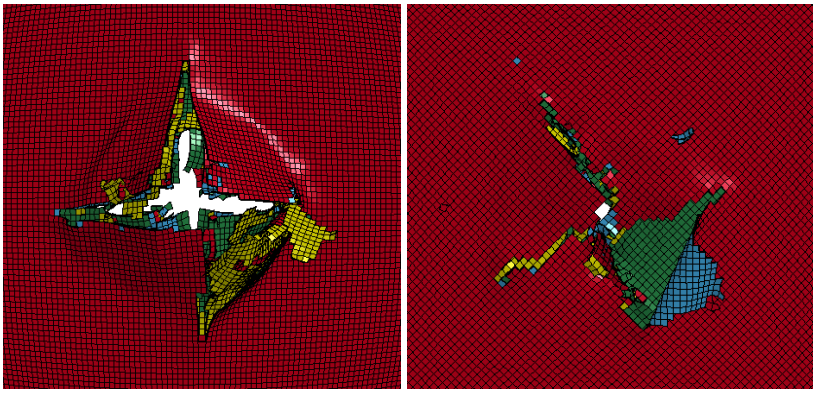

(a) (b)

(b)

Figure 1.56. LVG1074 - delamination: (a) original mesh, and (b) 45° rotated mesh

In addition to the rotated mesh, the results of the original mesh were compared to a fine mesh size of approximately half the element size of the baseline. In this case, the projectile velocities change in a different way, with all three simulations now resulting in penetration with high exit velocities, as shown in figure 1.57. The failure pattern of the plate changes is shown in figure 1.58.

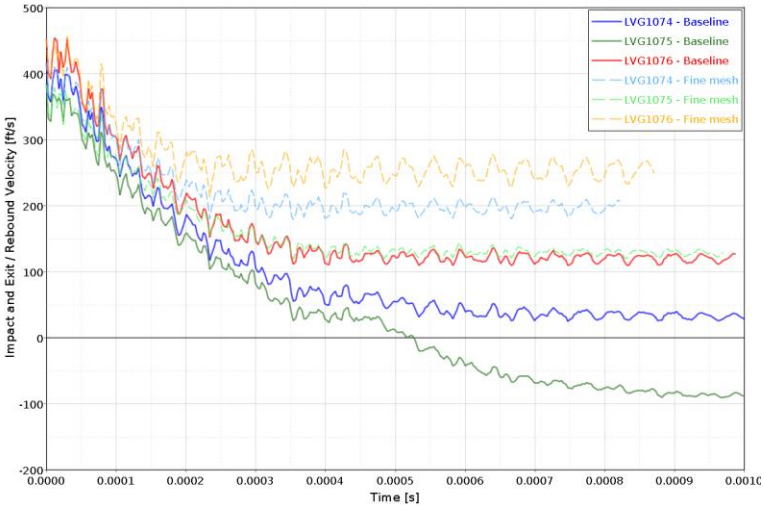

Figure 1.57. Projectile velocities with original mesh and with fine mesh

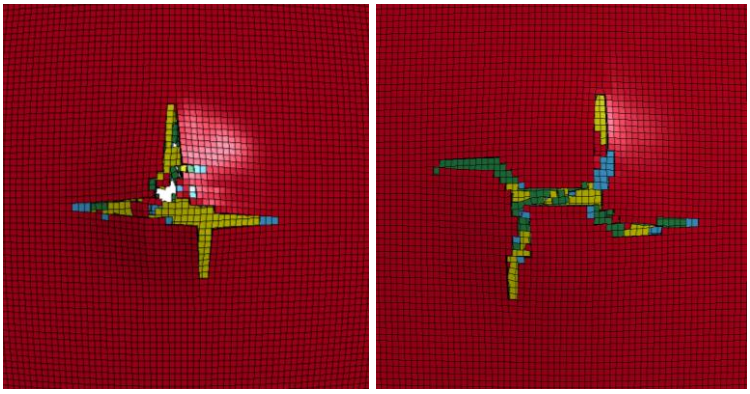

(a) (b)

Figure 1.58. LVG1074 - delamination: (a) original mesh, and (b) fine mesh – zoomed

2. STOCHASTIC COMPUTATIONAL FRAMEWORK OF MULTISCALE COMPOSITE ANALYSIS

The parameters of any mechanical or structural system possess a random variation as a function of space and time. The randomness in fracture parameters is related to uncertainties involved in the design and manufacturing stages, as well as the uncertain nature of the operating conditions. At the design stage, randomness is present in the test data regarding material strength values, elastic constants, engineering constants, damage parameters, and the material properties pertinent to the service life. The randomness of material properties significantly affects the functioning of the mechanical component and is unavoidable even with the best quality control measurements. Especially in structures like impact resistant components, where failure initiation is a locally driven event, the influence of randomness in material properties is no more negligible when the goal is to obtain the most accurate results possible. In order to account for these statistical variations in microscale properties of the material, a new numerical approach, different from the actual deterministic one, is required.

Due to the diminishing effect of microscale randomness at higher length scales, microstructural variability is often ignored. However, in some type of structures under particular concentrated loading conditions such as in impact resistant structures, the local properties are highly dominant for the failure generation. As experimental data of impact simulations show for a precise impact velocity on a chosen component, it is possible to define the probability of penetration. For this reason, especially in composite materials, due to their complex microscale nature, studies on the influence of stochastic variations of their properties are becoming more and more common.

The numerical investigation of the effects of microscale characteristics variability has to be supported by an efficient computational framework. A direct introduction of microscale-level modeling into classic FEM analysis, most of the time, can be computationally too expensive, especially in impact analysis. In literature, the most common procedure is the development of multiscale analysis that allows introducing a microscale level modeling without increasing sensibly the computational cost of the simulation.

Considering impact resistant structures, Johnston et al. [14] developed a stochastic computational framework with scale-dependent constitutive laws and an appropriate failure theory to simulate the behavior and failure of polymer matrix composite structures subjected to complex loading, showing the influence of variations in properties such as fiber volume fraction, fiber dimensions, fiber waviness, pure resin pockets, and void distributions to the composite impact performance.

Nilakantan et al. [15] have also performed a research about the prediction of the impact performance of flexible textile composite using multiscale and probabilistic methods. Here a yarn model comprised of a ~~lament~~laminate level architecture is developed to investigate the feasibility of solid element based homogenized yarn models as well as

the effect of ~~lament~~laminate strength, spreading, and inter~~n~~-~~lament~~laminate friction on the impact response and the numerical determination of the probabilistic velocity response curve.

Ricks et al. [16] have developed a multiscale modeling methodology that incorporates a statistical distribution of fiber strength into coupled micromechanics/finite element analysis. Here has been investigated the effect of a statistical fiber strength distribution and microscale architecture on the failure behavior of a dogbone specimen of SCS-6/TIMETAL 21S material.

Goldberg and Bonacuse [17] investigated the effects of the microstructural variations of woven ceramic matrix composites on the effective properties and response of the material, and Arnold et al. [18] studied the microstructural influence on deformation and fatigue life of composites.

In this work, the stochastic computational framework of the multiscale composite analysis was developed for a ballistic impact simulation. First, the stochastic microscale analysis of a composite was conducted to estimate probability distributions of composite properties. Then, the output of the microscale analysis was introduced into the macroscale model. Lastly, the stochastic macroscale analysis of an impact simulation was conducted to identify the probability ballistic velocity response of a composite plate.

2.1 STOCHASTIC MICROSCALE ANALYSIS

For the microscale analysis, the Micromechanics Analysis Code with the Generalized Method of Cells (MAC/GMC) [19] developed by NASA was utilized. Basically, the MAC/GMC allows performing simulations to compute composite material properties starting from its constituent's characteristics.

The GMC is capable of predicting the response of both continuous and discontinuous multi-phase composites with arbitrary internal microstructures and reinforcement shapes. The GMC is a continuum-based micromechanics model that provides closed-form expressions for the macroscopic composite response in terms of properties, size, shape, distribution, and response of the individual constituents or phases that make up the material. Furthermore, expressions relating the internal stress and strain fields in the individual constituents in term of the macroscopically applied stresses and strains are available through strain or stress concentration factors. These expressions make the investigation of failure processes at the microscopic level possible at each step of an applied load history.

In the MAC/GMC, a continuously or discontinuously reinforced, unidirectional fibrous composite was modeled as a rectangular double periodic (or triple periodic) array of fibers embedded in a matrix phase. The periodic character of the assemblage allowed identification of a Repeating Unit Cell (RUC) that can be used as a building block to construct the entire composite. The material structure of the unidirectional T800/F3900

considered in this study makes the doubly-periodic GMC the most suitable and efficient micromechanics model.

By assigning the different constituent materials to the sub-cells within the RUC, these elements are organized to represent the composite material structure. As the name indicates, the RUC repeats infinitely in two Cartesian coordinate directions as shown in figure 2.1. The doubly periodic GMC is infinitely long in the third out-of-plane X_1 direction and represents an infinite heterogeneous (composite) medium with a periodic microstructure. Thus, the GMC may be thought of as a model for a material point that may be the representative part of a larger overall structure. This micromechanics model not only computes the effective properties of the composite material located at a particular material point but also allows the simulation of applied loading conditions (in the form of global stresses, global strains, and a uniform temperature change) on the composite material to perform failure analysis for different loading histories and directions.

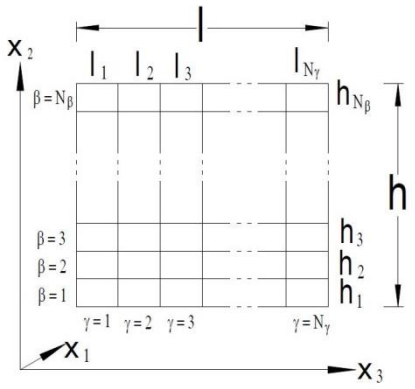

Figure 2.1. Characteristic parameters of RUC

The simplest architecture of an RUC for a composite material is a single-fiber RUC. This element is composed by a single-fiber surrounded by the matrix and can be represented with different levels of discretization. The internal library of the MAC/GMC contains different architectures of a single-fiber RUC. Figure 2.2 represents the internal MAC/GMC database single-fiber RUCs with a different number of sub-cells. The simplest architecture, shown in figure 2.2(a), is obtained using only four sub-cells, and the RUC architecture ID (ARCHID) 13 shown in figure 2.2(d) uses 676 sub-cells. In figure 2.2, the fiber sub-cell and the matrix sub-cell are represented in blue and in green, respectively.

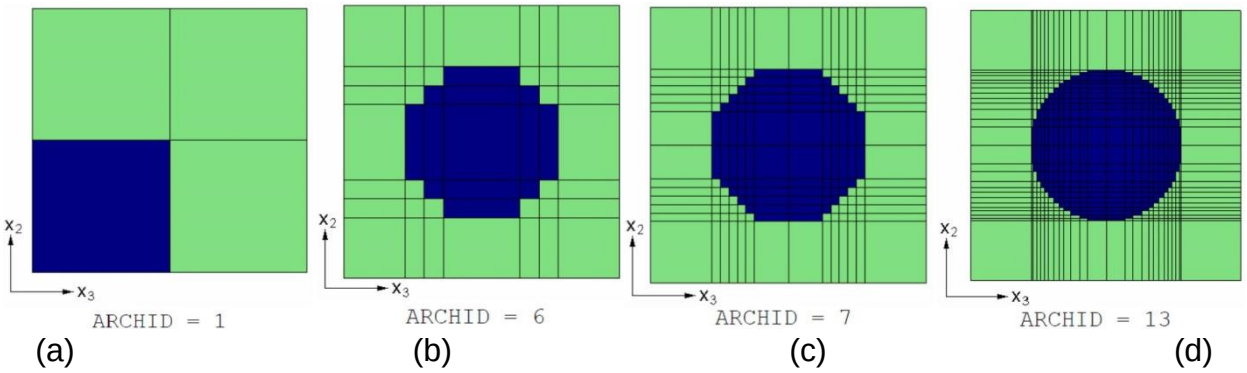

Figure 2.2. RUC architecture type: (a) ARCHID=1, (b) ARCHID=6, (c) ARCHID=7, and (d) ARCHID=13.

A second option to create an RUC is using ARCHID=99. Using ARCHID=99, the user can define an arbitrary structure for the RUC, and this option is able to create RUCs containing multiple fibers and user-defined fiber dispositions. These options, both single-fiber and multi-fiber, were used to study the microscale properties of the material and their probability distribution functions. After identifying mean values of the composite, it is necessary to evaluate the most accurate single-fiber RUC before comparing Monte Carlo simulation results of 1, 4, 16, and 26 fiber RUCs. Figure 2.3 shows the 25 fiber RUCs using ARCHID=99. The fiber sub-cell and the matrix sub-cell are represented in red and in blue, respectively.

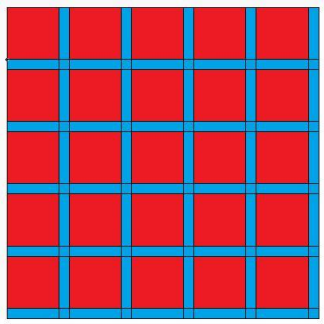

Figure 2.3. Example of RUC ARCHID=99 (25 fiber RUCs)

2.1.1 Properties of Composite Constituents

In the MAC/GMC, the carbon fiber T800 is modeled as transversely isotropic elastic and the epoxy matrix as linear elastic. To compute engineering moduli of the composite starting from these two constituents, six inputs for every material are required, plus the value of fiber volume fraction, which is summarized in table 2.1. For every one of these properties it is also necessary to evaluate the standard deviation (StD) and the distribution type. From literature, it has been possible to find information related to the distribution type and standard deviation for fiber properties and fiber volume fraction, but

data were rarely available on possible probabilistic distributions for matrix properties. Elastic properties are modeled with Gaussian distributions with a standard deviation of 5.87% for fibers and an arbitrary value, similar to the one used for the fibers, of 5% for the matrix.

Table 2.1. Constituent properties of MAC/GMC

	Fiber			Matrix		
		Mean	StD		Mean	StD
Axial Young modulus (GPa)	Ea_f	284.895	16.723	Ea_m	3.477	0.172
Transverse Young modulus (GPa)	Et_f	15.513	0.911	Et_m	3.477	0.172
Axial shear modulus (GPa)	Ga_f	103.420	6.071	Ga_m	1.275	0.064
Axial Poisson ratio	PRa_f	0.305	0.018	PRa_m	0.305	0.018
Transverse Poisson ratio	PRt_f	0.350	0.021	PRt_m	0.305	0.018
	Composite					
Fiber volume fraction (%)	V_f	54.0	3.381			

The same process of identifying means and standard deviations has to be applied to failure properties. Using literature, it has been possible to extrapolate means and the typical distribution to describe failure in a Weibull distribution type. Experimental tests show that failure in case of ballistic impact on T800/F3900 is driven by the ultimate strain of the epoxy matrix. Due to the high localized energy during impact, the resin exceeds the glass transition temperature becoming viscous and increasing its ultimate failure strain to almost 40%. Because of this behavior, to study the failure of the RUC only a strain-based failure criterion has been used in MAC/GMC — introducing a stress-based failure criterion has been identified as too conservative. Both for fiber and matrix, only six ultimate strain components are required, as shown in tables 2.2 and 2.3. The shape of the Weibull distribution function is defined by two parameters, such as a scale and a shape factor, which are determined in order to respect the desired standard deviation obtained from literature and to be close to literature shape factors. In the case of matrix properties, the same arbitrary standard deviation of 5% is maintained.

Table 2.2. Fiber failure properties of MAC/GMC

			Mean	StD	Shape factor	Scale factor
Ultimate axial strain	Direction 11	ε_{11}	0.01900	0.002958	7.60	0.02023
	Direction 22	ε_{22}	0.01900	0.002958	7.60	0.02023
	Direction 33	ε_{33}	0.01900	0.002958	7.60	0.02023
Ultimate shear strain	Direction 23	γ_{23}	0.01222	0.001868	7.75	0.01300
	Direction 13	γ_{13}	0.01222	0.001868	7.75	0.01300
	Direction 32	γ_{32}	0.01222	0.001868	7.75	0.01300

Table 2.3. Matrix failure properties of MAC/GMC

			Mean	StD	Shape factor	Scale factor
Ultimate axial strain	Direction 11	ε_{11}	0.02150	0.001073	25.00	0.02197
	Direction 22	ε_{22}	0.02150	0.001073	25.00	0.02197
	Direction 33	ε_{33}	0.02150	0.001073	25.00	0.02197
Ultimate shear strain	Direction 23	γ_{23}	0.06609	0.003304	24.95	0.06755
	Direction 13	γ_{13}	0.06609	0.003304	24.95	0.06755
	Direction 32	γ_{32}	0.06609	0.003304	24.95	0.06755

2.1.2 Elastic Properties of Composite

Based on the input properties of constituents in table 2.1, the MAC/GMC microscale analysis generates the nine elastic properties of a composite, as listed in table 2.4. First, the influence of different discretization levels on single-fiber architectures was evaluated using ARCHID 1, 6, 7, and 13, described in figure 2.2. Table 2.4 summarizes the nine elastic properties of a composite using four different RUC ARCHIDs. Since it is a unidirectional, continuous, fiber-reinforced composite, properties in both transverse directions are the same as shown in table 2.4. It seems that the MAC/GMC outputs are converging to the higher RUC ARCHID.

Table 2.4. Elastic values for single-fiber RUCs

RUC types	ARCHID=1	ARCHID=6	ARCHID=7	ARCHID=13
E_{11} (GPa)	159.200	159.200	159.200	159.200
E_{22} (GPa)	8.210	8.114	8.090	8.071
E_{33} (GPa)	8.210	8.114	8.090	8.071
G_{12} (GPa)	3.893	4.199	4.133	4.053
G_{13} (GPa)	3.893	4.199	4.133	4.053
G_{23} (GPa)	2.256	2.256	2.256	2.256
PR_{12}	0.3386	0.3385	0.3385	0.3386
PR_{13}	0.3386	0.3385	0.3385	0.3386
PR_{23}	0.4329	0.4413	0.4423	0.4429

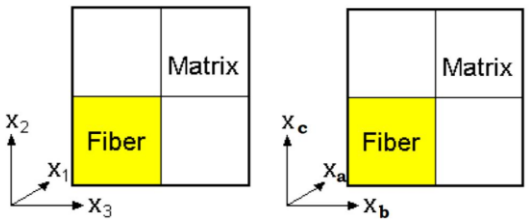

(a) (b)

Figure 2.4. Reference systems: (a) MAC/GMC, and (b) LS-DYNA

Because the MAC/GMC and LS-DYNA use different references shown in figure 2.4, the MAC/GMC output is transformed to the LS-DYNA input as shown in table 2.5.

Table 2.5. Transformation of MAC/GMC output to LS-DYNA input

MAC/GMC output (ARCHID=13)			LS-DYNA Input	
E_{11} (GPa)	159.200	→	E_a (GPa)	159.200
E_{22} (GPa)	8.071	→	E_b (GPa)	8.071
E_{33} (GPa)	8.071			
G_{12} (GPa)	4.053	→	G_{ab} (GPa)	4.053
G_{13} (GPa)	4.053			
G_{23} (GPa)	2.256	→	G_{bc} (GPa)	2.256
PR_{12}	0.3386	$\rightarrow \left(\frac{E_b}{E_a} PR_{12}\right)$	PR_{ba}	0.0171
PR_{13}	0.3386			
PR_{23}	0.4429	→	PR_{cb}	0.4430

In order to define possible distributions of composite properties driven by probabilistic variables of constituents, the Monte Carlo method was utilized. The common steps of the Monte Carlo method consist of:

- Definition of probabilistic distributions of input variables,
- Creation of random inputs representing the defined probabilistic distribution,
- Performing a series of deterministic simulations using input data, and
- Post-processing the output to develop probabilistic distributions of outputs.

LS-OPT software (a standalone design optimization and probabilistic analysis package) [20] was utilized to perform Monte Carlo simulations and to automate the process of running MAC/GMC analyses.

The Monte Carlo analysis was conducted with the random sampling of the Gaussian distributions of the inputs of the MAC/GMC, summarized in table 2.1. The convergence of the Monte Carlo analysis was studied by using different numbers of samples, which is summarized in table 2.6.

Table 2.6. Convergence of Monte Carlo analysis with different number of samples (ARCHID=13)

Samples	100		1,000		5,000		10,000		15,000	
	Mean	StD	Mean	StD	Mean	StD	Mean	StD	Mean	StD
E_a (GPa)	157.006	13.277	155.45	12.819	155.225	13.128	155.359	13.176	155.394	13.226
E_b (GPa)	7.842	0.513	7.822	0.484	7.81	0.498	7.807	0.501	7.808	0.503
G_{ab} (GPa)	3.956	0.503	3.927	0.488	3.915	0.480	3.912	0.480	3.913	0.482
G_{bc} (GPa)	2.217	0.150	2.209	0.137	2.204	0.137	2.204	0.137	2.204	0.138
PR_{ba}	0.016	0.002	0.016	0.001	0.016	0.002	0.016	0.002	0.016	0.002
PR_{cb}	0.415	0.029	0.415	0.028	0.416	0.028	0.416	0.028	0.416	0.029

Table 2.7 shows the difference of standard deviations between different numbers of samples. It can be seen that the Monte Carlo simulation converges when the number of samples increases. Therefore, 10,000 samples were selected for the converged solution of the Monte Carlo simulation because there is less than a 1% error for all parameters between 10,000 and 15,000 samples.

Table 2.7. Difference of standard deviations between different numbers of samples

	100 vs. 1,000	1,000 vs. 5,000	5,000 vs. 10,000	10,000 vs. 15,000
E_a	2.54 %	2.48 %	0.20 %	0.35 %
E_b	5.59 %	3.03 %	0.57 %	0.34 %
G_{ab}	2.22 %	1.51 %	0.13 %	0.35 %
G_{bc}	8.98 %	0.16 %	0.36 %	0.50 %
PR_{ba}	12.23 %	4.07 %	0.96 %	0.46 %
PR_{cb}	4.20 %	1.13 %	1.10 %	0.16 %

In addition, the convergence analysis of the number of fibers was studied. The result of the Monte Carlo simulations of the MAC/GMC with multi-fiber RUC is summarized in table 2.8.

Table 2.8. Distribution data of elastic properties of composite with different number of fibers

	1 fiber		4 fibers		16 fibers		25 fibers	
	Mean	StD	Mean	StD	Mean	StD	Mean	StD
E_a (GPa)	155.359	13.176	155.861	10.725	155.915	9.828	155.762	9.579
E_b (GPa)	7.807	0.501	7.939	0.498	7.942	0.477	7.944	0.486
G_{ab} (GPa)	3.912	0.480	3.791	0.435	3.809	0.429	3.794	0.417
G_{bc} (GPa)	2.204	0.137	2.202	0.140	2.209	0.140	2.204	0.139
PR_{ba}	0.016	0.002	0.017	0.001	0.017	0.001	0.017	0.001
PR_{cb}	0.416	0.028	0.405	0.027	0.404	0.027	0.406	0.026

Figures 2.5 to 2.10 show the distributions of the composite properties. It can be seen that the Monte Carlo simulation converges when the number of fibers increases. 25 fibers were selected for the converged solution.

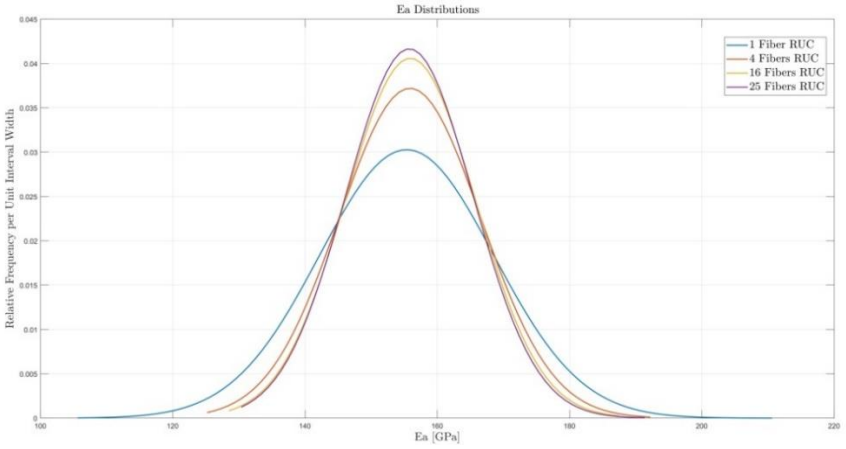

Figure 2.5. E_a distributions

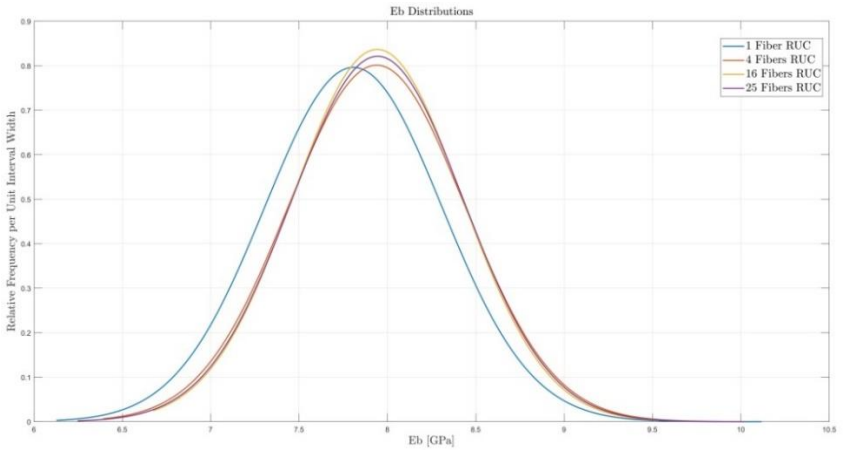

Figure 2.6. E_b distributions

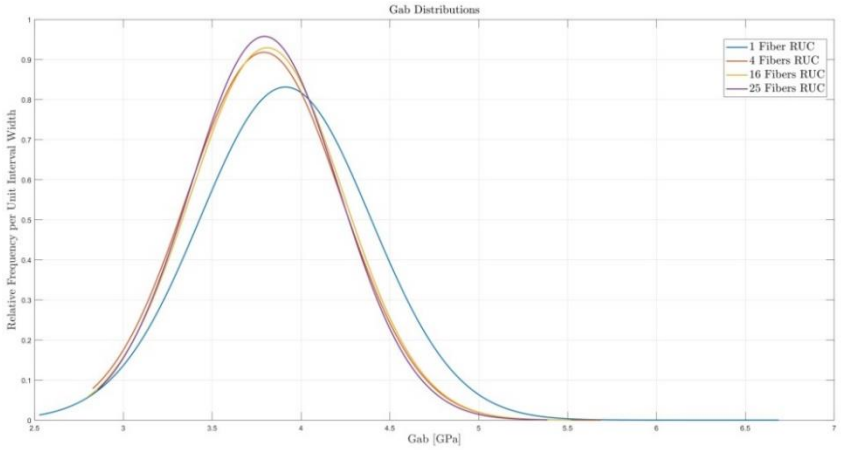

Figure 2.7. G_{ab} distributions

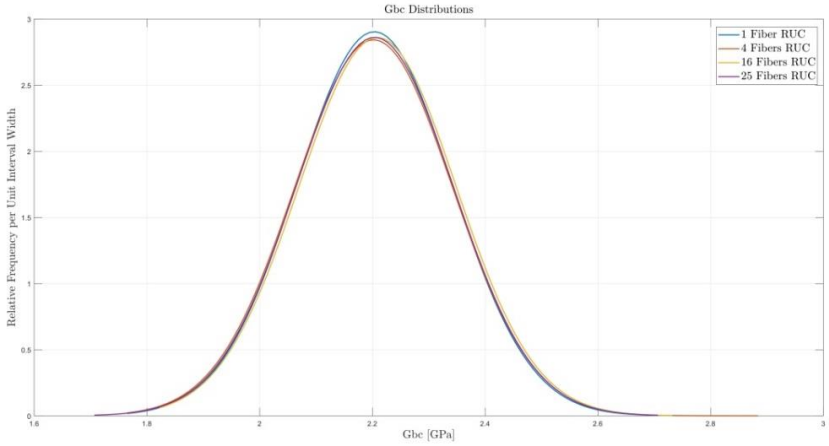

Figure 2.8. G_{bc} distributions

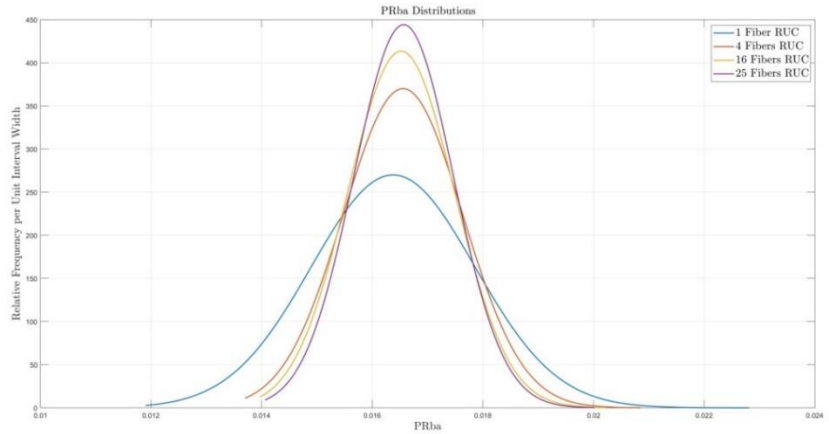

Figure 2.9. PR_{ba} distributions

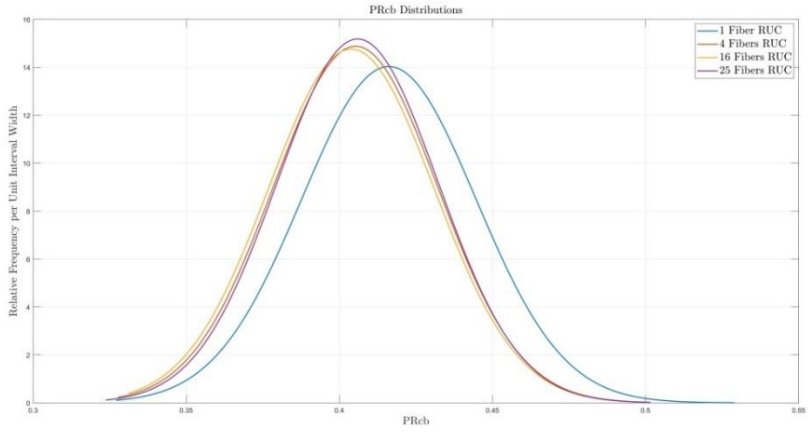

Figure 2.10. PR_{cb} distributions

2.1.3 Failure Properties of Composite

Similarly, the failure properties of the composite are able to be estimated by the MAC/GMC using the results of the elastic properties of the composite described above and the failure input properties of constituents in tables 2.2 and 2.3.

First, the influence of different discretization levels on single-fiber architectures was evaluated using ARCHID 1, 6, 7, and 13. The stress vs. strain curves are shown in figure 2.11. The fiber failure leads to one big drop while the matrix failure shows many small drops depending on the RUC ARCHID. Considering that the ultimate strains will be picked at the point that σ=0, it can be seen that all RUC ARCHIDs have the same ultimate strain.

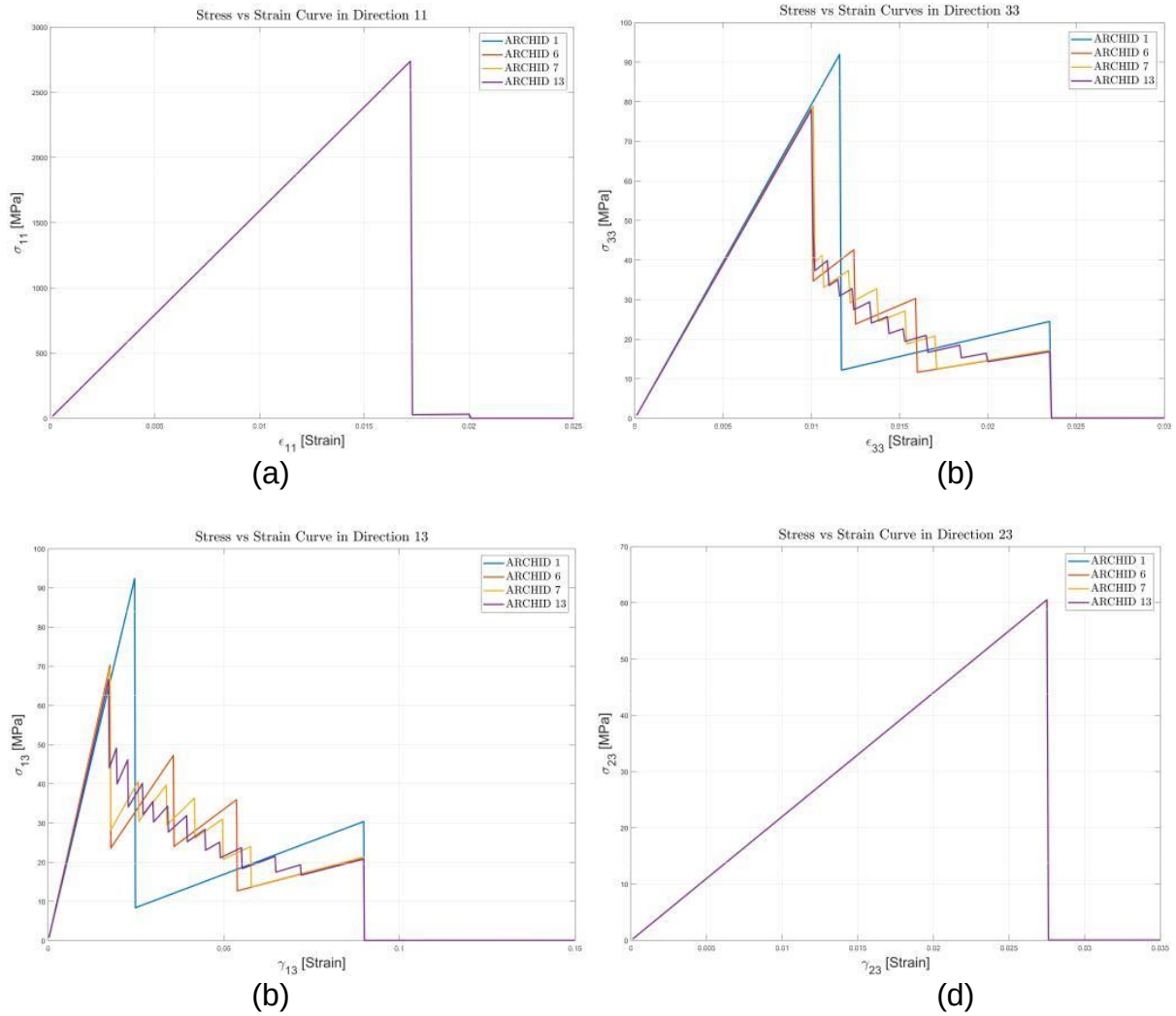

Figure 2.11. Comparison of stress vs strain curves of four different single-fiber RUCs: (a) σ_{11} vs. ε_{11}, (b) σ_{33} vs. ε_{33}, (c) σ_{13} vs. γ_{13}, and (d) σ_{23} vs. γ_{23}

The Monte Carlo analysis was conducted with the random sampling of the Weibull distributions of the failure inputs of the MAC/GMC, summarized in tables 2.2 and 2.3. Figure 2.12 shows the distributions of the failure properties of the composite obtained from the Monte Carlo simulations of the MAC/GMC with multi-fiber RUC. The Monte Carlo simulation converges when the number of fibers increases.

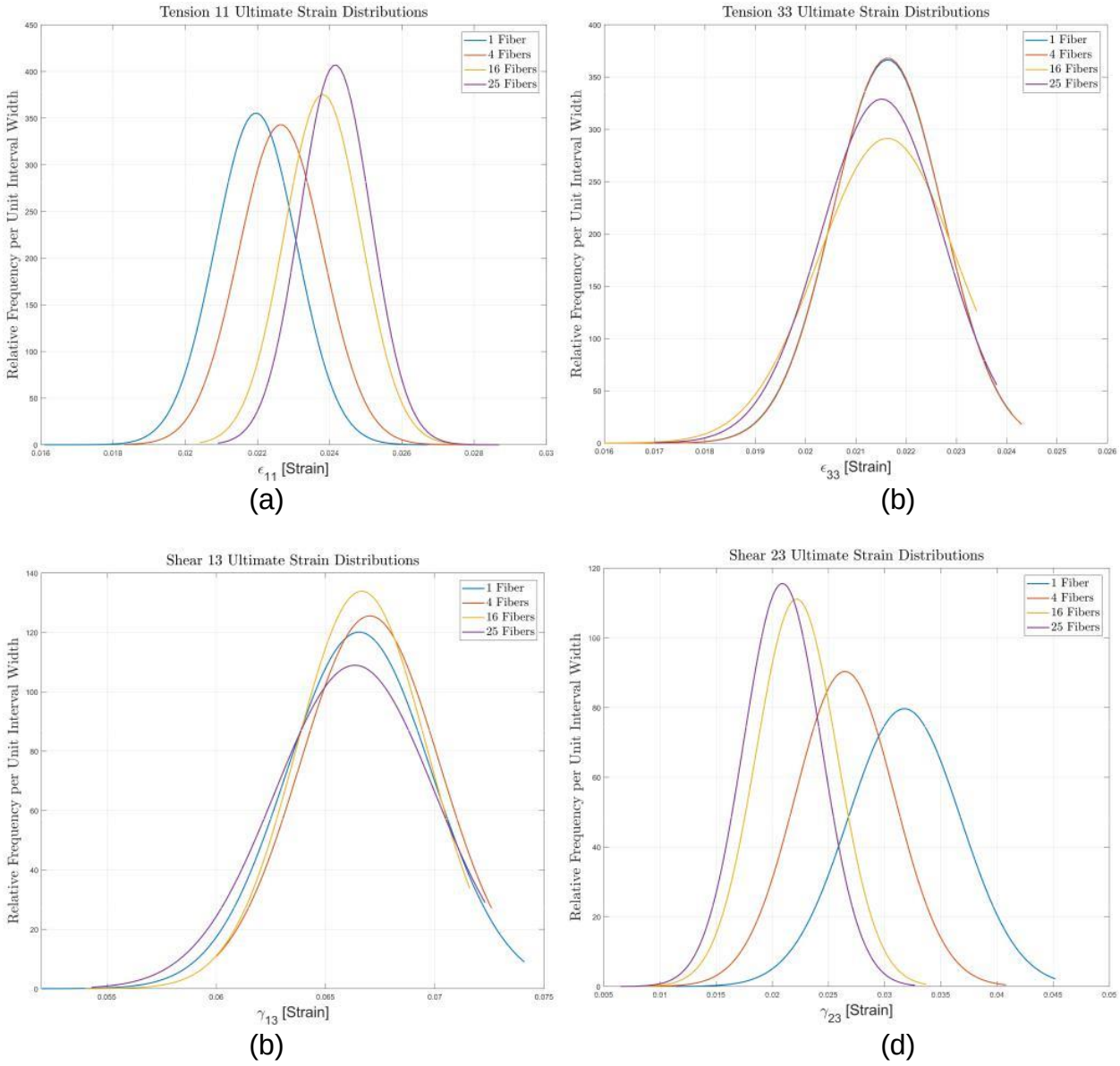

Figure 2.12. Failure distributions: (a) ε_{11}, (b) ε_{33}, (c) γ_{13}, and (d) γ_{23}

Table 2.9. Distribution data of failure properties of composite with different number of fibers

	1 fiber		4 fibers		16 fibers		25 fibers	
	Mean	StD	Mean	StD	Mean	StD	Mean	StD
ε_{11}	2.20E-02	1.12E-03	2.26E-02	1.16E-03	2.38E-02	1.06E-03	2.42E-02	9.80E-04
γ_{23}	3.18E-02	5.01E-03	2.65E-02	4.42E-03	2.22E-02	3.59E-03	2.09E-02	3.45E-03

2.1.4 Summary

The process of evaluating the distributions of elastic and failure properties of the composite using the MAC/GMC has been described. This probabilistic microscale analysis process is easily applicable to different composite materials. All the probabilistic distribution functions obtained in this microscale analysis process will be used for the macroscale stochastic impact simulations using LS-DYNA.

2.2 STOCHASTIC MACROSCALE ANALYSIS

In general, Finite Element (FE) simulations provide deterministic results. In the case of ballistic impact simulations, for a specific set of inputs (material model and parameters, geometry, mesh, impact velocity, and others) the result should always be the same. For a specific impact velocity simulated, the result will be either penetration or containment. In reality, however, due to several effects like, for example, impurities, inclusions, variations in fiber tensile strengths, and others, composite material properties show statistical variations. Therefore a “zone of mixed results” exists, in which for a given impact velocity the projectile will sometimes penetrate the composite plate and sometimes not. Deterministic simulations are not able to reproduce or predict this probability of penetration. To replicate this behavior, the goal was to use stochastic variations of the material properties of the composite as input to the simulations.

The goal was to create the required baseline material input to study the effects of statistical variation of material parameters on the response in ballistic impact simulations. This study can furthermore be helpful as a baseline comparison case to newly developed composite material models, as it describes a currently commonly used material model for ballistic impact simulations, the steps necessary to obtain useful results, and the limitations of the model.

As validation of the *MAT_213 material model was still ongoing at the time of this study, the widely used LS-DYNA material model *MAT_054 was used for the stochastic macroscale analysis. Therefore the *MAT_054 in conjunction with a failure criterion available in *MAT_ADD_EROSION was verified and validated in the previous chapter. After the validation of the material model, the sensitivity to the scaling of individual material properties was analyzed to identify which parameters showed a higher influence in low- and high-velocity ballistic impact simulations. By identifying these influential parameters, a future implementation of stochastic variations into the

*MAT_213 material model could be limited to these parameters to simplify the implementation and the material model input.

Using the validated *MAT_054 material card as a baseline, Python scripts were then used to create a user-specified number of materials that were then randomly assigned to the plate elements. The material parameters of these material cards followed the MAC/GMC-obtained stochastic variations as described in the previous chapter. By shuffling the assignment of materials to elements, a variation in the response of the composite was realized, and using logistic regression analysis, a probability of penetration for different impact velocities was obtained.

2.2.1 Influence of Variation of Elastic Material Parameters in Ballistic Impacts

Due to a large amount of input parameters to the *MAT_213 material model, the influence of the elastic material properties in the *MAT_054 model on ballistic impacts was studied to identify the most important variables for a future stochastic implementation of *MAT_213. The material properties were scaled up individually by the standard deviation percentage obtained using MAC/GMC in table 2.8 and their influence on the simulation results compared qualitatively by looking at the plate displacement in the low-velocity impact (LVG1067 – 155 ft/sec). In these low-velocity impacts, failure did not have an influence on the results. In the higher-velocity impact tests, on the other hand (LVG1075 – 385 ft/sec, LVG1074 – 417 ft/sec and LVG1076 – 454 ft/sec), failure occurred in the plate, and therefore influenced the obtained results.

In the low-velocity impact of LVG1067, the Young's modulus in fiber direction (EA) was clearly the dominating material parameter, as shown in figure 2.13. All other material parameters did not influence the plate displacement results significantly.

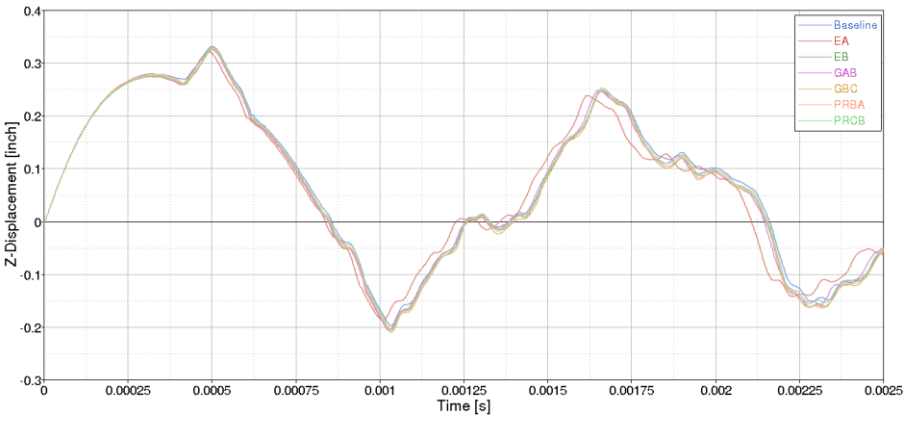

Figure 2.13. LVG1067 with elastic properties scaled individually

In the higher-velocity impacts of LVG1075, LVG1074, and LVG1076, the composite plate was damaged, and in the cases of LVG1074 and LVG1076 fully penetrated. Figures 2.14 to 2.16 show the resultant projectile displacements for the different scaled

elastic properties in the three impact tests. In the contained case (LVG1075), the shear modulus 12 (GAB) and the Poisson's ratio 31 (PRCB) influence the results most significantly.

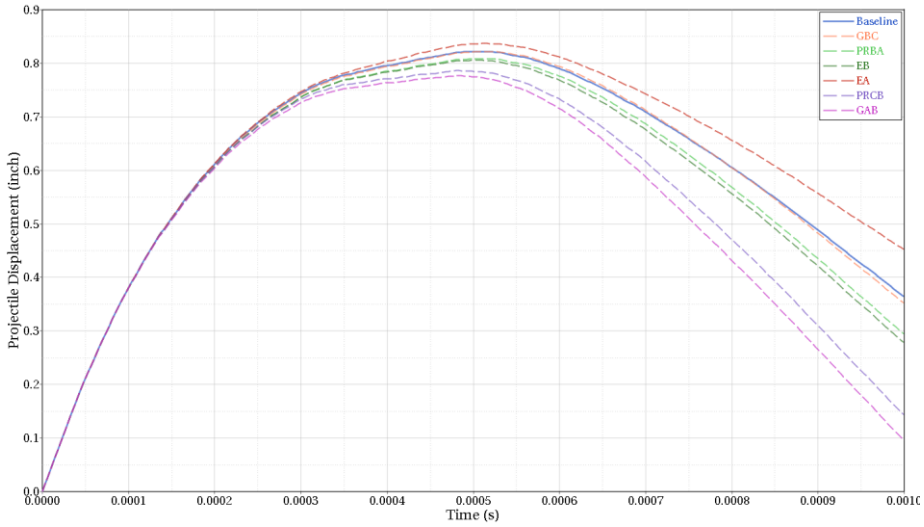

Figure 2.14. Projectile impact direction displacement in LVG1075

In LVG1074, the most important variables are the shear moduli in 23 (GBC) and 12 direction (GAB).

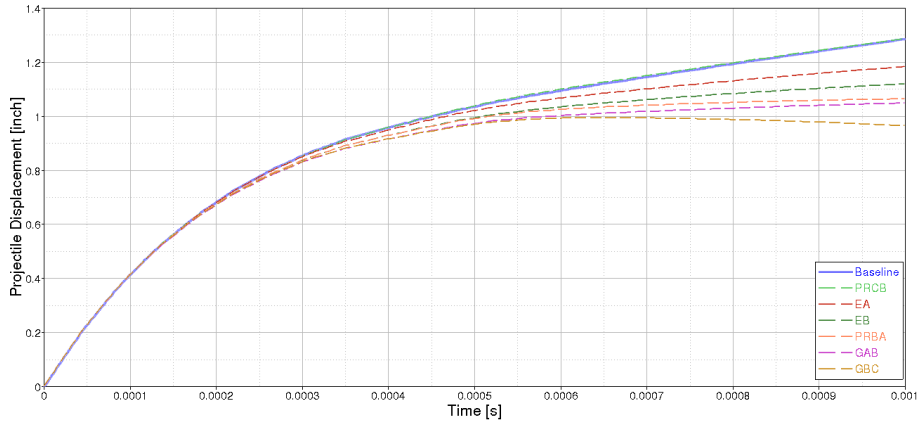

Figure 2.15. Projectile impact direction displacement in LVG1074

Similar results are obtained with the highest simulated velocity of LVG1076, with both shear moduli having the biggest impact on the result.

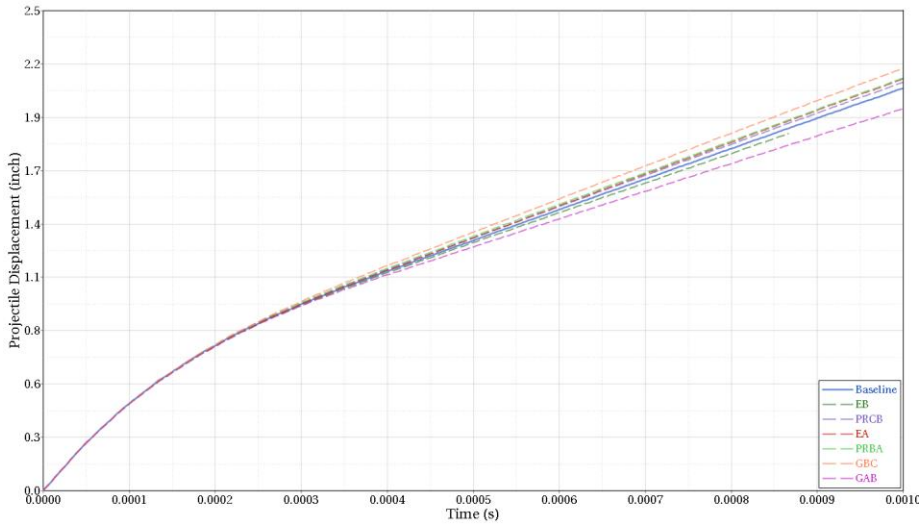

Figure 2.16. Projectile impact direction displacement in LVG1076

To sum up, in the low-velocity impact, where failure did not occur, the Young's modulus was the dominating material parameter; in the higher-velocity impacts the shear moduli.

2.2.2 Influence of Variation of Failure Parameters in High-Velocity Impacts

The influence of the defined failure parameters of the *MAT_ADD_EROSION card was studied using the three high-velocity impacts LVG1075, LVG1074 and LVG1076. The failure parameters were scaled by the absolute difference between mean and maximum/minimum that was obtained using MAC/GMC in table 2.9.

For all three ballistic impact velocities, the clearly dominating factor was the tensorial shear strain at failure (EPSSH). Figures 2.17 to 2.19 show the projectile velocity over time in the three ballistic impact tests for the scaled failure parameters.

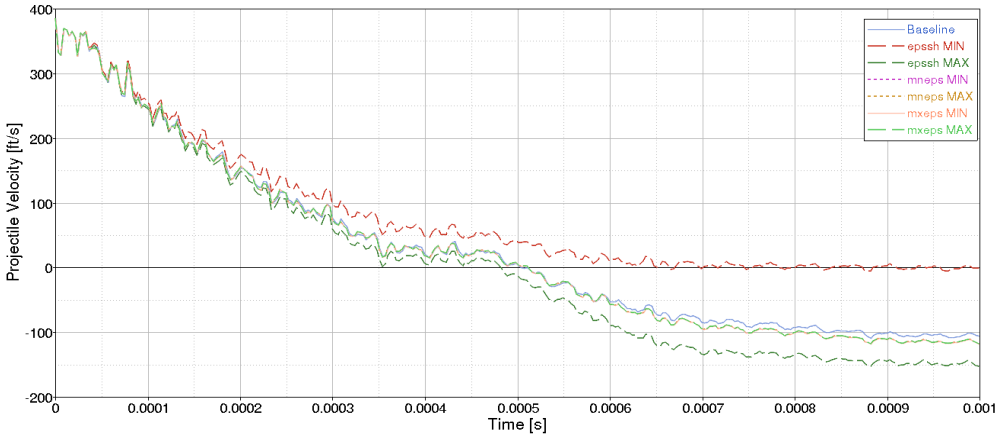

Figure 2.17. Projectile velocity in LVG1075

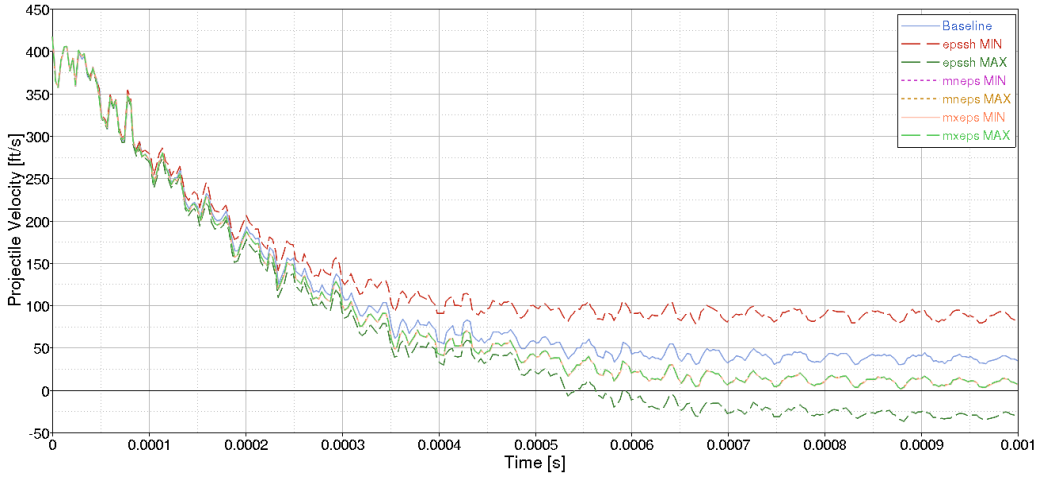

Figure 2.18. Projectile velocity in LVG1074

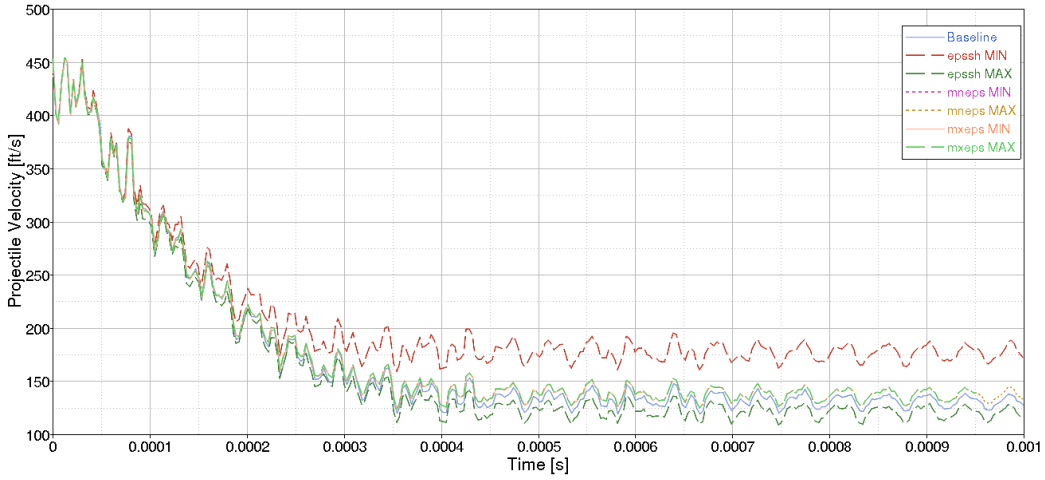

Figure 2.19. Projectile velocity in LVG1076

2.2.3 Determining Probability of Penetration using Statistical Variations of Material Parameters

The overall goal of the stochastic analysis is to provide a computational framework to analyze stochastic variations of material parameters and to incorporate their effects into ballistic impact simulations. The stochastic variations of the material parameters that were obtained using the micro-mechanics code MAC/GMC were used to create 100 LS-DYNA material cards. Figure 2.20 shows as an example the Young's modulus in fiber direction (EA) for the 100 material cards. These material cards were then randomly assigned to elements of the composite plate with every material card being assigned to the same total number of elements.

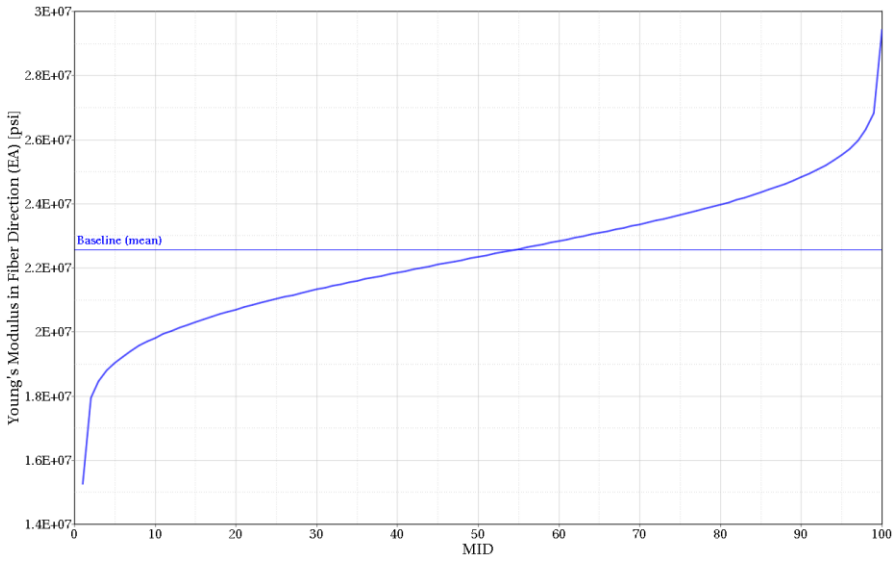

Figure 2.20. Example distribution of Young's modulus in fiber direction

50 ballistic simulations were then set up, with velocities being picked randomly in a range in which the 50% probability of penetration was expected due to the previous test and simulation results. The assignment of material IDs to the elements was reshuffled between every simulation. Therefore the impact region could sometimes contain “weaker” materials and sometimes “stronger” materials. Each simulation was run with two different material input sets, once with all material parameters being varied and once with a variation of only the most influential parameters as identified in the earlier studies.

Table 2.10 shows the Boolean results of the ballistic impact simulations with 0 representing projectile containment and 1 representing penetration of the plate. Containment was defined as the projectile displacement showing a maximum before the termination time of the simulation, meaning that the projectile rebounded.

Table 2.10. Results of ballistic impact simulations

ID	Velocity (in/sec)	All parameters with variation	EA, GAB, GBC, EPSSH with variation	ID	Velocity (in/sec)	All parameters with variation	EA, GAB, GBC, EPSSH with variation
1	4,614	0	0	26	5,017	1	1
2	4,622	0	0	27	5,023	1	1
3	4,627	0	0	28	5,033	1	1
4	4,640	0	0	29	5,040	1	1
5	4,641	0	0	30	5,044	1	1
6	4,670	0	0	31	5,044	1	1
7	4,715	0	0	32	5,047	1	1
8	4,785	0	0	33	5,050	1	1
9	4,808	0	0	34	5,053	1	1
10	4,825	0	0	35	5,056	1	1
11	4,906	0	1	36	5,063	1	1
12	4,920	0	0	37	5,067	1	1
13	4,926	1	1	38	5,074	1	1
14	4,927	0	1	39	5,080	1	1
15	4,935	0	1	40	5,082	1	1
16	4,968	1	0	41	5,093	1	1
17	4,970	1	1	42	5,130	1	1
18	4,974	1	1	43	5,158	1	1
19	4,977	1	0	44	5,159	1	1
20	5,000	1	1	45	5,160	1	1
21	5,006	1	1	46	5,194	1	1
22	5,006	0	1	47	5,237	1	1
23	5,008	1	1	48	5,253	1	1
24	5,009	0	1	49	5,254	1	1
25	5,011	1	1	50	5,272	1	1

In figure 2.21, the logistic regression functions indicating the probabilities of penetration that were computed for the two sets of data are shown with the raw data points. The two physically tested impact velocities are shown in green as well. The blue curve shows the regression function for the material input, where all parameters were stochastically varied, and the red curve where only the most influential material parameters were varied. The “zone of mixed results”, or in other words the velocity range from lowest velocity causing penetration to highest velocity in which the projectile was contained for both cases, is similar. The velocity at 50% likelihood of penetration with all parameters varied is 4,916 in/sec (409.7 ft/sec), and with the most influential parameters varied 4,951 in/sec (412.6 ft/sec), which is a difference of less than 1%. As the difference between the two analysis is quite low, in future stochastic implementations of *MAT_213, the focus should lie on the here-determined influential parameters.

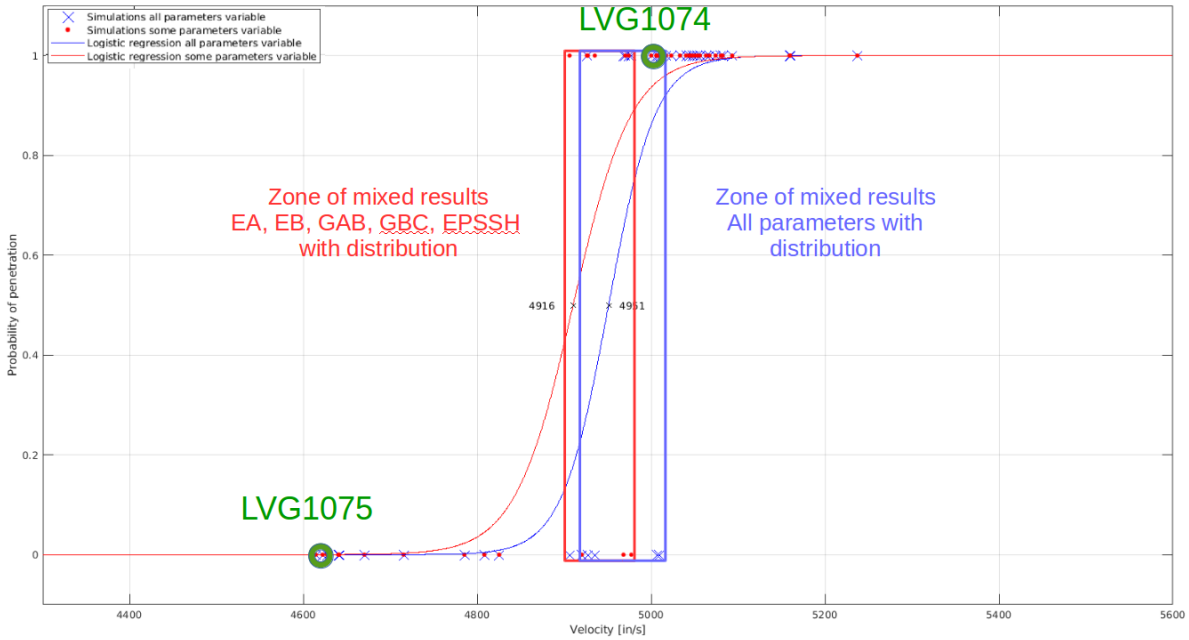

Figure 2.21. Logistic regression functions and zone of mixed results for both sets of simulations

For a comparison of the determined probability range to the ballistic impact tests conducted at NASA, figure 2.22 shows the test impact velocity vs. exit/rebound velocity obtained in the tests in blue. The simulated probability range from 99% probability contained to 99% probability of penetration is shown in yellow. The red marker highlights the 50% probability of penetration velocity.

The simulation results suggest that for the LVG1075 impact velocity of 385 ft/sec, in 100% of the time the projectile will be contained, as it also was in the test. For the impact velocity of the LVG1074 test (417 ft/sec), however, the computed probability of penetration was ~90%. In the physical test, the projectile penetrated the plate and exited on the back with a relatively low-velocity of ~25 ft/sec, which suggests that in certain circumstances the projectile could have been contained for that velocity.

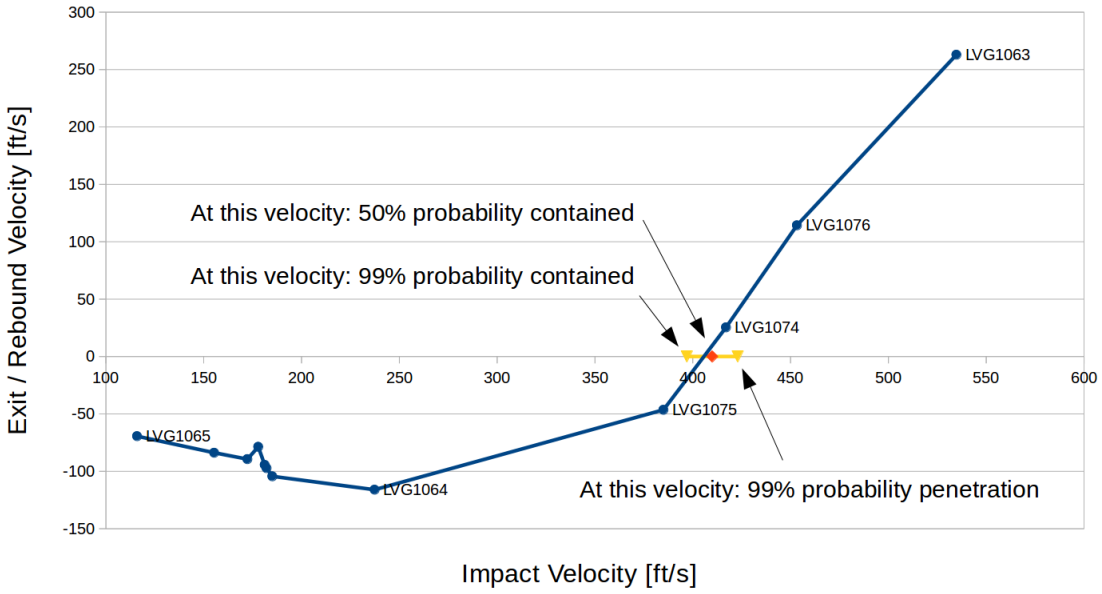

Figure 2.22. Simulation probabilities in comparison to NASA ballistic impact tests

Overall, the probabilities of penetration that were obtained in the simulations seem to agree reasonably well with the limited ballistic impact test data that was available in the critical velocity region.

2.2.4 Summary

A computational framework for the determination of probabilities of penetration in ballistic impact tests that takes into account statistical variation of material parameters in composites was introduced. To obtain physically meaningful stochastic variations of these material parameters, the micro-mechanics solver MAC/GMC was used. These variations of material parameters were incorporated into a ballistic impact simulation utilizing a LS-DYNA *MAT_054 material card that was validated as part of this study. Several impact velocities with random distributions of LS-DYNA material cards that followed the MAC/GMC material parameter distributions were conducted and logistic regression analysis used to obtain probabilities of penetration.

Reasonable agreement between the obtained probabilities of penetration and the limited test results in the critical region was found. The results of this study will support the implementation of stochastic capabilities into the newly developed *MAT_213 material model.

3. COMPARISON OF DETERMINISTIC TO PROBABILISTIC SIMULATIONS

3.1 IMPLEMENTATION OF STOCHASTIC FUNCTION INTO *MAT_213

In the previously conducted study, *MAT_054 was used to identify the most influential material parameters for ballistic impact simulations. How these material parameters translate to the *MAT_213 input is shown in table 3.1. After the implementation of the stochastic capabilities for *MAT_213 is completed, the user will be able to input stochastic distributions of scale factors for each of the shown material directions. The stochastic function for *MAT_213 will be implemented as *DEFINE_STOCHASTIC_ VARIATION_MAT213.

Table 3.1. *MAT_213 equivalent material parameters to *MAT_054

*MAT_054 scalar input	*MAT_213 tabulated input	Order in the keyword of *DEFINE_STOCHASTIC_VARIATION _MAT213
EA	Tension and Compression in 1-direction	1
GAB	Shear 12	2
	Shear 13	3
GBC	Shear 23	4
EPSSH	In-plane failure	5
	Out-of-plane failure	6

An example of this new LS-DYNA keyword card is shown in figure 3.1. In this example, the stochastic definition is given the ID 1 which is valid for part ID (pid) 1. The variable IRNG defines if a (pseudo) or a (true) random number generator should be used. This way a user can obtain the same results when running the same input several times (pseudo-random), or possibly get variation in the results (true-random).

```
*DEFINE_STOCHASTIC_VARIATION_MAT213
$     id_sv       pid    pid_typ      irng
          1         1          0         0
$    vartyp    corlgrp        r1        r2
          1         0      0.75      1.25
          1         0      0.75      1.25
          1         0      0.75      1.25
          1         0      0.75      1.25
          1         0      0.75      1.25
          1         0      0.75      1.25
```

Figure 3.1. Example input for *MAT_213 stochastic option

The VARTYP variable defines what type of stochastic variation should be used. Setting VARTYP to 1, for example, allows for the definition of a uniform random distribution in the interval R1 to R2. If the variable should not follow a distribution, the user can set

VARTYP to zero and therefore set all scale factors to 1 which leaves the material parameter unchanged. Other options allow for the definition of a Gaussian distribution or defining a distribution following an input curve of a probability distribution function or a cumulative distribution function.

The use of the CORLGRP variable allows specifying which of the parameters should be correlated or not. An example input could correlate the deformation related variables (Tension and Compression in 1-direction, Shear 12, 13, 23) by specifying the same integer value for their CORLGRP parameter, and then additionally correlate the two failure parameters (for in-plane and out-of-plane failure) between each other by giving them a different CORLGRP integer value. Table 3.2 shows an overview of all available options and explanations for the new keyword.

Table 3.2. Option of *DEFINE_STOCHASTIC_VARIATION_MAT213

VARIABLE	DESCRIPTION
ID_SV	Stochastic variation ID. A unique ID number must be used.
PID	*PART ID or *SET_PART ID.
PID_TYP	Flag for PID type. If PID and PID_TYP are both 0, then the properties defined here apply to all shell and solid parts using materials with the STOCHASTIC option. EQ.0: PID is a *PART ID. EQ.1: PID is a *SET_PART ID
IRNG	Flag for random number generation. EQ.0: Use deterministic (pseudo-) random number generator. The same input always leads to the same distribution. EQ.1: Use non-deterministic (true) random number generator. With the same input, a different distribution is achieved in each run.
VARTYP	Variation type for scaling the yield stress. EQ.0: The scale factor is 1.0 everywhere. EQ.1: The scale factor is a random number in the uniform random distribution in the interval defined by R1 and R2. EQ.2: The scale factor is a random number obeying the Gaussian distribution defined by R1, R2, and R3. EQ.3: The scale factor is defined by the probability distribution function defined by curve LCID. EQ.4: The scale factor is defined by the cumulative distribution function defined by curve LCID.
CORLGRP	Correlation group number. If CORLGRP is 0, then the random number for the distribution is uncorrelated with all the other distributions. The same random number is used for evaluating all the distributions having the same positive integer value for CORLGRP.
R1, R2, R3	Real values to define the stochastic distribution.
LCID	Curve ID defining the stochastic distribution.

3.2 SINGLE-ELEMENT LEVEL STUDY

To verify that *DEFINE_STOCHASTIC_VARIATION_MAT213 produces the expected results, single-element simulations in the effected directions were conducted. In the first round of simulations, the four deformation parameters for which stochastic capabilities were implemented were varied individually and 10 simulations per variable were run. In another round of simulations, all four deformation parameters were varied at the same time and the simulation was again repeated 10 times.

A similar verification process was used for the two failure parameters. First, they were tested individually, and in another round both variables were varied at the same time. The last step in the single-element verification was to run all single-element cases several times, while defining a stochastic variation for all parameters. Table 3.3 shows an overview of all single-element verification simulations.

Table 3.3. Single-element verification cases

	Stochastic variables varied per case	Cases	Number of simulations per case	Total simulations
Deformation parameters individual	(1/4)	4	10	40
All deformation parameters	(4/4)	1	10	10
Failure parameters individual	(1/2)	2	10	20
All failure parameters	(2/2)	1	10	10
All parameters	(6/6)	1	10	10
			Total:	**90**

3.2.1 Variation of Deformation Properties

In the first single-element simulations, the deformation parameters were varied individually. To verify that the variation of the tension and compression input in 1-direction leads to the expected results, tension and compression single-element simulations were conducted.

Figure 3.2 (tension) and figure 3.3 (compression) show the results for 10 different simulations (Run 1-10) and a baseline simulation (solid red line). As the scale factor was varied with a uniform random distribution in the interval 0.9 to 1.1, all stress vs. strain results lie within an envelope of two curves that would be defined by the baseline curve scaled up by a factor of 1.1 or down by a factor of 0.9. The results shown here can only be obtained by using a (true) random number generator, which can be realized by setting IRNG to one.

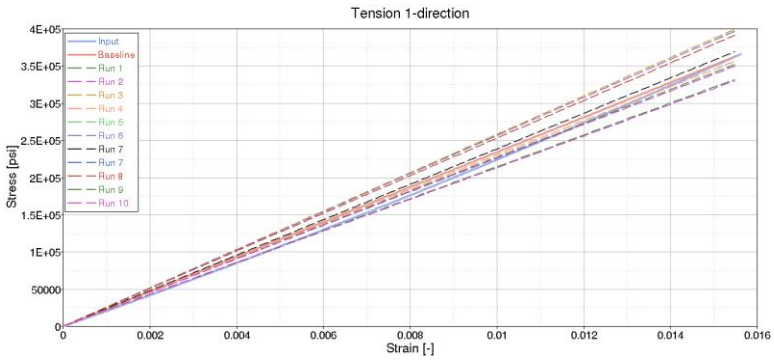

Figure 3.2. Stress vs. strain stochastic tension 1-direction

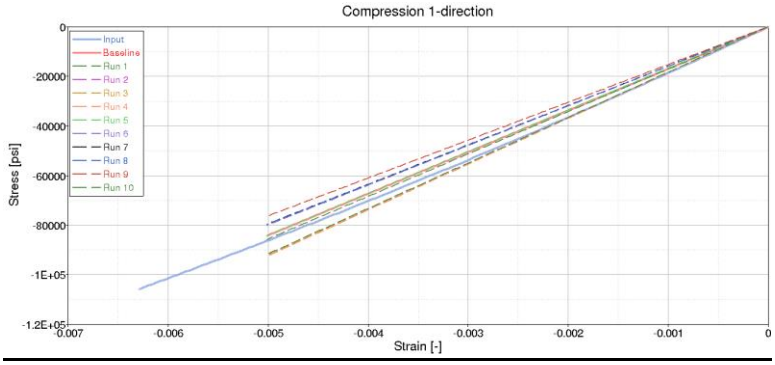

Figure 3.3. Stress vs. strain stochastic compression 1-direction

Figure 3.4 shows the stochastic variation keyword card that was used to obtain the results. As only the first VARTYP parameter in line 2 in figure 3.4 is set to one, only tension and compression in 1-direction is affected.

```
*DEFINE_STOCHASTIC_VARIATION_MAT213
$     id_sv       pid    pid_typ       irng       numv    num_beg
          1         1          0          1
$    vartyp    corlgrp         r1         r2         r3
          1          0        0.9        1.1
          0          0        0.9        1.1
          0          0        0.9        1.1
          0          0        0.9        1.1
          0          0        0.9        1.1
          0          0        0.9        1.1
```

Figure 3.4. *DEFINE_STOCHASTIC_VARIATION_MAT213 for tension/compression 1-direction variation only

In the shear 12 case, the *DEFINE_STOCHASTIC_VARIATION_MAT213 input from figure 3.5 was changed to only apply a stochastic scale factor to the shear 12-direction. Therefore, the first VARTYP parameter was set to zero and only the second one was

set to one. Figure 3.5 shows the results for 10 different runs and in solid red the baseline (deterministic) result. Again, the whole stress vs. strain curve is effectively scaled up and down by a maximum of 10%.

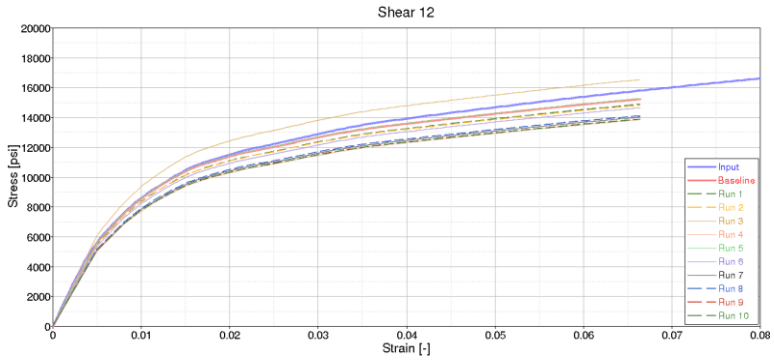

Figure 3.5. Stress vs. strain stochastic shear 12

To apply a stochastic variation to the shear 23-direction, VARTYP in line three of *DEFINE_STOCHASTIC_VARIATION_MAT213 has to be set to one. Figure 3.6 shows the results in 10 simulations and the baseline result in solid red.

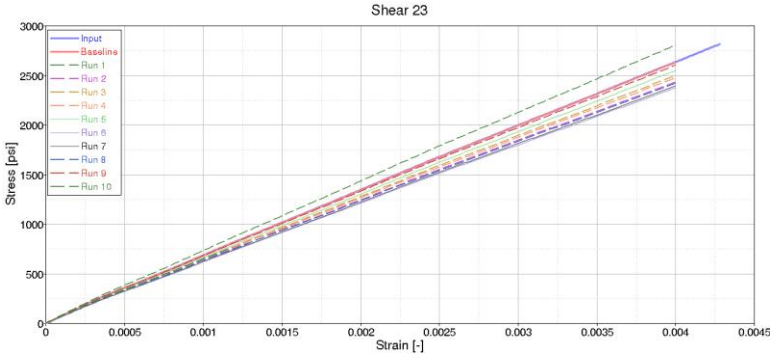

Figure 3.6. Stress vs. strain stochastic shear 23

The shear 13 input can be varied by setting VARTYP in the fourth line of *DEFINE_ STOCHASTIC_VARIATION_MAT213 to one. Figure 3.7 shows the results. The deviation from the input curve (solid blue) is due to boundary conditions that do not represent pure 13 shear.

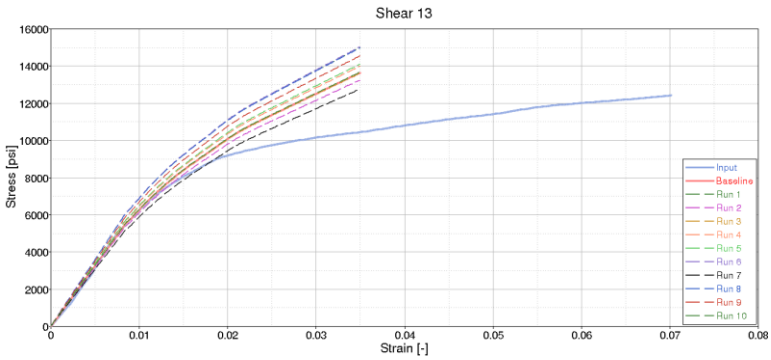

Figure 3.7. Stress vs. Strain stochastic shear 13

By setting the first four VARTYP parameters to one, all deformation properties for which stochastic capabilities were implemented in *MAT_213 can be varied at the same time. Figure 3.8 shows the results for 10 runs of five different elements that were obtained with the same input. All curves are scaled independently (if CORLGRP is not defined or set to zero).

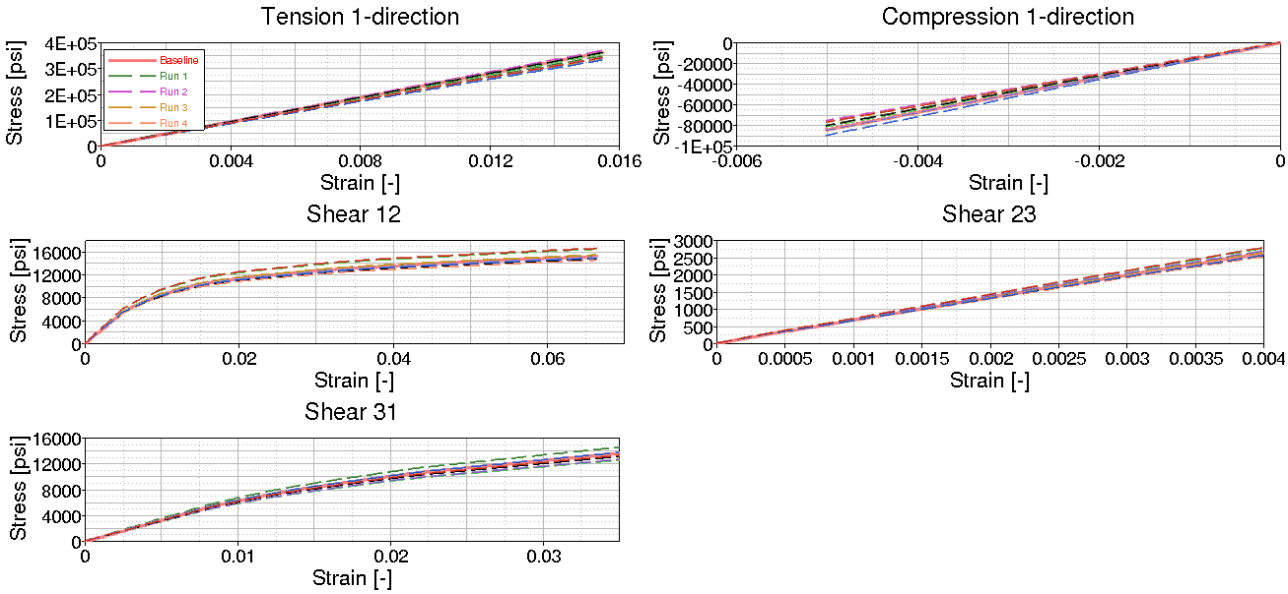

Figure 3.8. Stress vs. Strain, all deformation properties with variation

3.2.2 Variation of Parameters of the Generalized Tabulated Failure Criterion

In addition to the four deformation properties, capabilities to define stochastic variation for the Generalized Tabulated Failure Model were implemented. The tabulated failure model treats the in- and out-of-plane failure separately and therefore both were also treated separately in the stochastic implementation.

To achieve a variation of the in-plane failure, the in-plane failure radius was scaled by the stochastic variable.

Figure 3.9 shows 10 repetitions of nine single-element simulations and how the results were affected by the scaled failure radius. As only the in-plane failure radius is scaled, only the in-plane cases (tension/compression 1-direction and shear 12) are affected. The solid blue line represents the baseline (deterministic) simulation. When the end of the input stress vs. strain curve is reached, *MAT_213 computes a tangent modulus of 10% times the Young's modulus in that direction. Therefore, for example in tension in 2-direction, the stress vs. strain output looks bilinear. If now the failure radius is scaled up, in some cases the point of failure was not reached during the simulation time. This behavior can be seen in tension and compression in 2-direction in these cases, but could be avoided by either changing the *MAT_213 input curves, the tabulated failure surface, or by choosing different variation scale factors.

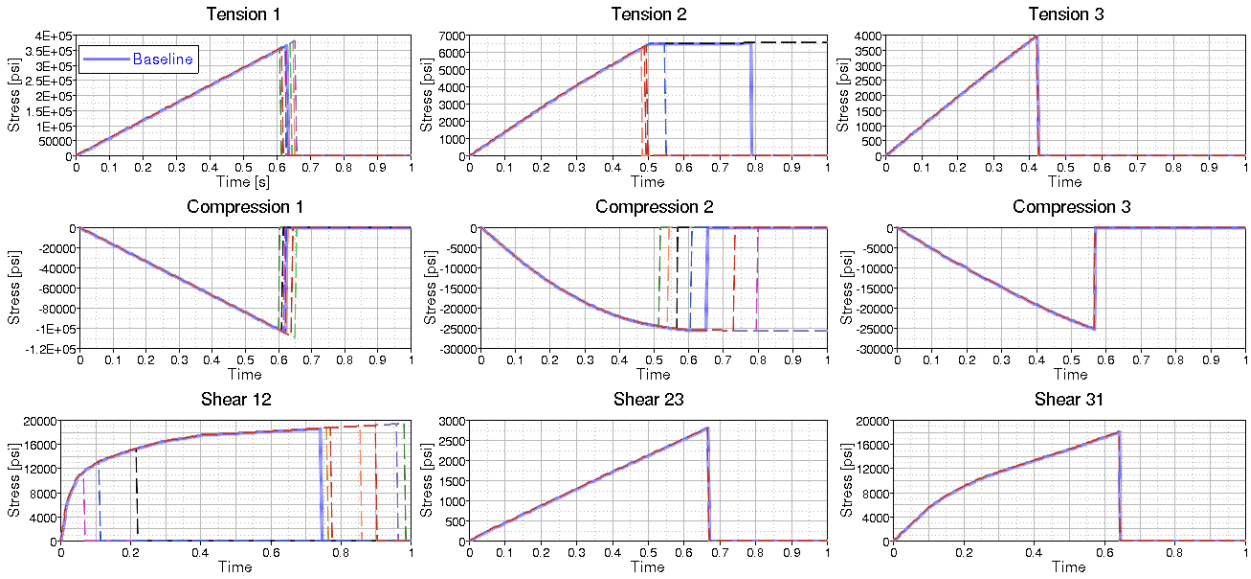

Figure 3.9. Stress vs. Strain in-plane failure with variation with under integrated elements

The simulations in figure 3.9 were run with under-integrated elements. If the same simulations are repeated using fully-integrated elements (8-integration points), the elements fail much earlier than in the deterministic simulation, as shown in figure 3.10. The problem in these cases is that the failure radius in every integration point is scaled by a stochastic factor and, because the element is eroded when the first integration point fails, this will always happen in the “weakest” point with the lowest scale factor. Statistically, the chances are very high that at least one of the eight integration points has a scale factor lower than one and therefore the element will fail earlier than the deterministic simulation in most cases. This issue could be addressed by using a

variation that takes this into account by applying predominantly scale factors greater than one.

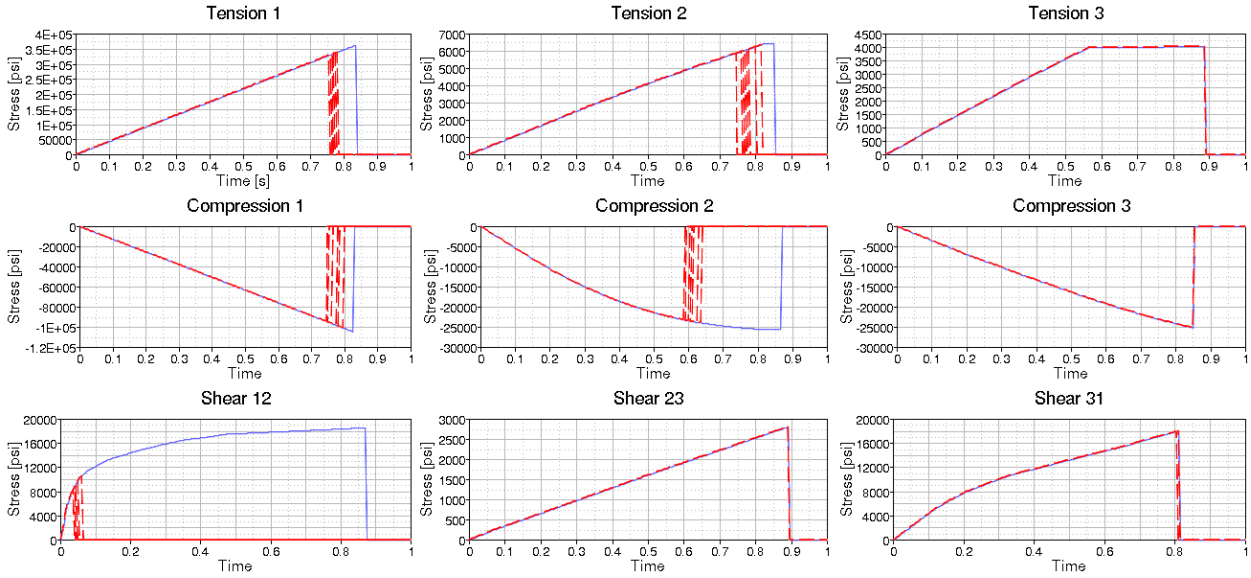

Figure 3.10. Stress vs. Strain in-plane failure with variation with fully integrated elements

To apply a stochastic variation to the out-of-plane failure radius, the user must set the last VARTYP parameter (line 6 in figure 3.4) to one. Figure 3.11 shows that only the out-of-plane cases (tension/compression 3-direction, shear 23 and 31) are affected by the scaling.

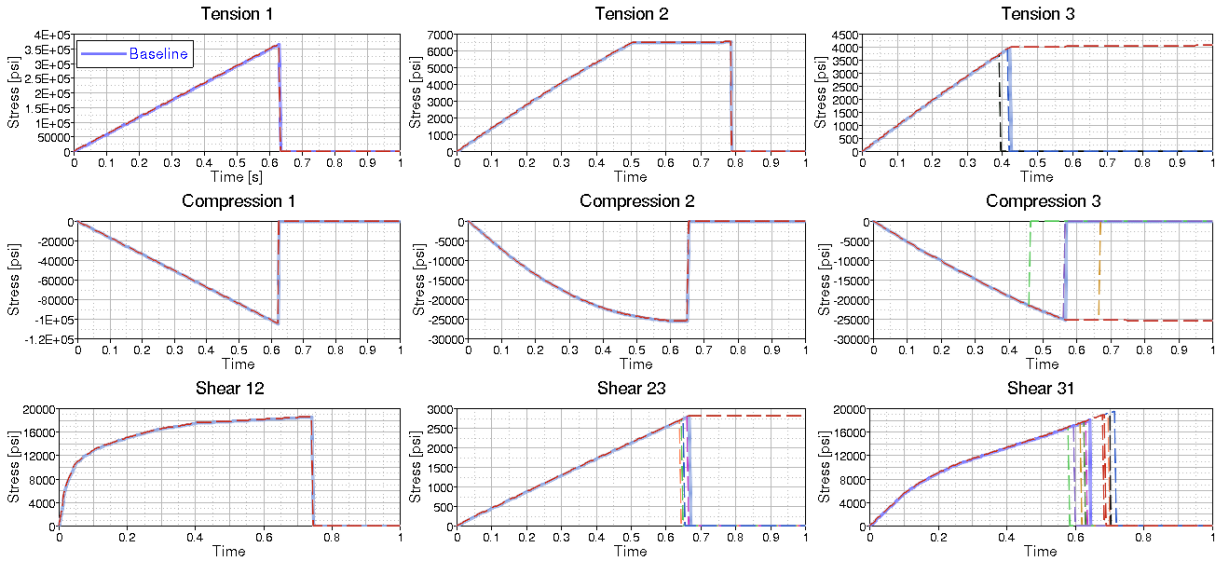

Figure 3.11. Stress vs. Strain out-of-plane failure with variation

The stress vs. strain output in the single-element cases where both the in- and out-of-plane failure radius were scaled by a stochastic variation, are shown in figure 3.12 The results in all individual directions are affected.

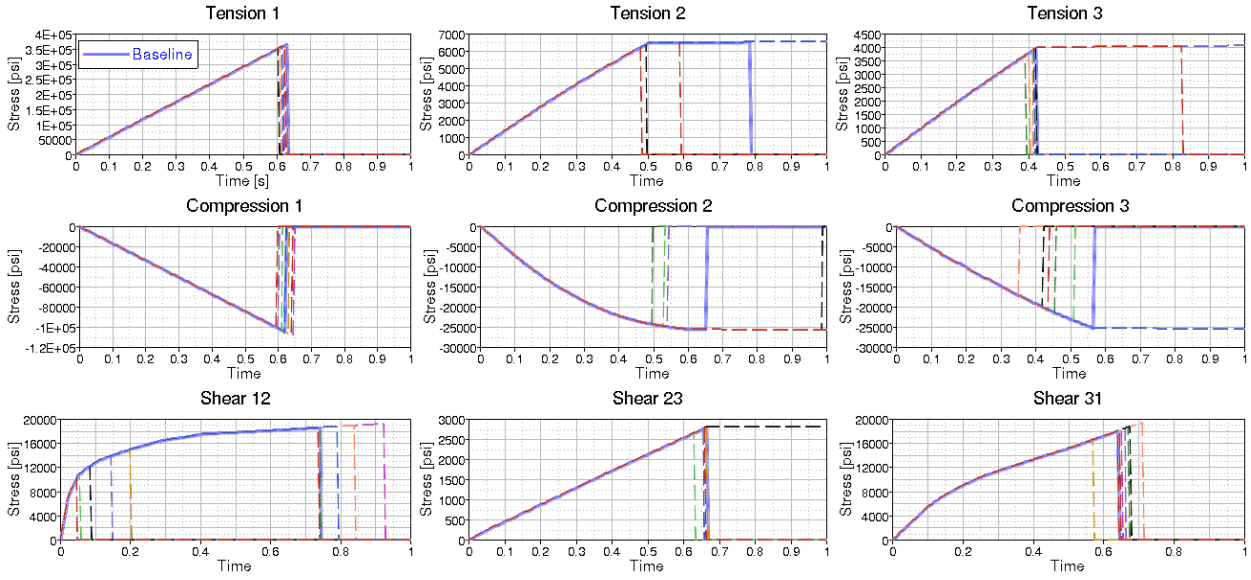

Figure 3.12. Stress vs. Strain in- and out-of-plane failure with variation

3.2.3 Variation of deformation properties and in- and out-of-plane failure radius

In a final set of simulations, all deformation properties and both in- and out-of-plane failure were scaled using stochastic variations. All six VARTYP variables were set to one and the interval of the uniform random distribution was defined by R1 and R2.

Figure 3.13 shows the results in the single-element simulations. In the cases where the deformation properties were scaled (tension/compression 1-direction, shear 12, 23, 31), the whole curve was scaled up and down, and due to the variation in the failure radius the elements fail at higher or lower stresses than in the baseline (deterministic) simulation. The tension/compression in 2- and 3-direction cases are not affected by the scaled deformation properties; however, the failure stresses show a variation.

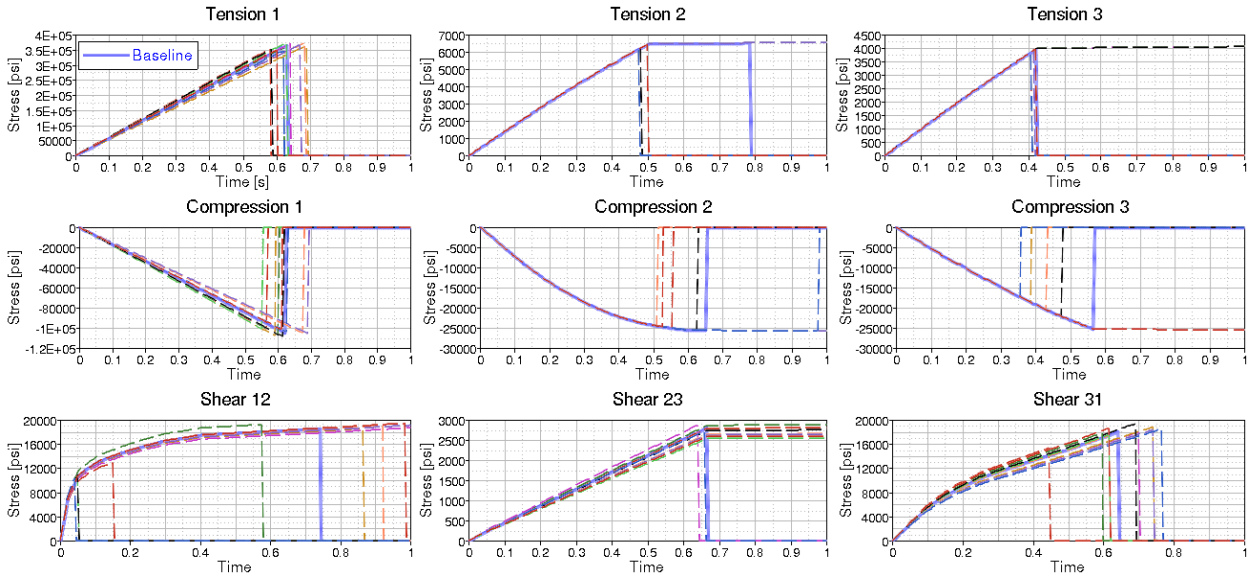

Figure 3.13. Stress vs. Strain, all deformation properties, in- and out-of-plane failure with variation

3.3 COMPONENT LEVEL STUDY

3.3.1 Coupon Simulation

Cross-ply layup coupon simulations were chosen to verify the stochastic option for MAT213 in multi-element simulations. Figure 3.14 shows the dimensions of the specimen and the fiber orientation layup. Since the goal of the study was to access the stability and general functionality of the stochastic option only, the results were not compared to test results.

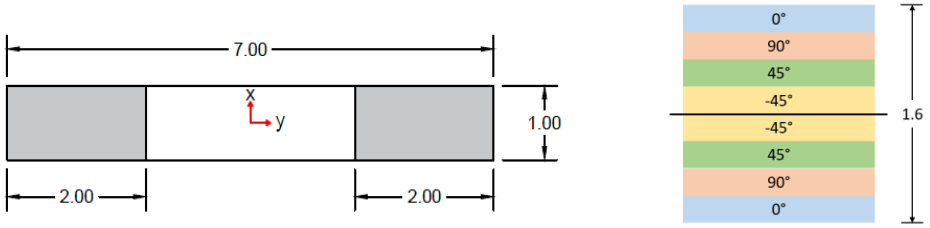

(a) (b)

Figure 3.14. Tension coupon specimen: (a) dimensions, and (b) fiber orientation layup

Table 3.4 shows all simulations that were performed, all of which terminated normally. In the first two sets, the stochastic variation of all deformation properties was varied by a 10% and 20% uniform random distribution, respectively. In the second two sets of simulations, the Tsai-Wu failure criterion was added to access the influence in simulations with failure.

Table 3.4. Coupon verification cases

	Stochastic variables varied per case	Cases	Number of simulations per case	Total simulations
Cross-ply tension all (10% variation)	(4/4)	1	10	10
Cross-ply tension all (20% variation)	(4/4)	1	10	10
Cross-ply tension with Tsai-Wu failure (10% variation)	(4/4)	1	10	10
Cross-ply tension with Tsai-Wu failure (20% variation)	(4/4)	1	10	10
			Total	40

Figure 3.15 shows the measured force over time in the cases without failure and for a variation of 10%. Very little deviation from the baseline can be observed. Even for a uniform random distribution of 20%, the results looked similar than in the shown graph. The reason for the consistent results seems to be an averaging effect of the deformation properties similar to many springs in a series and parallel arrangement as all elements are loaded relatively uniform.

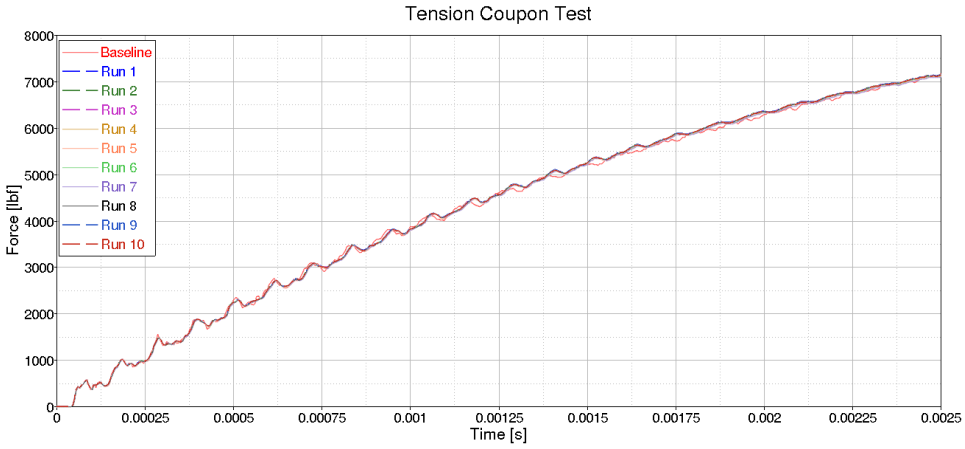

Figure 3.15. Coupon simulation results with 10% stochastic variation

When failure is considered, however, the results show significant differences to the baseline and to each other, as figure 3.16 shows. If a comparably “weak” element is located in a region with high stresses, it will fail earlier and therefore cause the whole coupon to fail earlier. As the geometric distribution of the scale factors is random, in some cases the coupon will fail at a higher or lower force.

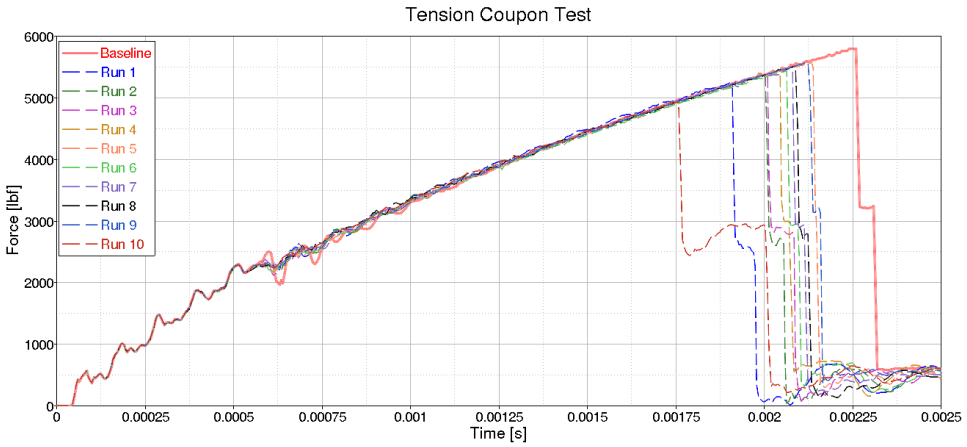

Figure 3.16. Coupon simulation results with 10% stochastic variation and Tsai-Wu failure

3.3.2 Ballistic Impact Simulation

The influence of a variation of the elastic properties on low-velocity ballistic impact simulations without failure was studied on the impact test LVG1071. All deformation properties available in the *DEFINE_STOCHASTIC_VARIATION_MAT213 option were varied with a uniform random distribution of ±10%. Since these simulations were conducted to verify that the stochastic option does not cause issues in large models, the physical significance of the distribution was not considered.

Figure 3.17 shows the results for the baseline (deterministic) simulation (solid red line), the physical test (solid black line), and 10 simulations with the stochastic variation of the deformation properties (dashed lines). The displacement of the plate shows a variation in the 10 runs that ranges from very similar (Run 6) to the baseline simulation, to significant differences (Run 7).

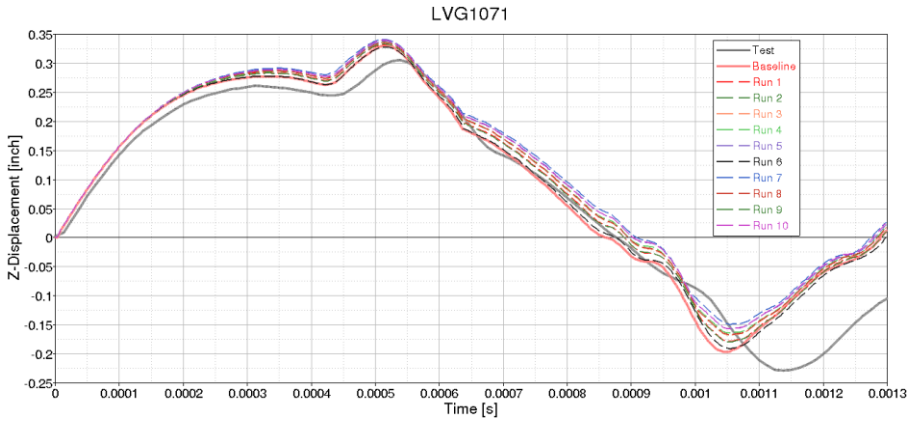

Figure 3.17. Z-Displacement at the center of the plate in ballistic impact simulations with stochastic variation of deformation properties

4. CONCLUDING REMARKS

This study worked on three tasks: (1) development of a composite FE model, (2) development of a stochastic computational framework of multiscale composite analysis, and (3) comparison of deterministic to probabilistic simulations.

First, a composite FE model was developed for stable and accurate impact simulations. The convergence of the modeling and numerical parameters, such as the number of elements through a plate thickness, an aspect ratio of elements, and hourglass control, was studied. Also, the modeling techniques of boundary condition and delamination were developed.

Secondly, the stochastic computational framework of multiscale composite analysis was developed. The stochastic microscale analysis using the MAC/GMC was conducted to estimate the mean and distribution of composite properties, which were the inputs of the macroscale analysis. Then, the stochastic macroscale analysis for impact simulations using LS-DYNA was conducted to estimate the probability of penetration for different impact velocities on the composite plate.

Lastly, the results of deterministic and probabilistic simulations were compared. The stochastic function was implemented into *MAT_213 for the stochastic analysis of impact simulation. The stochastic function of *MAT_213 was verified in single-element level and component level studies. Clearly, the results show that the material variation leads to a noticeable response variation.

In addition, the Generalized Tabulated Failure Model in *MAT_213 was verified by checking the history of the stress-state variables, such as the angle and radius, in single-element and impact simulations.

5. REFERENCES

[1] J.O. Hallquist, “LS-DYNA - Keyword User’s Manual - Volume II - Material Models,” Livermore Software Technology Corporation, 2015.

[2] S.H. Marzi, “Ein ratenabhängiges, elasto-plastisches Kohäsivzonenmodell zur Berechnung struktureller Klebverbindungen unter Crashbeanspruchung,” Stuttgart: Fraunhofer-Verlag, 2010.

[3] M. Juntti, L.E. Asp, and R. Olsson, “Assessment of Evaluation Methods for the Mixed-Mode Bending Test,” Journal of Composites, Technology and Research, 1999, 21(1):37-48.

[4] P.W. Harper and S.R. Hallett, “Cohesive Zone Length in Numerical Simulations of Composite Delamination,” Engineering Fracture Mechanics, 2008, 75(16):4774-4792.

[5] S. Matsuda, M. Hojo, and S. Ochiai, “Mesoscopic Fracture Mechanism of Mode II Delamination Fatigue Crack Propagation in Interlayer-Toughened CFRP,” JSME International Journal Series A Solid Mechanics and Material Engineering, 1997, 40(4):423-429.

[6] S. Liu and F.K. Chang, “Matrix Cracking Effect on Delamination Growth in Composite Laminates Induced by a Spherical Indenter,” Journal of Composite Materials, 1994, 28(10):940-977.

[7] B.D. Davidson and F.O. Sediles, “Mixed-Mode I-II-III Delamination Toughness Determination via a Shear-Torsion-Bending Test,” Composites Part A: Applied Science and Manufacturing, 2011, 42(6):589-603.

[8] I. Chou, T. Inutake, and K. Namba, “Correlation of Damage Resistance under Low Velocity Impact and Mode II Delamination Resistance in CFRP Laminates,” Advanced Composite Materials, 1999, 8(2):167-176.

[9] K. Kageyama, I. Kimpara, I. Ohsawa, M. Hojo, and S. Kabashima, “Mode I and Mode II Delamination Growth of Interlayer Toughened Carbon/Epoxy (T800H/3900-2) Composite System,” Composite Materials: Fatigue and Fracture: Fifth Volume, STP1230-EB, Martin, R., Ed., ASTM International, West Conshohocken, PA, 1995, pp. 19-37.

[10] P. Nuggehalli Nandakumar, “Rate Sensitivity of the Interlaminar Fracture Toughness of Laminated Composites,” Master’s Thesis, Wichita State University, 2010.

[11] J. Rhymer, H. Kim, and D. Roach, “The Damage Resistance of Quasi-Isotropic Carbon/Epoxy Composite Tape Laminates Impacted by High Velocity Ice,” Composites Part A: Applied Science and Manufacturing, 2012, 43(7):1134-1144.

[12] B. Wade and P. Feraboli, “Crushing Behavior of Laminated Composite Structural Elements: Experiment and LS-DYNA Simulation,” Technical Report, DOT/FAA/TC-15/25, December 2016.

[13] S. Dong, K. Carney, A. Sheldon, and L. Graening, “Parametric Optimization of CAE Material Models for Carbon-Fiber-Reinforced Polymer (CFRP) Composites,” NAFEMS World Congress, June 2017.

[14] J.P. Johnston, “Stochastic Multiscale Modeling and Statistical Characterization of Complex Polymer Matrix Composites,” PhD Dissertation, Arizona State University, 2016.

[15] G. Nilakantan, “Modeling the Impact of Flexible Textile Composites Trough Multiscale and Probabilistic Methods,” PhD Dissertation, University of Delaware, 2010.

[16] T.M. Ricks, T.E. Lacy, B.A. Bednarcyk, and S.M. Arnold, “A Multiscale Modeling Methodology for Metal Matrix Composites Including Fiber Strength Stochastics,” 53rd AIAA/ASME/ASCE/AHS/ASC Structures, Structural Dynamics and Materials Conference, April 2012.
[17] R.K. Goldberg, P.J. Bonacuse, and S.K. Mital, “Investigation of Effects of Material Architecture on the Elastic Response of a Woven Ceramic Matrix Composite,” Technical Report, NASA/TM-2012-217269, 2012
[18] S.M. Arnold, P.L.N. Murthy, B.A. Bednarcyk, E.J. Pineda, and S.K. Mital, “Micromechanics-Based Fatigue Life Pre-diction of Composites,” 58th AIAA/ASCE/AHS/ASC Structures, Structural Dynamics, and Materials Conference, 2017.
[19] S.M. Arnold, B.A. Bednarcyk, T.E. Wilt, and D. Trowbridge, “Micromechanics Analysis Code with Generalized Method of Cells (MAC/GMC) - User Guide: Version 3.0,” NASA Glenn Research Center, 1999.
[20] N. Stander, W. Roux, A. Basudhar, T. Eggleston, T. Goel, and K. Craig, “LS-OPT User’s Manual,” Livermore Software Technology Corporation, 2015.
[21] R.K. Goldberg, K.S. Carney, P. DuBois, C. Hoffarth, B. Khaled, L. Shyamsunder, S. Rajan, and G. Blankenhorn, “Incorporation of Failure into an Orthotropic Three-Dimensional Model with Tabulated Input Suitable for Use in Composite Impact Problems,” Technical Report, NASA/TM-2017-219492 , 2017.

APPENDIX A. GENERALIZED TABULATED FAILURE MODEL

In most available failure models for composites, the shape of the failure surface in stress space is described as a mathematical function, with the disadvantage of therefore prescribing the general shape of this surface. The Generalized Tabulated Failure Model implemented in *MAT_213, however, allows for the input of tabulated curves to describe the failure surface. Therefore, the new failure model allows for a more precise definition of said failure surface. This section will investigate some of the characteristics of the new failure model in simple single-element cases and compare the important variables to the expected values in such loading conditions. A detailed description of the theory of the Generalized Tabulated Failure Model is provided by Goldberg et al. [21].

A.1. IN-PLANE FAILURE MODEL

A point on the in-plane failure surface is described in the σ_{11}-σ_{22} plane using the independent variables, such as angle (θ) and the ratio of the shear stress to the shear failure stress. The magnitude of the failure surface point along these lines is defined by the dependent variable *r* (radius). Both the angle and the radius are calculated as

$$\theta = cos^{-1}\left(\frac{\sigma_{11}}{\sqrt{\sigma_{11}^2+\sigma_{22}^2}}\right) \theta_{act} = -\theta \; if \; \sigma_{22} \leq 0, \text{ and} \tag{A.1}$$

$$r = \sqrt{\sigma_{11}^2 + \sigma_{22}^2 + 2\sigma_{12}^2}\,. \tag{A.2}$$

Figure A.1 shows an example of what a failure surface defined by the Generalized Tabulated Failure Criterion might look like. The red lines on the surface represent the tabulated input curves that function as the input to the model. All other points on the surface are interpolated between these curves. The shown failure surface functioned as the input to the single-element verification cases described in the following paragraphs. For the in-plane failure model, tension and compression in 1- and 2-directions, as well as shear in 12-direction, were evaluated.

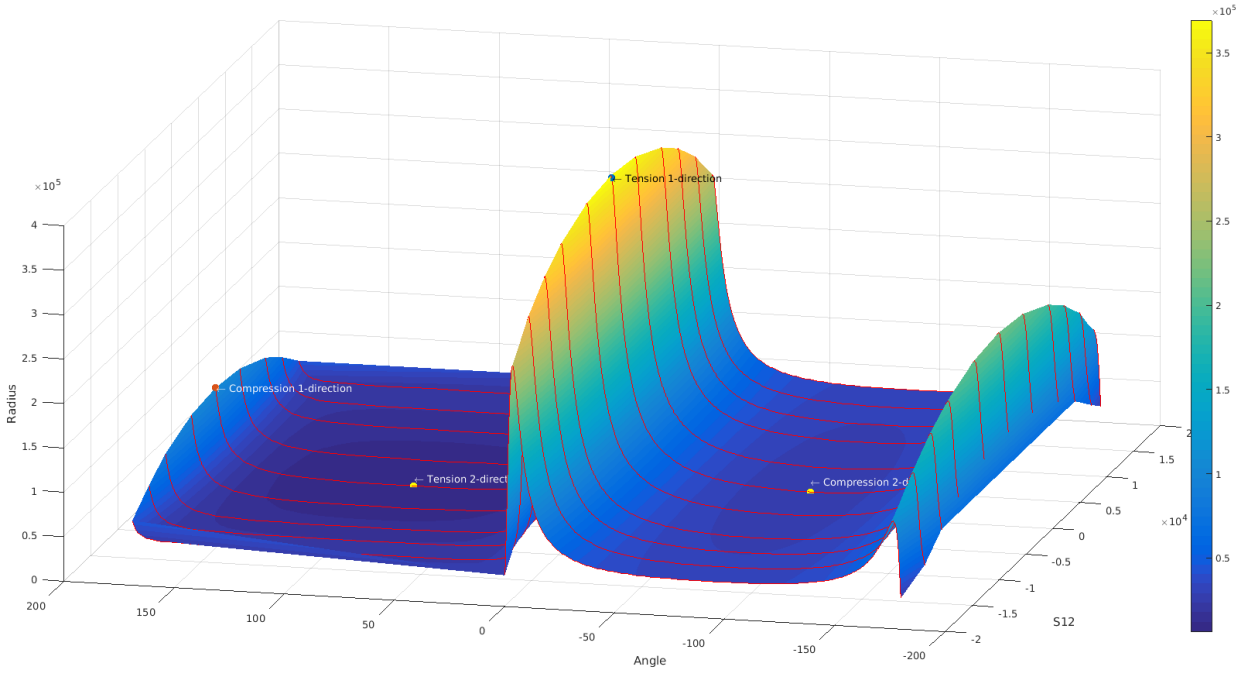

Figure A.1. Example of in-plane failure surface

A.1.1. Tension 1-Direction

Since the stresses in 2-direction and shear in 12-direction are zero, if the element is loaded in tension in 1-direction, the calculated angle is zero. The radius throughout the simulation is expected to correlate with the stress in 1-direction as the following calculations show:

$$\theta = cos^{-1}\left(\frac{\sigma_{11}}{\sqrt{\sigma_{11}^2 + \sigma_{22}^2}}\right) = cos^{-1}\left(\frac{\sigma_{11}}{\sqrt{\sigma_{11}^2 + 0}}\right) = cos^{-1}(1) = 0°$$

$$r = \sqrt{\sigma_{11}^2 + \sigma_{22}^2 + 2\sigma_{12}^2} = \sqrt{\sigma_{11}^2} = \sigma_{11}$$

Figure A.2 shows the angle and radius throughout the simulation with the calculated values corresponding to the expected ones.

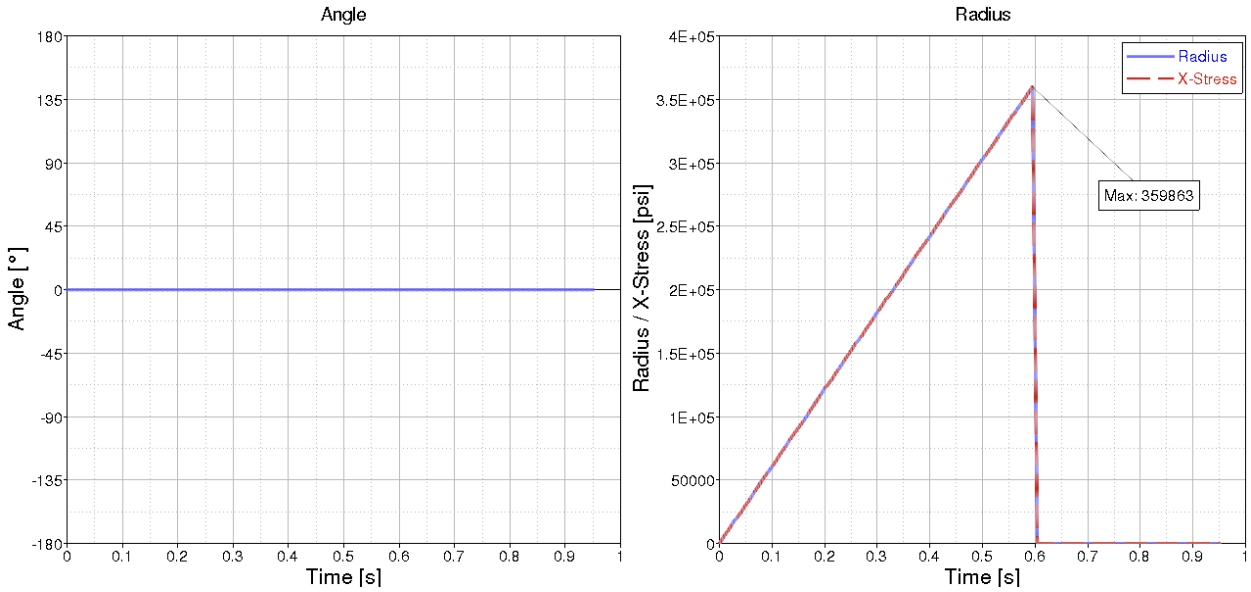

Figure A.2. Angle and radius in tension in 1-direction: (a) angle, and (b) radius

A.1.2. Tension 2-Direction

With both stresses in 1-direction and shear in 12-direction being zero, the angle in tension loading in 2-direction should be 90° and the radius should correlate with the computed stress in 2-direction:

$$\theta = cos^{-1}\left(\frac{\sigma_{11}}{\sqrt{\sigma_{11}^2 + \sigma_{22}^2}}\right) = cos^{-1}\left(\frac{0}{\sqrt{0 + \sigma_{22}^2}}\right) = cos^{-1}(0) = 90°$$

$$r = \sqrt{\sigma_{11}^2 + \sigma_{22}^2 + 2\sigma_{12}^2} = \sqrt{\sigma_{22}^2} = \sigma_{22}$$

Figure A.3 shows the computed values for the angle and radius throughout the simulation. Both angle and radius match the expected values.

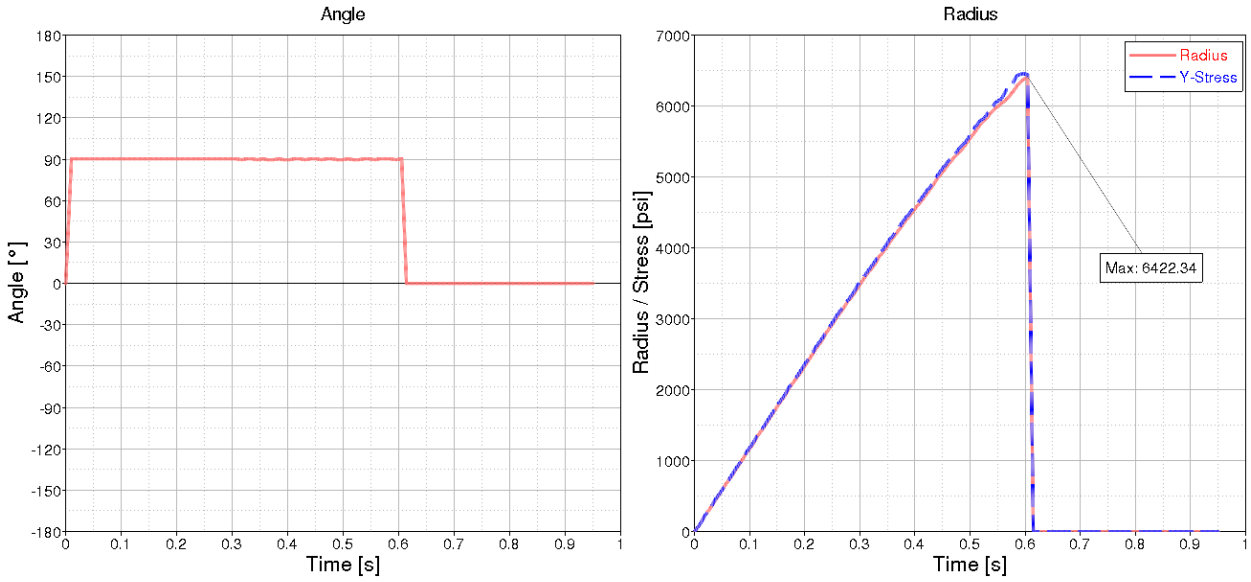

(a) (b)

Figure A.3. Angle and radius in tension in 2-direction: (a) angle, and (b) radius

A.1.3. Compression 1-Direction

For compression in 1-direction, the computed values for the angle are 180° and the radius are expected to correspond to the absolute values of the stress in 1-direction.

$$\theta = cos^{-1}\left(\frac{\sigma_{11}}{\sqrt{\sigma_{11}^2 + \sigma_{22}^2}}\right) = cos^{-1}\left(\frac{-\sigma_{11}}{\sqrt{-\sigma_{11}^2 + 0}}\right) = cos^{-1}(-1) = 180°$$

$$r = \sqrt{\sigma_{11}^2 + \sigma_{22}^2 + 2\sigma_{12}^2} = \sqrt{-\sigma_{11}^2} = |\sigma_{11}|$$

Figure A.4 shows the results for the angle and radius throughout the simulation, which match the expected values.

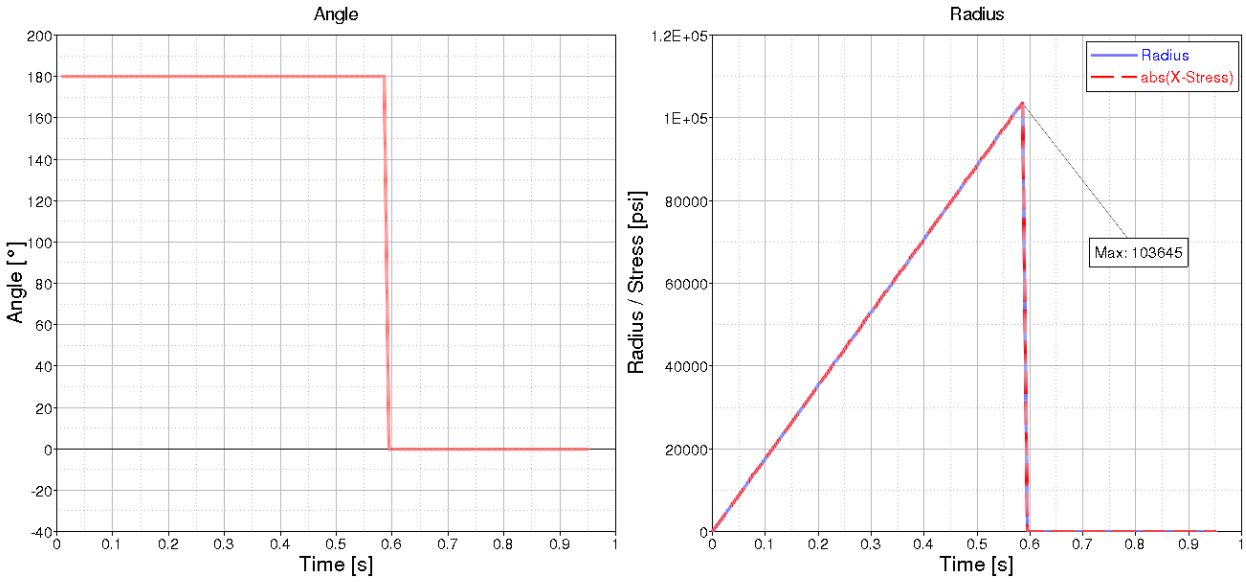

(a) (b)

Figure A.4. Angle and radius in compression in 1-direction: (a) angle, and (b) radius

A.1.4. Compression 2-Direction

For compression in 2-direction, the computed angle is 90°. However, as the stress in 2-direction is negative, the sign of the angle is changed to differentiate between tension and compression in 2-direction. The computed radius should correspond to the stress in 2-direction.

$$\theta = cos^{-1}\left(\frac{\sigma_{11}}{\sqrt{\sigma_{11}^2 + \sigma_{22}^2}}\right) = cos^{-1}\left(\frac{0}{\sqrt{0 + \sigma_{22}^2}}\right) = cos^{-1}(0) = 90°$$

$$\theta_{act} = -\theta \; if \; \sigma_{22-mod} \leq 0$$

$$\theta = -90°$$

$$r = \sqrt{\sigma_{11}^2 + \sigma_{22}^2 + 2\sigma_{12}^2} = \sqrt{-\sigma_{22}^2} = |\sigma_{22}|$$

Figure A.5 shows that both angle and radius match the expected values.

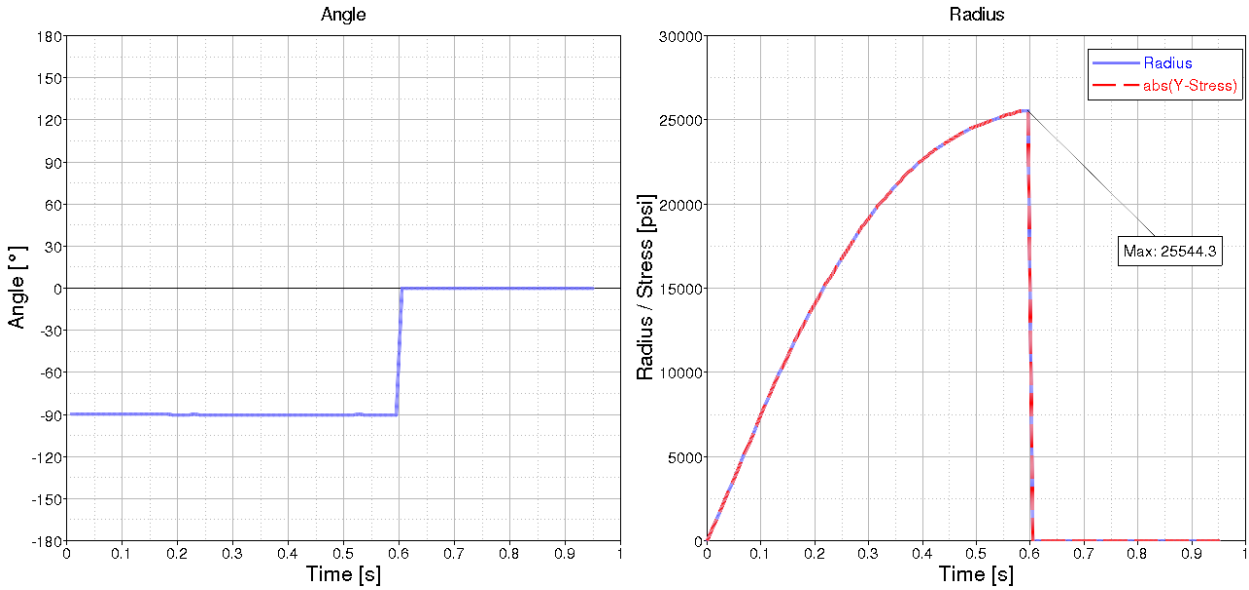

(a) (b)

Figure A.5. Angle and radius in compression in 2-direction: (a) angle, and (b) radius

A.1.5. 12-Shear

In pure in-plane shear, both normal in-plane stress components are zero and therefore the computed angle is 90°. The radius for shear in 12-direction is expected to correlate to $\sqrt{2}\sigma_{12}$.

$$\theta = cos^{-1}\left(\frac{\sigma_{11}}{\sqrt{\sigma_{11}^2 + \sigma_{22}^2}}\right) = cos^{-1}\left(\frac{0}{\sqrt{0+0}}\right) = cos^{-1}(0) = 90°$$

$$r = \sqrt{\sigma_{11}^2 + \sigma_{22}^2 + 2\sigma_{12}^2} = \sqrt{2\sigma_{12}^2} = \sqrt{2}\sigma_{12}$$

Figure A.6 shows the results for the 12-shear single-element case. The angle matches the expected value of 90°, the radius (blue curve) matches the 12-shear stress (green curve) multiplied by $\sqrt{2}$ (red curve).

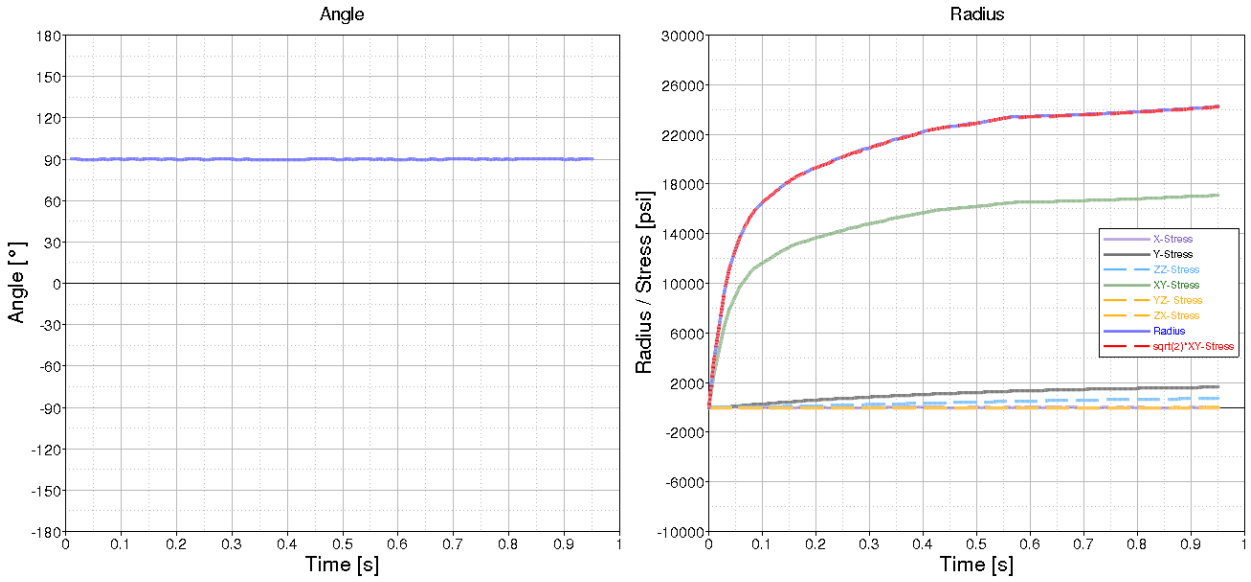

Figure A.6. Angle and radius in 12-shear: (a) angle, and (b) radius

A.2. OUT-OF-PLANE FAILURE MODEL

A point on the out-of-plane failure surface is described in the σ_{13}-σ_{23} plane using the independent variables θ (angle) and the ratio of the out-of-plane normal stress to the out-of-plane failure stress. The magnitude of the failure surface point along these lines is defined by the dependent variable r (radius). The following equations show how both the angle and the radius are calculated in the out-of-plane cases:

$$\theta = cos^{-1}\left(\frac{\sigma_{13}}{\sqrt{\sigma_{13}^2+\sigma_{23}^2}}\right) \theta_{act} = -\theta \; if \; \sigma_{23} \leq 0 \text{ , and} \tag{A.3}$$

$$r = \sqrt{\sigma_{33}^2 + 2\sigma_{13}^2 + 2\sigma_{23}^2} \text{ .} \tag{A.4}$$

Figure A.7 shows an example of the out-of-plane failure surface that was used in the subsequent single-element simulations.

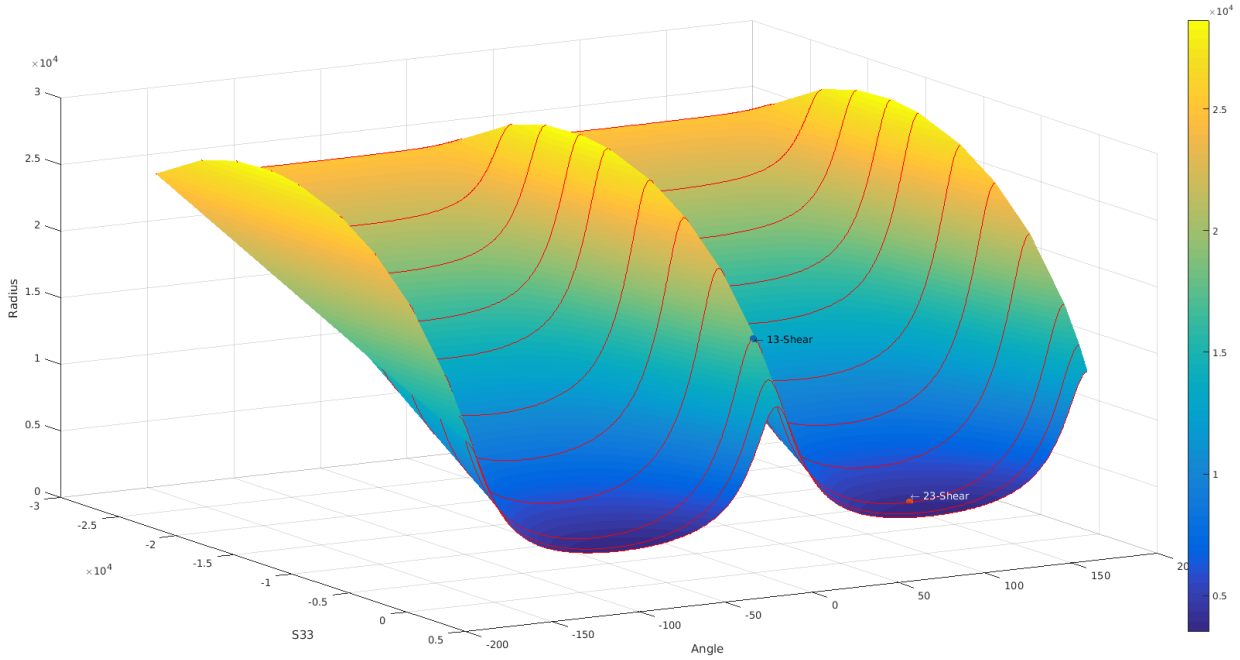

Figure A.7. Example of out-of-plane failure surface

A.2.1. 3-Direction Tension

With the out-of-plane normal stress as the only non-zero stress component, the equation to calculate the angle ends up with a fraction that divides two values that are both close to zero. Due to the numerical noise, the computed values for the angle do not stay constant at one value throughout the simulation as shown in figure A.8(a). The radius in figure A.8(b), however, matches the expected value and correlates perfectly with the through-thickness normal stress.

$$\theta = cos^{-1}\left(\frac{\sigma_{13}}{\sqrt{\sigma_{13}^2 + \sigma_{23}^2}}\right) = cos^{-1}\left(\frac{0}{\sqrt{0+0}}\right) = cos^{-1}(0) = 90°$$

$$r = \sqrt{\sigma_{33}^2 + 2\sigma_{13}^2 + 2\sigma_{23}^2} = \sqrt{\sigma_{33}^2} = \sigma_{33}$$

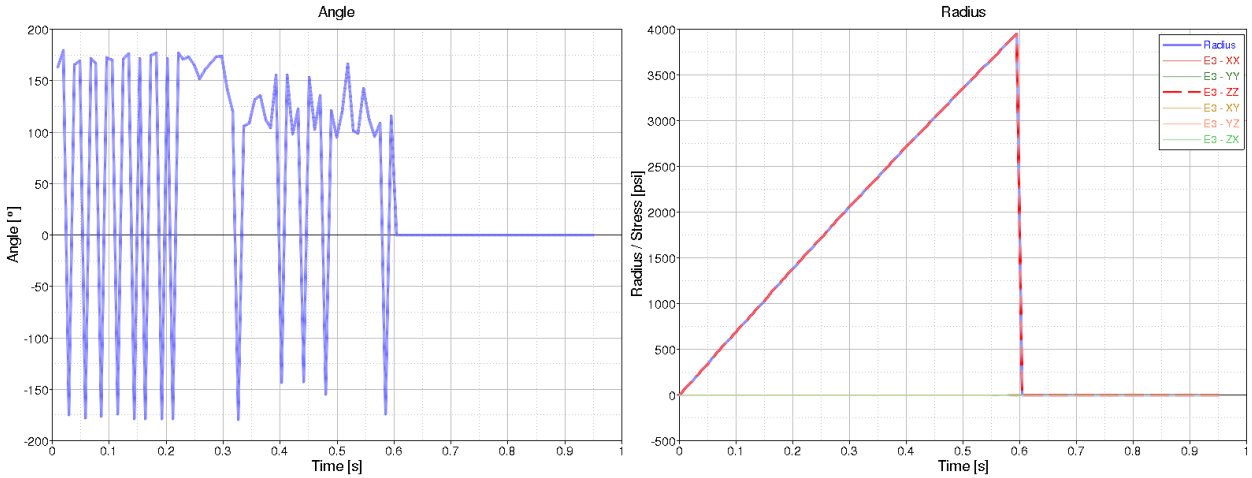

(a) (b)

Figure A.8. Angle and radius in tension in 3-direction: (a) angle, and (b) radius

A.2.2. 3-Direction Compression

Compression in 3-direction yields similar results as the tension case with the angle oscillating as shown in figure A.9(a). The radius in figure A.9(b) correlates perfectly with the expected value and matches the through-thickness normal stress.

$$\theta = cos^{-1}\left(\frac{\sigma_{13}}{\sqrt{\sigma_{13}^2 + \sigma_{23}^2}}\right) = cos^{-1}\left(\frac{0}{\sqrt{0+0}}\right) = cos^{-1}(0) = 90°$$

$$r = \sqrt{\sigma_{33}^2 + 2\sigma_{13}^2 + 2\sigma_{23}^2} = \sqrt{\sigma_{33}^2} = |\sigma_{33}|$$

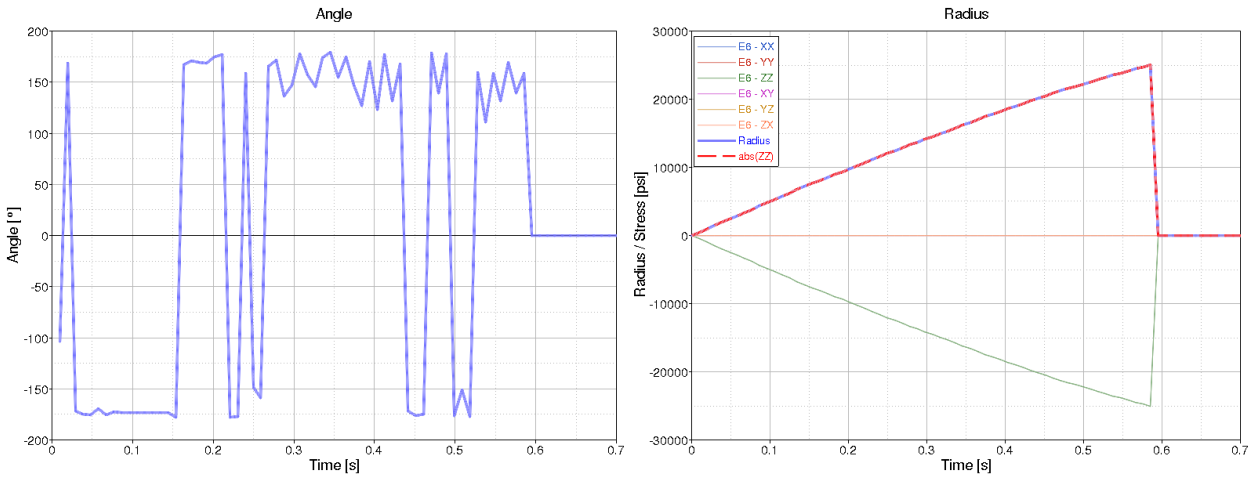

(a) (b)

Figure A.9. Angle and radius in compression in 3-direction: (a) angle, and (b) radius

A.2.3. 23-Shear

In the out-of-plane shear case in 23-direction, the calculated and computed angle values match, as do the radius values, which is shown in figure A.10.

$$\theta = cos^{-1}\left(\frac{\sigma_{13}}{\sqrt{\sigma_{13}^2 + \sigma_{23}^2}}\right) = cos^{-1}\left(\frac{0}{\sqrt{0 + \sigma_{23}^2}}\right) = cos^{-1}(0) = 90°$$

$$r = \sqrt{\sigma_{33}^2 + 2\sigma_{13}^2 + 2\sigma_{23}^2} = \sqrt{0 + 0 + 2\sigma_{23}^2} = \sqrt{2}\sigma_{23}$$

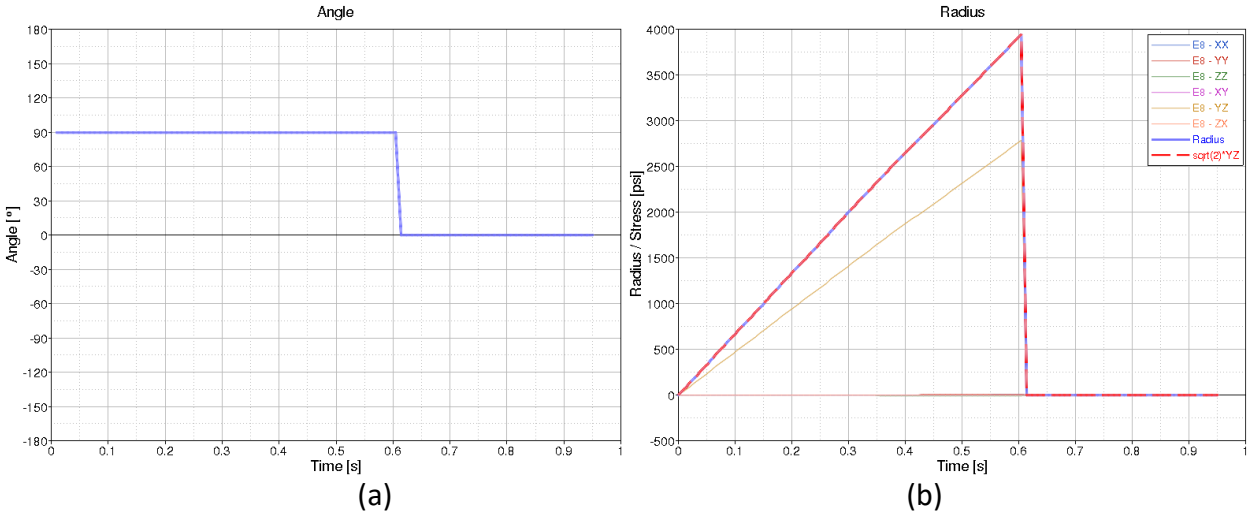

(a) (b)

Figure A.10. Angle and radius in 23-shear: (a) angle, and (b) radius

A.2.4. 31-Shear

In the second out-of-plane shear single-element simulation, the computed angle is expected to be zero and the radius to correlate with $\sqrt{2}\sigma_{13}$. Figure A.11 shows that both the angle and radius match their expected values.

$$\theta = cos^{-1}\left(\frac{\sigma_{13}}{\sqrt{\sigma_{13}^2 + \sigma_{23}^2}}\right) = cos^{-1}\left(\frac{\sigma_{13}}{\sqrt{\sigma_{13}^2 + 0}}\right) = cos^{-1}(1) = 0°$$

$$r = \sqrt{\sigma_{33}^2 + 2\sigma_{13}^2 + 2\sigma_{23}^2} = \sqrt{0 + 2\sigma_{13}^2 + 0} = \sqrt{2}\sigma_{13}$$

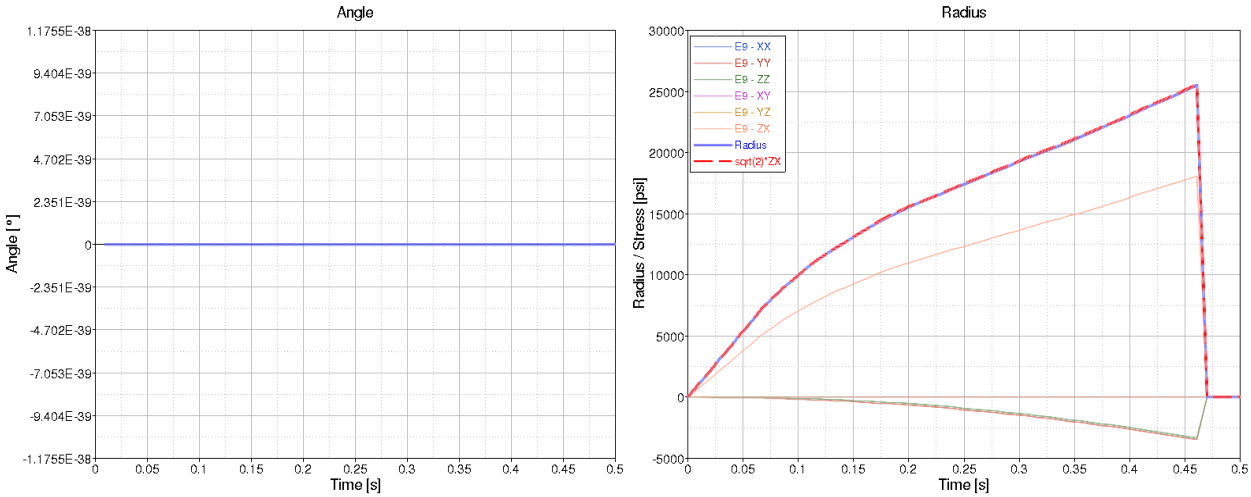

(a) (b)

Figure A.11. Angle and radius in 31-shear: (a) angle, and (b) radius

A.3. BALLISTIC IMPACT SIMULATION

In addition to the single-element simulations, two ballistic impacts were simulated to analyze the output with respect to the Generalized Tabulated Failure Model. The projectile impact velocities chosen were 155 ft/sec (LVG1071) and 237 ft/sec (LVG1064). In the physical test of LVG1071, the projectile did not penetrate the panel and no damage was visible. In the test LVG1064, the projectile did not penetrate the panel as well. However, some splitting of the 0 degree fibers and some minimal fiber fracture was observed.

For a better understanding of the parameters that are used to define failure in the Generalized Tabulated Failure Model, the in- and out-of-plane angle, as well as the in-plane shear (12) and out-of-plane normal stress (33), were plotted over time for both impact velocities.

A.3.1. LVG1071

Figure A.12 shows the in-plane angle for four specific elements in the LVG1071 case. The red curve, for example, represents the element in the center of the plate that is directly impacted by the projectile. A negative value between -140° and -170° in the first 0.2 msec of the simulation is an indication of biaxial compression in 1- and 2-directions as the following approximation shows:

$$\sigma_{12} = 0, \sigma_{11} = 4\sigma_{22} < 0:$$

$$\theta = cos^{-1}\left(\frac{\sigma_{11}}{\sqrt{\sigma_{11}^2 + \sigma_{22}^2}}\right) \approx cos^{-1}\left(\frac{4\sigma_{22}}{\sqrt{(4\sigma_{22})^2 + \sigma_{22}^2}}\right)$$

$$= cos^{-1}\left(\frac{-4}{\sqrt{17}}\right) \approx cos^{-1}(-0.97) \approx 166°$$

$$\theta_{act} = -\theta \; if \; \sigma_{22} \leq 0 \rightarrow \theta = -166°$$

As the plate experiences a bending during the impact, this can explain the compressive in-plane stresses on the impacted side of the plate.

When looking at the opposite side of the plate (blue curve) in figure A.12, the values between 0°and 5° indicate a biaxial tension in-plane dominated by 1-directional tension as the following approximation shows:

$$\sigma_{12} = 0, \sigma_{11} = 15\sigma_{22} > 0:$$

$$\theta = cos^{-1}\left(\frac{\sigma_{11}}{\sqrt{\sigma_{11}^2 + \sigma_{22}^2}}\right) \approx cos^{-1}\left(\frac{15\sigma_{22}}{\sqrt{(15\sigma_{22})^2 + \sigma_{22}^2}}\right)$$

$$= cos^{-1}\left(\frac{15}{\sqrt{(15)^2 + 1}}\right) \approx cos^{-1}(0.998) \approx 3.6°$$

This tension on the opposite side of the plate again indicates a bending of the plate and therefore seems reasonable.

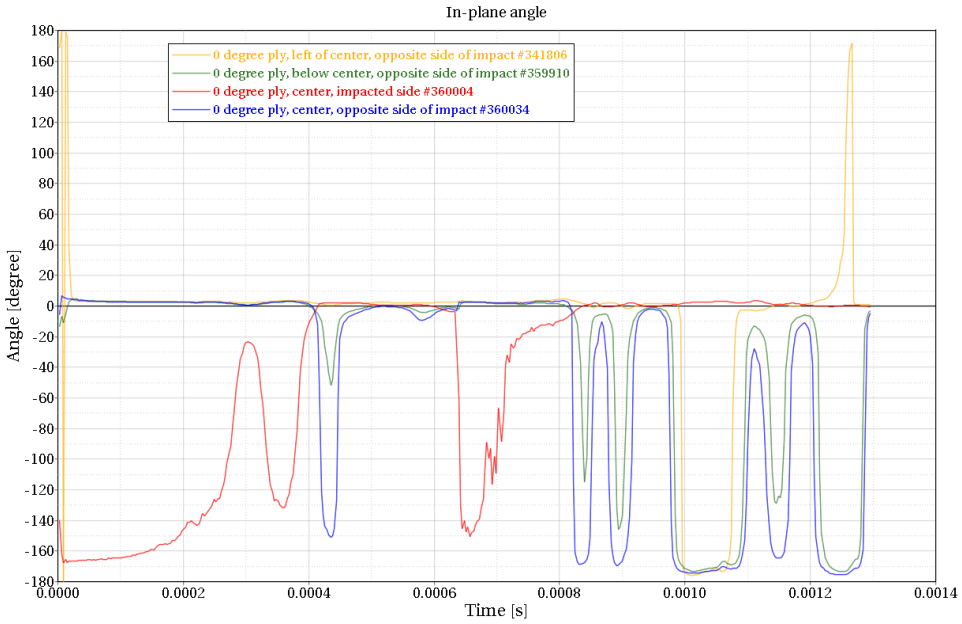

Figure A.12. In-plane angle of specific elements in LVG1071

In addition to the in-plane angle, figure A.13 shows the in-plane shear stress in the top graph and the plate displacement during the same time interval. The shear stresses in the initial phase of the simulation range from around -1000 to +1000 psi.

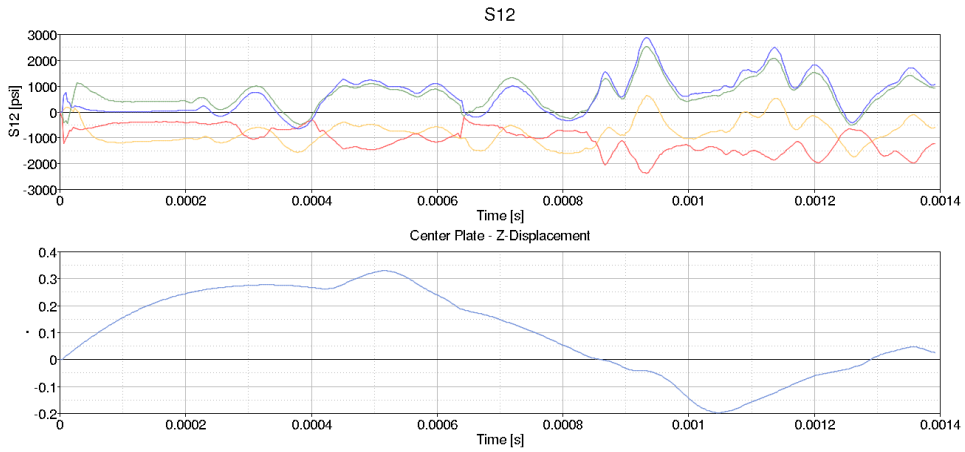

Figure A.13. In-plane shear stress of specific elements and center plate displacement in LVG1071

Figure A.14 shows the out-of-plane angle for four specific elements in the LVG1071 case.

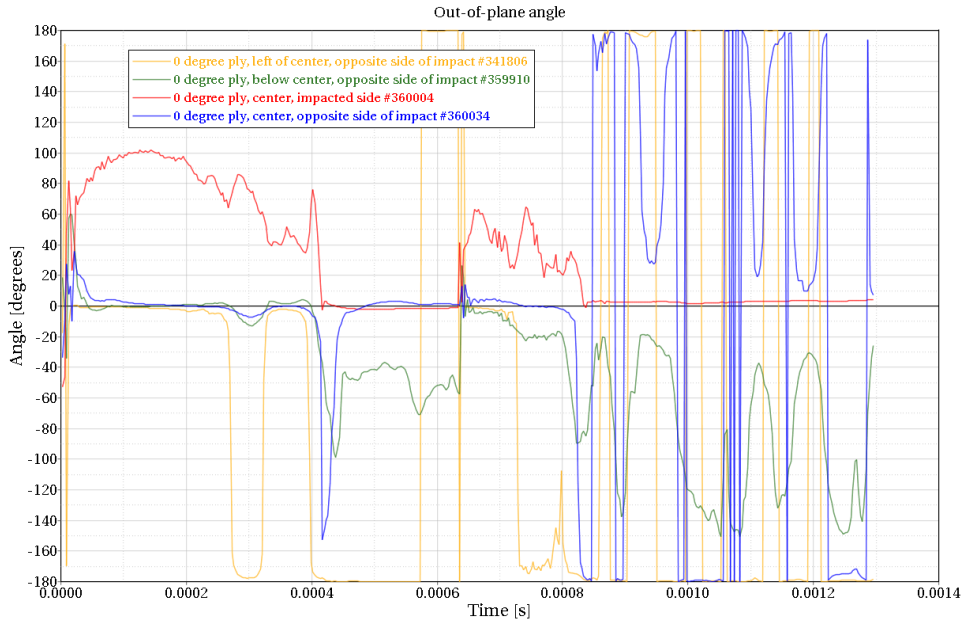

Figure A.14. Out-of-plane angle of specific elements in LVG1071

Figure 15 shows the out-of-plane normal stress (top) and the plate displacement (bottom). The red curve shows the stress at the center element of the impacted side

with a sharp peak right at the beginning of the simulation when the projectile first contacts the panel. The thickness stress then levels at around -10,000 psi while the plate deforms. Between 0.4 and 0.65 msec, the projectile loses contact to the plate as a deformation wave travels back to the center of the plate. As a result, the thickness stresses drop to a value close to zero before the projectile comes in contact with the plate again.

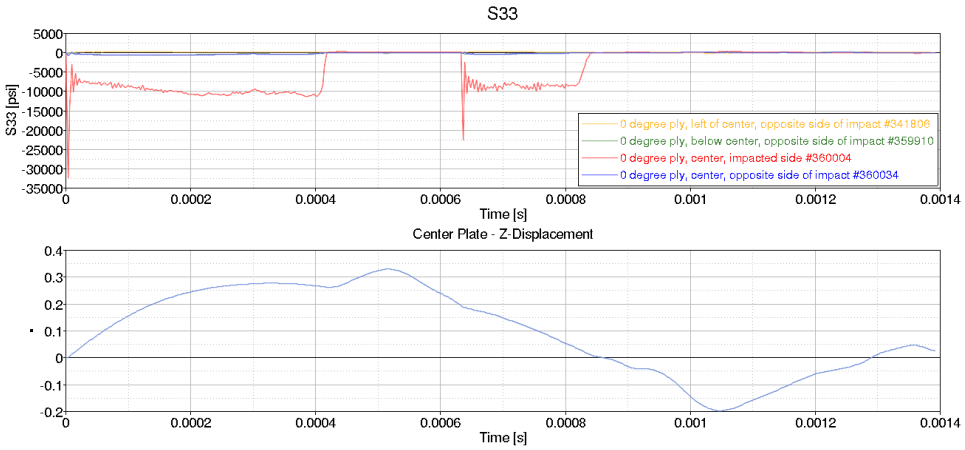

Figure A.15. Out-of-plane normal stress of specific elements and center plate displacement in LVG1071

Figure A.16 shows a zoomed version of the thickness stress vs. time plot.

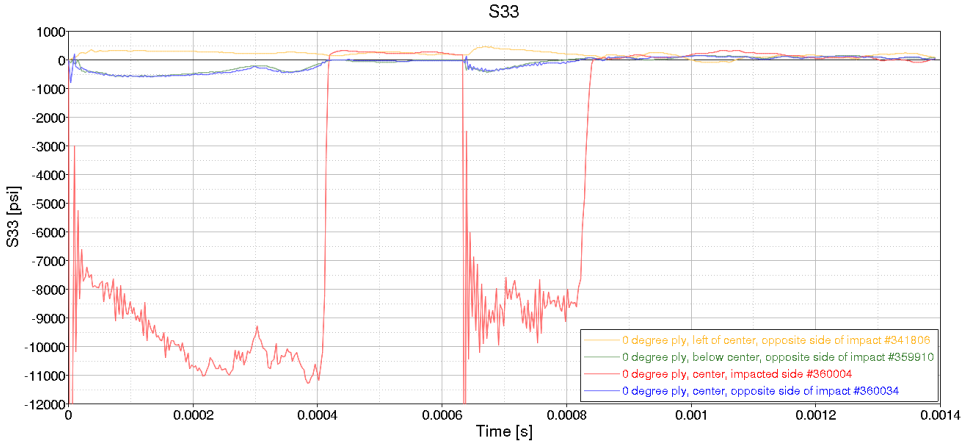

Figure A.16. Out-of-plane normal stress of specific elements in LVG1071 (zoomed)

A.3.2 LVG1064

Figure A.17 shows the in-plane angle for four specific elements in the LVG1064 case, which featured a higher impact velocity than the previously shown LVG1071 test. The

following plots show the in-plane shear (figure A.18), out-of-plane angle (figure A.19) and the out-of-plane normal stress (figures A.20 and A.21).

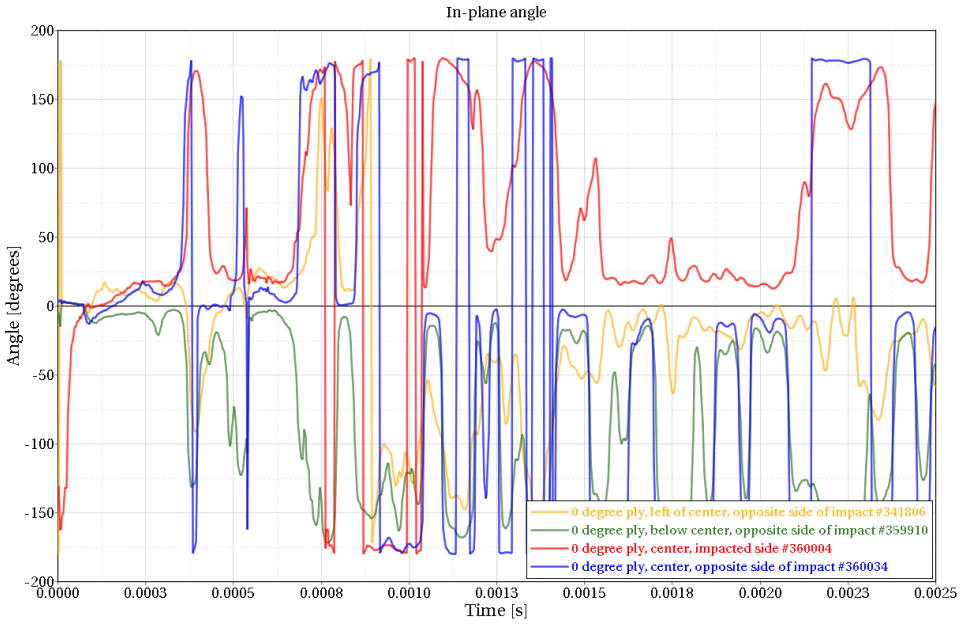

Figure A.17. In-plane angle of specific elements in LVG1064

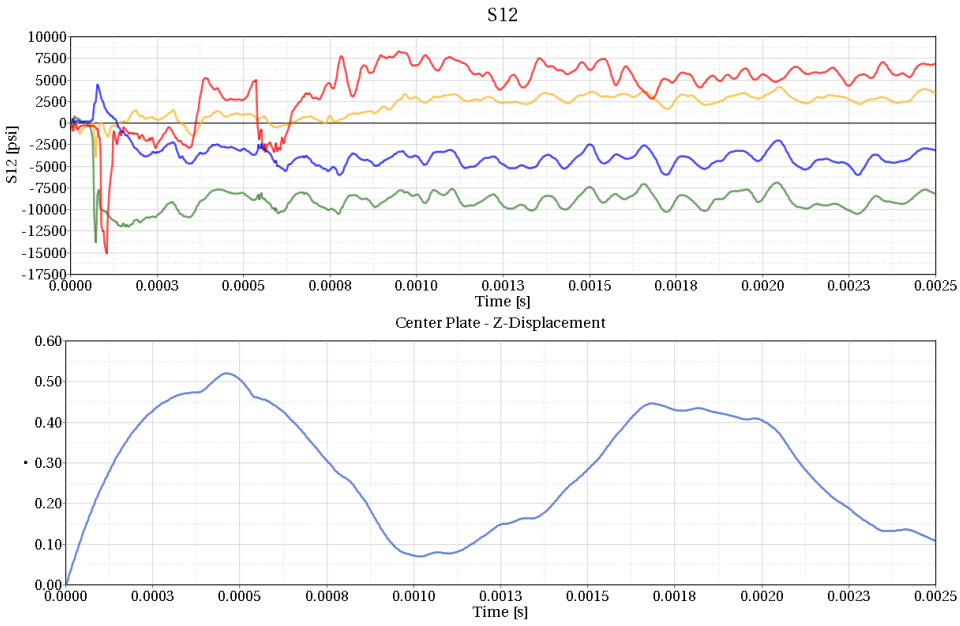

Figure A.18. In-plane shear stress of specific elements and center plate displacement in LVG1064

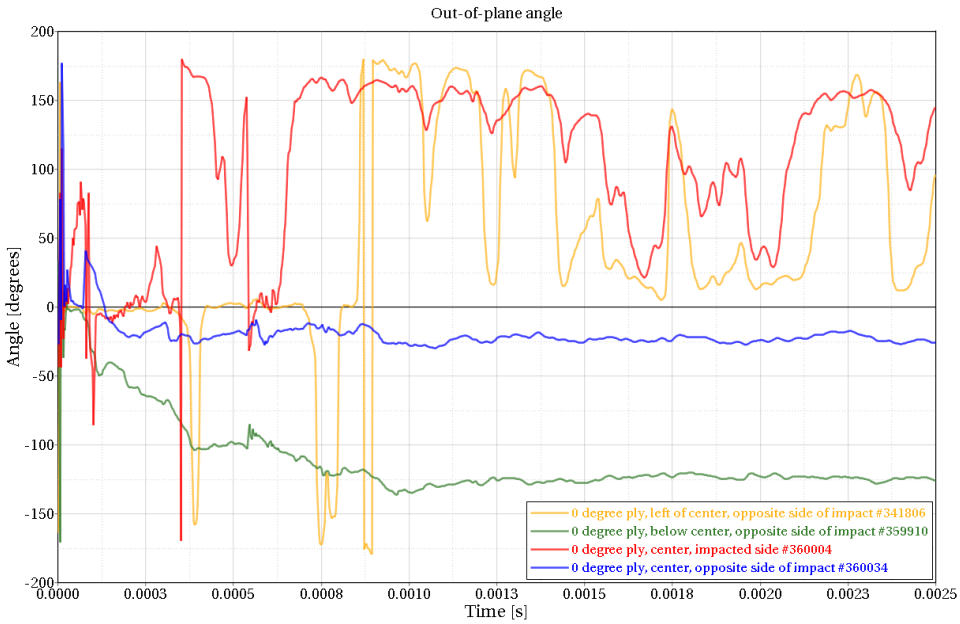

Figure A.19. Out-of-plane angle of specific elements in LVG1064

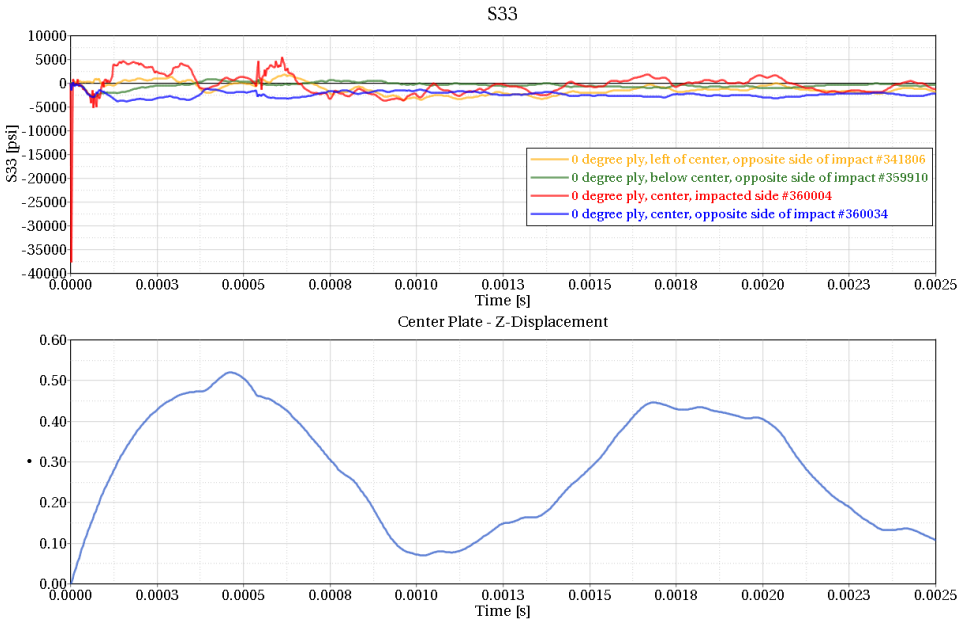

Figure A.20. Out-of-plane normal stress of specific elements and center plate displacement in LVG1064

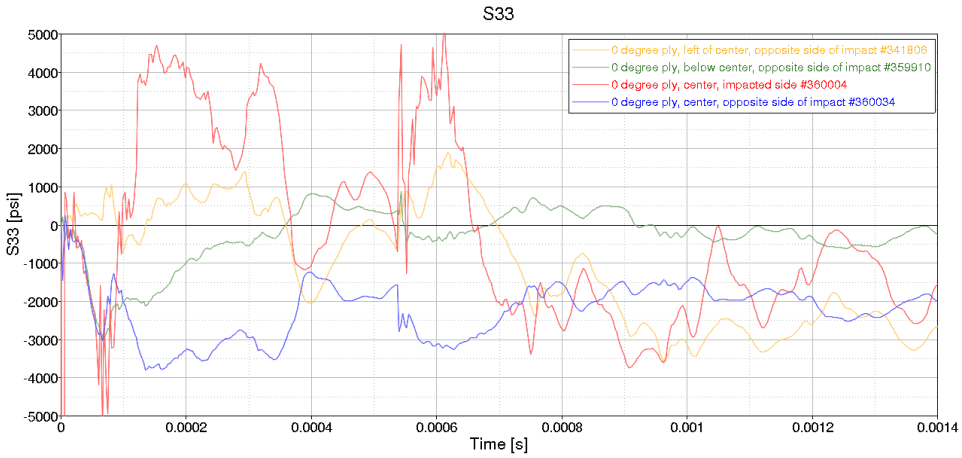

Figure A.21. Out-of-plane normal stress of specific elements in LVG1064 (zoomed)

APPENDIX B. USED *MAT_213 VERSION INFORMATION

Table B.1. Used *MAT_213 Version Information

Chapter	*MAT_213 version
1.1	V1.1
1.2	V1.0
1.3	V1.1
1.4	V1.1
1.5	N/A
2.1	N/A
2.2	N/A
3.1	V1.3.1
3.2	V1.3.1
3.3	V1.3.1
A.1	V1.2
A.2	V1.2
A.3	V1.2